MAX-PLANCK-INSTITUT
FÜR CHEMISCHE PHYSIK FESTER STOFFE

TECHNISCHE UNIVERSITÄT MÜNCHEN
Physik Department

The longitudinal magnetoresistance of Weyl semimetals

Marcel Naumann, M. Sc.

Vollständiger Abdruck der von der Fakultät für Physik der Technischen Universität München zur Erlangung des akademischen Grades eines

Doktors der Naturwissenschaften (Dr. rer. nat.)

genehmigten Dissertation.

Vorsitzender:	**Prof. Dr. Frank Pollmann**
Prüfer der Dissertation:	**1. Prof. Dr. Elena Hassinger** **2. Prof. Dr. Clemens Laubschat**

Die Dissertation wurde am 22.05.2019 an der Technischen Universität München eingereicht und durch die Fakultät für Physik am 24.06.2019 angenommen.

Abstract

Weyl semimetals offer the experimental realisation of an abstract theoretical model, Weyl fermions. What is more, they allow for the study of effects which were so far thought to be accessible only in large scale high energy physics experiments in a simple piece of metal.

The bulk of this thesis experimentally investigates the longitudinal magnetoresistance of Weyl semimetals, searching for indications of a chiral anomaly in the longitudinal magnetotransport, i.e. when field and current are aligned. This investigation is done on members of the TaAs family, which consists of TaAs, TaP, NbAs and NbP.

Searching for the chiral anomaly in Weyl semimetals, the large transverse magnetoresistance had previously been found to cause strong current inhomogeneities, concealing the intrinsic longitudinal magnetoresistance, ρ_{zz}. In this work, these artefacts are avoided by ensuring a homogeneous current injection. The experimental work is accompanied by simulations of the potential distribution in a sample with imperfect current contacts, aiding the interpretation of the experimental results. Also, the known band structure and Fermi energy is used to calculate the orbital longitudinal magnetoresistance to distinguish effects well explained by the 'trivial' band structure from those which are not. The c-axis transport is found to be fully dominated by orbital effects, while the a-axis longitudinal magnetoresistance in both niobium compounds and TaAs is not. Here, the non-monotonous magnetoresistance is attributed to weak localisation effects, which are larger than typically encountered in other materials. In conclusion, no clear indication of a chiral anomaly is found.

Two more projects are summarised. First, $\mathrm{CoSb_3}$ promised the opportunity for the investigation of a crossover from a trivial semiconductor into a topologically non-trivial material under strain. To find suitable samples, the influence of the growth method on the sample properties is investigated. While no suitable crystals for this experiment could be found, samples grown by a novel inclined rotary Bridgman method allowed for the study of a 3D isotropic electron gas in its quantum limit. The transport properties in fields up to 70 T are found to be consistent with an impurity scattering mediated mechanism, linking the transverse conductivity to the longitudinal one.

The second project on $\mathrm{UBe_{13}}$ is a contribution of measurements to solve a long standing question: This heavy-fermion superconductor mostly comes in a 'low'-T_{c} or a 'high'-T_{c} type. The two differ in their low-temperature properties, such as the superconducting critical temperature and specific heat. The difference could be traced to the incorporation of aluminium from the flux growth into the lattice, yielding the low-type variety. Annealing leads to aluminium diffusing out of the lattice, which changes the low-temperature properties to those of high-T_{c} samples.

Zusammenfassung

Weyl Halbmetalle machen ein abstraktes theoretisches Modell, Weyl Fermionen, zum ersten Mal experimentell zugänglich. Zudem erlauben sie, Effekte in einem Kristall zu Untersuchen, die man bisher lediglich in großen hochenergiephysikalischen Experimenten studieren konnte.

Der Großteil dieser Arbeit untersucht den longitudinalen Magnetotransport, d. h. unter paralleler Ausrichtung von Magnetfeld und Strom, von Weyl Halbmetallen der TaAs Familie (TaAs, TaP, NbAs, NbP) auf der Suche nach der chiralen Anomalie.

Bisherige Untersuchungen der chiralen Anomalie zeigten, dass Strominhomogenitäten den realen longitudinalen Magnetowiderstand, ρ_{zz}, verschleiern. Im Rahmen dieser Arbeit wurden diese Artefakte durch vollflächige, homogene Stromkontakte weitestgehend verhindert. Flankiert wurde dies durch Berechnungen auf Basis des bekannten transversen Magnetwiderstands sowie der elektronischen Struktur: Zum einen erleichterte die Simulation des elektrischen Potentials innerhalb eine Probe mit imperfekten Kontakten die Interpretation der Ergebnisse. Zum anderen wurde der orbitale longitudinale Magnetwiderstand berechnet, womit sich 'triviale' Beiträge von chiralen unterscheiden lassen. Der Magnetotransport entlang der c-Achse zeigt sich vollständig Orbital dominiert, im Gegensatz zum a-Achsen Transport. Dieser meist nicht-monotone Magnetwiderstand wird schwachen Lokalisierungseffekten zugeschrieben, welche sich ausgeprägter zeigen als in anderen Systemen. Zusammenfassend ließen sich keine eindeutigen Anzeichen für chirale Beiträge finden.

Es folgt ein kurzer Abriss über zwei weitere Projekte, $\mathrm{CoSb_3}$ und $\mathrm{UBe_{13}}$: In $\mathrm{CoSb_3}$ wurde ein Übergang vom trivialen Halbleiter zu einem topologisch nichttrivialen unter dem Einfluss einer Gitterverzerrung vorhergesagt. Auf der Suche nach geeigneten Proben wurde der Einfluss zweier Zuchtmethoden auf die elektronischen Eigenschaften untersucht. Hier stellten sich Kristalle die mittels eines neuartigen 'Inclined Rotary Bridgman' Verfahrens erzeugt wurden als Modellsystem für eine andere Fragestellung, die Untersuchung eines isotropen, dreidimensionalen Elektronengases in seinem Quantenlimit, heraus. Transportmessungen in hohen Magnetfeldern bis zu 70 T zeigten, dass sich die Eigenschaften durch ein Modell erklären lassen, in dem der transverse Transport stark vom Longitudinalen beeinflusst wird.

Das zweite Projekt befasst sich mit dem schwere Fermionen Supraleiter $\mathrm{UBe_{13}}$. Dieser zeigt sich in einer hoch und einer niedrig-T_{c} Variante, die sich in ihren elektronischen Eigenschaften bei tiefen Temperaturen unterscheiden. Dies wurde auf Einlagerungen des Aluminium Flusses zurückgeführt, welcher während der Einkristallzucht verwendet wird und die niedrig-T_{c} Ausprägung hervorruft. Durch thermisches Ausheilen diffundiert dieses aus dem Gitter und hinterlässt die hoch-T_{c} Variante.

Contents

1 Introduction

One of the most interesting aspects in condensed matter physics is to understand the interplay between the electronic structure and observable effects in an experiment. While the study of the electronic structure by methods such as quantum oscillations constitutes a field of its own right, gaining a detailed idea of the influence of the Fermi surface on e.g. magnetotransport properties takes the investigation a crucial step further. What is more, comparing this theoretical expectation with experimental results allows to find the border between what is understood so far and which effects still require more investigations.

One material class at the boundary of the current state of research are so called Weyl semimetals. Their low-energy physics can be modelled as solution to the 3D massless Dirac Hamiltonian, Weyl fermions, as first described 90 years ago by Hermann Weyl. The lack of inversion symmetry allows spin-orbit coupling to split bands into their spin-split variants. Bands crossing in individual points, so called Weyl points, now show an almost linear dispersion and a well defined chirality, i.e. a strict relation between momentum and spin as expected from Weyl fermions. The eigenstates at the bandcrossing have peculiar properties such as a non-trivial berry curvature which gives rise to a negative longitudinal magnetoresistance, the chiral anomaly. Weyl semimetals present the first three dimensional experimental realisation of such a system 90 years after their theoretical description.

Still, the electronic structure of a real condensed matter system often hosts more than Weyl nodes. Especially the TaAs family investigated in the course of this work also hosts 'trivial' Fermi surface pockets, not related to the topologically non-trivial ones enclosing the Weyl points ('Weyl pockets'). Additionally, more often than not the Fermi energy is too far away from the Weyl points to reasonably expect them to yield sizeable contributions to the transport properties. A detailed knowledge of the electronic structure is required to understand the possible influence of the Weyl-pockets on the electronic properties. This can only be gained by quantum oscillations and is the starting point of the investigation detailed here in the main text.

The attempt of the discovery of a new effect such as the chiral anomaly in transport calls for special experimental scrutiny. While presenting themselves with a cuvée of topologically trivial and non-trivial Fermi surface pockets, the TaAs compounds are compensated semimetals. As such, they come with a large transverse magnetoresistances which can cause strong current inhomogeneities when measuring in the longitudinal configuration required for the chiral anomaly. This demands high experimental care and non-standard contacting procedures to ensure a homogeneous current distribution. Simulations of the potential distribution within a sample with slightly imperfect current contacts still greatly aid the interpretation of the acquired data.

In the following, the theoretical background of the encountered effects is outlined in the first chapter. Here, calculations of the size of the orbital longitudinal magnetoresistance are presented. The next chapter details the experimental methods used for the study of the TaAs-type Weyl semimetals. Emphasis is put on the preparation of contacts and the simulation of the potential distribution within the samples when the resistivity is measured in the longitudinal configuration. The fourth chapter features the experimental results on the measurements of the longitudinal magnetoresistance in the TaAs family. Besides these, a general compilation of transport parameters such as mobilities and effective masses as determined by quantum oscillation measurements is included.

This is followed by a short discussion of two separate projects. Work on $CoSb_3$ included the investigation of the dependence of material properties on the growth method. Here, samples were found which appeared to be a suitable model system for the investigation of an isotropic electron gas confined to its lowest Landau level by a large magnetic field, the so called quantum limit. High magnetic field investigation well beyond the quantum limit field were carried out, finding a broad agreement with an existing theory which attempt to describe this state of matter. The second projects includes work on UBe_{13}, where in a collaboration with chemists a longstanding inconsistency in sample properties could be traced to aluminium impurities stemming from the single crystal growth.

2 | Theory

2.1. The (semi-)classical magnetoresistance

2.1.1. Zero-field resistivity

Since the bulk of the work presented in chapter 4.2 describes measurements on the intrinsic longitudinal magnetoresistance in Weyl semimetals, the background of the resistance in metals and the magnetoresistance in particular should be clarified first.

In a metal, the application of an electric field $\mathbf{E}$ will result in a current density $\mathbf{j}$. Both quantities are proportional to each other, with the conductivity $\hat{\sigma}$ being the proportionality constant [1]:

$$\mathbf{j} = \hat{\sigma}\mathbf{E} \tag{2.1.1}$$

Equation 2.1.1 is the microscopic version of Ohm's law. Since both $\mathbf{E}$ and $\mathbf{j}$ are vector quantities, they are denoted in bold. Consequently, the conductivity $\hat{\sigma}$ is a tensor and denoted as such with the hat.

A homogeneous electric field is now applied along the length l of a sample with cross section A. Integrating Eq. 2.1.1 over the volume of the sample recovers the potential drop over the length U and the total current I and yields

$$U = \hat{\sigma}^{-1}\frac{l}{A}I = \hat{\rho}\frac{l}{A}I = RI. \tag{2.1.2}$$

This is the macroscopic version of Ohm's law [1]. Here, $\hat{\rho} = \hat{\sigma}^{-1}$ is the so called resistivity, a material but not geometry dependent quantity. Combining $\hat{\rho}$ with sample size and cross section gives R, the resistance. This is typically determined in an experiment where currents and voltages and consequently, through Ohms' law, resistances and resistivities are measured.

On a more microscopic level, electrons with a charge e move through a lattice of positively charged ions similar to a gas. There is no long range interaction, only frequent collision with the lattice or with each other after a mean time τ. This model is also called the Drude model [1]. The scattering time τ and the effective mass of the electrons $m^* = m/m_0$ enters via the mobility μ [1]

$$\sigma_0 = ne\mu, \tag{2.1.3}$$

$$\mu = \frac{e\tau}{m^*}. \tag{2.1.4}$$

The subscript zero at σ_0 indicates the zero magnetic field value. A greater number of charge carriers and a longer scattering time will result in a higher conductivity.

2.1.2. Magnetoresistance

In zero field it is reasonable to express the conductivity tensor with respect to the crystal symmetry axes. Upon application of a magnetic field, it is convenient to switch to a basis which only takes the field direction into account. In the following discussion the magnetic field will be applied along the z axis. The notation is such, that the first subscript denotes the direction of the current and the second the direction along which the voltage is measured. Due to the symmetry in a typical cubic or tetragonal system where the field is applied along a main crystallographic axis, we assume only three independent components of the conductivity tensor, $\sigma_{\mathrm{xx}} = \sigma_{\mathrm{yy}}$[1], $\sigma_{\mathrm{xy}} = -\sigma_{\mathrm{yx}}$ and σ_{zz}. The matrix inversion of the conductivity tensor now yields the respective components of the resistivity tensor, such as

$$\rho_{\mathrm{xx}} = \frac{\sigma_{\mathrm{xx}}}{\sigma_{\mathrm{xx}}^2 + \sigma_{\mathrm{xy}}^2}, \tag{2.1.5}$$

$$\rho_{\mathrm{xy}} = -\frac{\sigma_{\mathrm{xy}}}{\sigma_{\mathrm{xx}}^2 + \sigma_{\mathrm{xy}}^2}, \tag{2.1.6}$$

$$\rho_{\mathrm{zz}} = 1/\sigma_{\mathrm{zz}}. \tag{2.1.7}$$

In general, the number of independent and non-zero components of the conductivity tensor depends on the symmetry of the system, which is the number of possible symmetry operations of the crystallographic point group minus those which are broken by the applied magnetic field under the respective direction. A more detailed account on this for the TaAs-family investigated here, is given in appendix A.1.

Misalignments of the magnetic field with respect to the main crystallographic axis will break the symmetries which preserve the reduced conductivity tensor described above. Consequences of the necessarily more complicated description are also detailed in appendix A.1, for the special case of the longitudinal component ρ_{zz}.

---

[1] This may not be true in a tetragonal system with field along a.

In an applied magnetic field, the material property $\hat{\rho}$ can change. The dependence $\hat{\rho}(\mathbf{B})$ is referred to as magnetoresistance (although magnetoresistivity might be more appropriate) and likewise $\hat{\sigma}(\mathbf{B})$ is the magnetoconductivity. Often it is useful to express the magnetoresistance in the normalised change of resistance in field, with ρ_0 being the zero field resistivity:

$$\Delta\rho/\rho_0 = \frac{\rho(B) - \rho_0}{\rho_0}. \tag{2.1.8}$$

In the σ_{xj} and ρ_{xj} components, where j =x,y, the current is applied perpendicular to the magnetic field. This case is typically referred to as the *transverse* case, the corresponding ρ_{xx} the transverse magnetoresistance and ρ_{xy} the Hall resisticity. In contrast, the zz component is with current parallel to the field direction, called the *longitudinal* case and ρ_{zz} the longitudinal magnetoresistance.

At sufficiently high fields, the Hall resistivity ρ_{xy} is closely related to the charge carrier density. For a one-band Drude model:

$$\rho_{\mathrm{xy}} = \frac{1}{ne}B. \tag{2.1.9}$$

Therefore, the slope of the Hall resistivity can be used the determine the charge carrier density of a material.

A good introduction to the microscopic effect of the application of a magnetic field on the resistivity is given in Pippards book [2]. Only the most important results will be quoted here.

In an electron gas, the Lorentz force $\mathbf{F} = e\mathbf{v} \times \mathbf{B}$ confines the electron movement perpendicular to the field on a circular trajectory in that plane, leaving the movement along the field unaffected. The angular frequency of the circular motion is the cyclotron frequency

$$\omega_c = \frac{eB}{m^*}. \tag{2.1.10}$$

The development of a spiralling trajectory along the field direction is stopped by scattering at e.g. defects after a scattering time τ. Therefore, the angle an electron is moved away from its original trajectory upon applying a magnetic field is $\gamma = \omega_c\tau$. If this angle is very small ($\gamma \ll 1$), so will be the influence of the magnetic field on transport properties. If the field is sufficiently strong to force electrons on fully developed spirals, winding multiple times ($\gamma \gg 1$), the influence might be rather big and impede the transport appreciably.

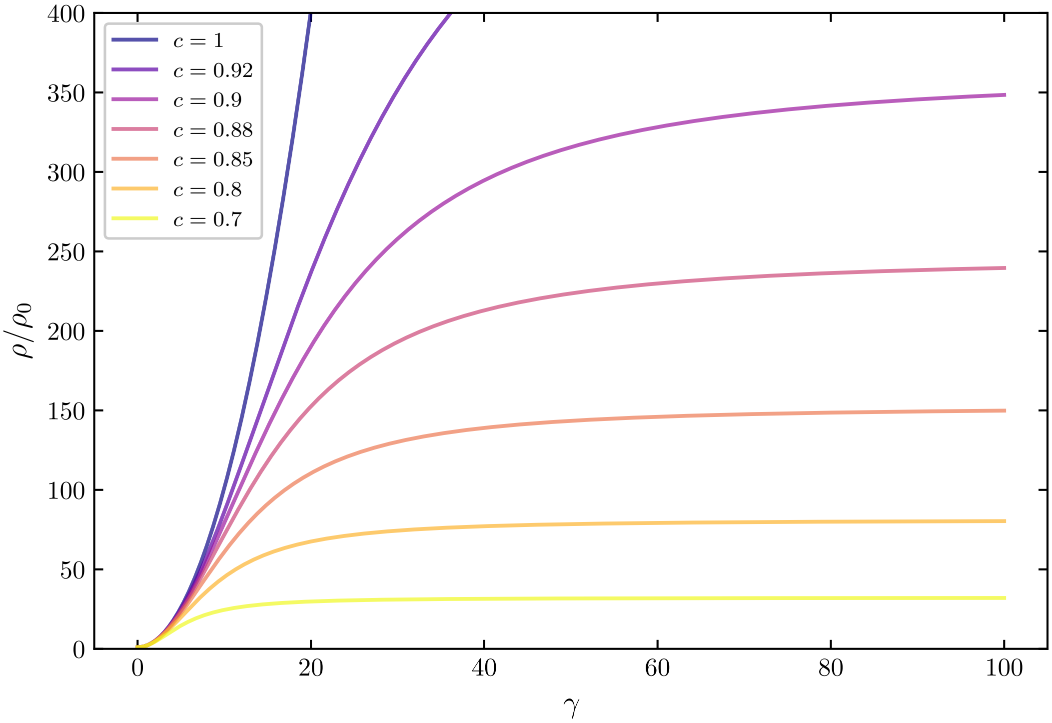

Figure 2.1.1. – Plot of Equation 2.1.13 for the compensated ($c = 1$) and nearly compensated case. Figure reproduced from [2, p. 30].

Sticking to the Drude model, the components of the conductivity tensor depend on the magnetic field [2]

$$\sigma_{\mathrm{xx}} = \sigma_{\mathrm{yy}} = \frac{\sigma_0}{1+\gamma^2} \tag{2.1.11}$$

$$\sigma_{\mathrm{xy}} = -\sigma_{\mathrm{yx}} = -\frac{\gamma\sigma_0}{1+\gamma^2}. \tag{2.1.12}$$

One can see the deflection angle γ to be the natural 'field scale' for the magnetoresistance. Still, upon applying the tensor inversion, one recovers $\rho_{\mathrm{xx}} = 1/\sigma_0$, a field independent transverse resistivity. This means, the free-electron gas exhibits no magnetoresistance. This is in agreement with what is observed in real materials: One of the best realisation of a free electron gas are alkali metals, such as potassium. Although not absent, the effect is very small: For $\gamma = 10$ the magnetoresistance $\Delta\rho/\rho$ is less than 10 % and at large values of $\gamma = 150$ it will only rise to about 20 % [2].

While the potassium only served as an illustration, in many other materials the prerequisites of a free electron gas are often not met: Many materials host more than one Fermi surface and more than one kind of charge carriers, electrons (contributions denoted with a - sign) and holes (+). Here, the conductivity is a sum of the two [2]:

$$\sigma_{\mathrm{xx}} = \frac{\sigma_-}{1+\gamma_-^2} + \frac{\sigma_+}{1+\gamma_+^2}$$

and likewise for the Hall component. Performing the matrix inversion, setting $\gamma = \gamma_- = \gamma_+$, $c = n_+/n_-$ as the degree of compensation and $\epsilon = 1 - c$ we arrive at [2]:

$$\rho_{\mathrm{xx}}/\rho_0 = \frac{1+\gamma^2}{1+\gamma^2\epsilon^2/(1+c^2)^2} \tag{2.1.13}$$

Apparently, if $c \neq 0$, there is a finite magnetoresistance. Indeed, the better the compensation, the higher the magnetoresistance, while for finite values of ϵ a saturation at high magnetic fields takes place. This is shown in figure 2.1.1.

To relate this to experiments, it is more convenient to use mobilities, instead of the cyclotron frequency and scattering time. Both are related by (see Eq. 2.1.4)

$$\gamma = \omega_{\mathrm{c}}\tau = \frac{eB}{m^*}\tau = \mu B. \tag{2.1.14}$$

Therefore, the transverse magnetoresistance should be proportional $\mu^2 B^2$, at least at lowest fields.

2.1.3. Magnetoresistance from Fermi-surface geometry

The discussion above is based on the Drude model, which implies an isotropic system. However, in real materials the breaking of the continuous translational symmetry in favour of a discrete one results Brillouin zones and Fermi-surfaces which are distinct from a perfect sphere. In the following, a microscopic model which includes such features is presented.

The quantitative treatment of this problem is typically done with a Boltzmann approach as developed by Shockley and Chambers in the 1950s [3, 4, 5]. An intuitive version of the expression of the conductivity tensor is [6]

$$\sigma_{ij} = \frac{e}{4\pi^3 B} \oint_{\mathrm{FS}} \mathrm{d}^2\mathbf{k} \oint_{\mathrm{cycl.orbit}} \mathrm{d}\mathbf{k}' u_{F_i}(\mathbf{k}) u_{F_j}(\mathbf{k}') \frac{P(\mathbf{k}',\mathbf{k})}{1-P(2\pi)}, \tag{2.1.15}$$

$$\frac{\mathrm{d}P(\mathbf{k}',\mathbf{k})}{\mathrm{d}\mathbf{k}'} = P(\mathbf{k},\mathbf{k}') \frac{\hbar}{eBl_{\mathrm{mfp}} \sin\angle(B,u_F(\mathbf{k}'))} \tag{2.1.16}$$

or

$$P(\mathbf{k},\mathbf{k}') = \exp\left(-\frac{\hbar K_{\mathrm{arc}}(\mathbf{k},\mathbf{k}')}{eBl_{\mathrm{mfp}} \sin\angle(B,u_F(\mathbf{k}'))}\right), \tag{2.1.17}$$

where

$u_{F_i}(\mathbf{k})$ is the normalised component of the Fermi velocity at $\mathbf{k}$,

$P(\mathbf{k}',\mathbf{k})$ is the probability that an electron makes it from $\mathbf{k}$ to $\mathbf{k}'$,

l_{mfp} is the mean free path,

$K_{\mathrm{arc}}(\mathbf{k},\mathbf{k}')$ is the length of a path on the Fermi surface from $\mathbf{k}$ to $\mathbf{k}'$.

First, the case of the transverse conductivity σ_{xx} on a spherical Fermi surface should be discussed. At low fields, the exponential disappears quickly and the expression reduces to an integral over $u^2_{F_x}(\mathbf{k})$ over the Fermi surface. Increasing the field, the ring integral comes into play and the correlator $u_{F_i}(\mathbf{k})u_{F_j}(\mathbf{k}')$ becomes more important. As soon as there is an appreciable probability that the electron manages half an orbit, the correlator changes sign[2], reducing the value of the ring integral and therefore the conductivity. In the extreme high field limit the exponential is a constant and the ring integral over the correlator approaches zero, at least in case of a somewhat circular shape of the cyclotron orbit. Therefore, the conductivity vanishes, which is qualitatively in agreement with Eq. 2.1.11.

Another case is the longitudinal conductivity σ_{zz}, first also on a spherical Fermi surface. If we, without loss of generality, assume to be at the 'top' of the sphere, u_{F_z} is positive, and independent of the position along the orbit $\mathbf{k}'$ (see figure 2.1.2, top). Therefore, the effect of the correlator described above, which changes sign and reduces the size of the integral, does not come into play. Here, the expected longitudinal magnetoresistance should be small, if at all existent.

---

[2] We assume only closed orbits here. For the xx component the differentiation between open and closed orbits is crucial, but beyond the scope of this work.

A different result is obtained if a tilted, ellipsoidal Fermi surface is assumed. Upon completing a cyclotron orbit, the sign of u_{F_z} changes (figure 2.1.2, bottom) and a similar situation to the one of the σ_{xx} component is recovered. In this case the magnetoresistance should be finite. We can see the geometry of the Fermi surface to play a crucial role for the size and existence of the magnetoresistance in general and particularly in the longitudinal case. This should be discussed in more detail in the following section.

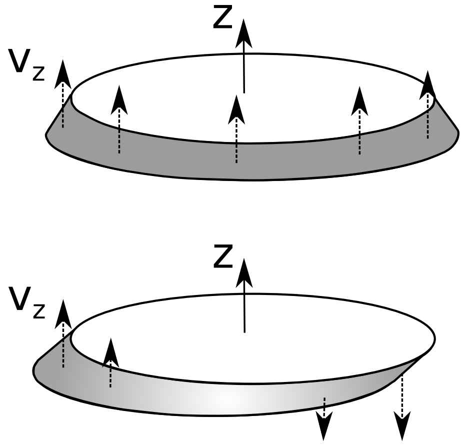

Figure 2.1.2. – Schematic illustration of the z component on a cyclotron orbit around two varieties of Fermi surfaces. Top: A spherical Fermi surface. Bottom: A tilted ellipsoid.

During the course of the thesis, it was unsuccessfully tried to calculate the conductivity tensor for a real material based on the band structure and Fermi energy alone using Eq. 2.1.15. Since the Fermi surface was extracted from the discrete 3D $E(\mathbf{k})$ matrix, small numerical errors from the discretisation and interpolation were present in the integrand. If the field was sufficiently strong, the value of the ring integral (if only taken along half a cyclotron orbit) was orders of magnitude larger than the integral around a full orbit, making the latter extremely susceptible to the noise present in the integrand. In the literature, equation 2.1.15 was evaluated successfully in quasi 2D materials where it was possible to rely on a cylindrical harmonic expansion of the Fermi surface [7]. This was not possible here. Nevertheless, this equation, is the basis of the work that is going to be discussed in the following section.

In order to distinguish the magnetoresistance, caused by the Fermi surface geometry as described above, from other sources which will be described later this will be referred to as *orbital* magnetoresistance.

2.2. The orbital longitudinal magnetoresistance (LMR)

The longitudinal magnetoresistance can have two origins: Anisotropic scattering [8] and a corrugation of the Fermi surface [9, 2]. Since there is no evidence of strongly anisotropic scattering in the Weyl semimetals, only the second should be discussed.

Recently, a publication by Pal and Maslov has outlined certain symmetry requirements on the band structure and therefore the Fermi surface which can lead to a non-zero longitudinal magnetoresistance [10]. The necessary and sufficient condition for the existence of a longitudinal magnetoresistance is:

$$\frac{\partial}{\partial k_\mathrm{z}}\left(\frac{\partial\epsilon/\partial\phi}{\partial\epsilon/\partial k_\rho}\right)\neq 0 \tag{2.2.1}$$

Here, the dispersion $\epsilon(\mathbf{k})$ is expressed in the cylindrical coordinates ϕ,k_ρ,k_z. Remembering $\mathbf{v}_\mathrm{F}=\partial\epsilon/\partial\mathbf{k}$ this can be interpreted geometrically: The angle between the angular and the radial Fermi velocity component has to vary upon moving along the z direction in the Brillouin zone in order to get a variation in ρ_zz with the magnetic field.

However, this does not mean, that any arbitrary anisotropic Fermi surface yields a finite longitudinal magnetoresistance. For example, both potentially highly anisotropic dispersions $\epsilon=\epsilon_\alpha(\phi,k_\rho)+\epsilon_\beta(k_\mathrm{z})$ and $\epsilon=\epsilon_\alpha(\phi,k_\rho)\cdot\epsilon_\beta(k_\mathrm{z})$ violate 2.2.1 and do not result in any finite longitudinal magnetoresistance.

2.3. Estimation of the size of the orbital LMR

Knowing the band structure and corresponding Fermi energy, we can now check for the existence of a longitudinal magnetoresistance with the theory presented by Pal *et al.* in [10]. More useful than the knowledge of existence or absence of a longitudinal magnetoresistance is the knowledge of its potential size. We will therefore not follow Eq. 2.2.1, but equations 20 and 22 in Ref. [10] instead:

$$\sigma_\mathrm{zz}(0)=\frac{2e^2\tau}{(2\pi)^3}\int \mathrm{d}^3k v_\mathrm{z}^2\left(-\frac{\mathrm{d}f^0}{\mathrm{d}\epsilon}\right), \tag{2.3.1}$$

$$\delta\sigma_\mathrm{zz}=\sigma_\mathrm{zz}(\infty)-\sigma_\mathrm{zz}(0)\sim\int\int\int \mathrm{d}\epsilon\mathrm{d}k_\mathrm{z}\mathrm{d}t_1\left(-\frac{\mathrm{d}f^0}{\mathrm{d}\epsilon}\right)(v_\mathrm{z}\langle v_\mathrm{z}\rangle-v_\mathrm{z}^2). \tag{2.3.2}$$

Here, τ denotes the isotropic scattering time, v_z the z component of the Fermi velocity (or, more general along the direction of current and field), f^0 is the Fermi-distribution function and $\langle v_\mathrm{z}\rangle$ is the average of the Fermi velocity along a cyclotron orbit. Regarding the integration in Eq. 2.3.2, ϵ denotes the energy, and t_1 is the time integration along a cyclotron orbit. Approaching the problem at zero temperature, $\mathrm{d}f^0/\mathrm{d}\epsilon$ is a delta function restricting the integration to a surface integration; therefore to the Fermi surface. Since only relative changes are of interest, the prefactor $\frac{2e^2\tau}{(2\pi)^3}$

shall be omitted, as the authors have already done in Eq. 2.3.2. The quantities S and δS which are defined to be proportional to $\sigma_{\mathrm{zz}}(0)$ and $\delta\sigma_{\mathrm{zz}}$ respectively can now be computed such as

$$\sigma_{\mathrm{zz}}(0) \sim S = \int_{\mathrm{FS}} \mathrm{d}^2k \; v_{\mathrm{z}}^2, \tag{2.3.3}$$

$$\delta\sigma_{\mathrm{zz}} \sim \delta S = \int_{\mathrm{FS}} \mathrm{d}^2k \; (v_{\mathrm{z}}\langle v_{\mathrm{z}}\rangle - v_{\mathrm{z}}^2), \tag{2.3.4}$$

where $\int_{\mathrm{FS}} \mathrm{d}k^2$ denotes the surface integration over the Fermi surface. This transformation from Eq. 2.3.2 to 2.3.4 is possible since the chosen integral measure $\int\int\int \mathrm{d}\epsilon \mathrm{d}k_{\mathrm{z}} \mathrm{d}t_1$ itself is a transformation from an integral measure, which covers the volume in k space [10, Eq. 15]. Consequently, $\delta S/S \sim \delta\sigma_{\mathrm{zz}}/\sigma_{\mathrm{zz}}$, which means the relative size of the expected longitudinal magnetoresistance can be estimated. Contributions of various Fermi surfaces are added, such that if $\Sigma = \sum_i \sigma_{\mathrm{zz}}^i$ (i denotes the index of the contribution of an individual Fermi surface), than $(\delta\sigma_{\mathrm{zz}}/\sigma_{\mathrm{zz}})_{\mathrm{total}} = \sum_i (\delta\sigma_{\mathrm{zz}}^i/\sigma_{\mathrm{zz}}^i) \cdot (\sigma_{\mathrm{zz}}^i/\Sigma)$.

2.4. The example of bismuth

To illustrate this and check on code used for calculations on the TaAs family, bismuth should serve as an example. The band structure and Fermi surfaces of this material are well known and analytical calculations of the expected longitudinal magnetoresistance exist [11]. What is more, bismuth is a compensated semimetal same as the TaAs family and as such an ideal test case.

Its band structure hosts an electron and a hole band with a slight overlap of few meV and both bands can be described using an anisotropic mass tensor. Detailed parameters will be omitted and can be found in [11]. The Fermi surfaces are of ellipsoidal shape and can be seen in figure 2.3.1. There is one hole Fermi surface with its long axis along the z direction (red), which is referred to as the trigonal direction. Besides this, there are three electron Fermi surfaces standing as an upside down tripod with threefold rotational symmetry 'underneath' the hole surface. They are ellipsoids as well, slightly tilted by $\sim 6°$ with respect to the plane

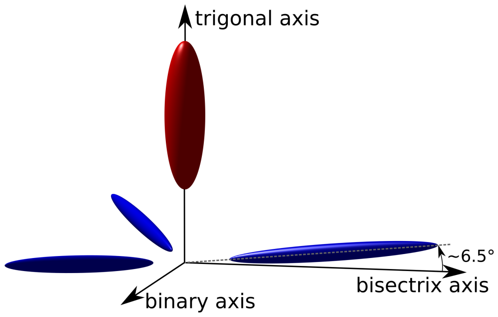

Figure 2.3.1. – Illustration of the Fermi surfaces of Bismuth and the crystallographic axes. Red: Hole surface. Blue: Electron surface.

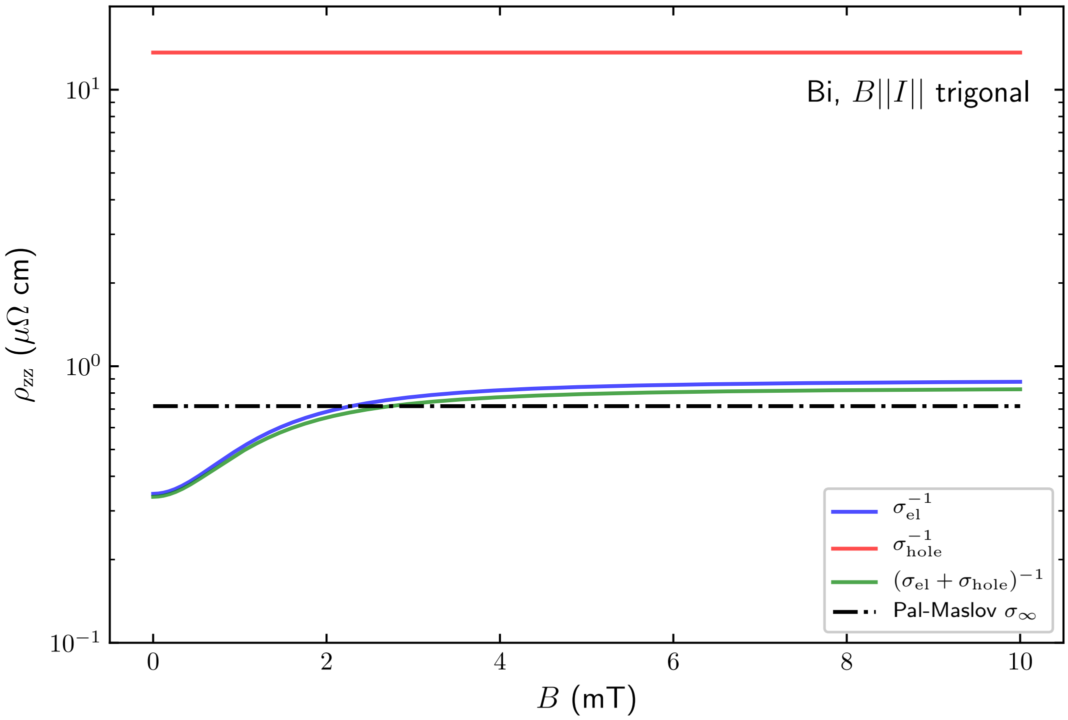

Figure 2.4.1. – The longitudinal magnetoresistance in bismuth, both according to the theory by Yoshida (coloured lines) and the expected saturation value according to the theory presented by Pal and Maslov. The individual contributions of the hole and electron band are also presented.

perpendicular to the z axis (figure 2.3.1, blue). This is typically referred to as the binary-bisectrix plane. The binary, bisectrix and trigonal axis constitute a orthogonal basis, with the trigonal as described pointing along the long axis of the hole surface, the bisectrix pointing along one of the electron surfaces and the binary is orthogonal to the other two. Therefore, the latter is pointing along no long axis of any Fermi surface.

Table 2.4.1 shows the results on the magnetoresistance in bismuth. Figure 2.4.1 shows Yoshida's results [11] and the saturation according to Pal and Maslov [10]. Also shown are the individual contributions of the electron and hole band to the transport along the trigonal axis. Both theories agree on the dominance of the electron surfaces. Also, both predict a field independent conductivity contribution of the hole band. This is despite explicit field dependencies in the equations presented in Yoshidas work, which actually cancel out.

The similarity of results is not surprising, since both theories approach the problem from a similar point of view. Based on a Boltzmann-theory approach discussed above

Table 2.4.1. – Calculated longitudinal magnetoresistance in Bismuth for $B||I||$ trigonal. Results from Yoshida [11] and Pal-Maslov [10] are shown as well. The factor of 3 appearing in the line of the electron Fermi surfaces is because of the threefold repetition of the electron surface in the Brillouin zone.

	$\Delta S = \int_{\mathrm{FS}} \mathrm{d}^2k(v_z - \langle v_z \rangle)^2$	$S_0 = \int_{\mathrm{FS}} \mathrm{d}^2k v_z^2 / \sum$	$\Delta S/S_0$
electron	$3.7 \cdot 10^{-77} \cdot 3$	$7 \cdot 10^{-77} \cdot 3$ / 99.3 %	0.53
hole	$2.7 \cdot 10^{-87}$	$1.4 \cdot 10^{-78}$ / 0.66 %	~ 0
Pal et al.			0.53
Yoshida			0.59

(see Eq. 2.1.15) the results are obtained by integrating the respective Fermi velocity components on the Fermi-surface. They differ somewhat in the treatment of the integral around the cyclotron orbit: In the theory by Pal and Maslov [10] they simplify this to an average Fermi velocity component while Yoshida [11] takes advantage of the simpler geometry of Bismuth which allowed the full analytical integration.

It can be concluded, that although there are small differences around 10 % in the relative change in conductivity in high fields, both yield very similar results. What is more, both agree in the qualitatively important prediction of the dominance of the electron Fermi surface to the transport along the trigonal axis. Therefore, the theory from Pal *et al.* to estimate the orbital longitudinal magnetoresistance can be considered valid.

2.5. Expected orbital LMR in TaAs-type Weyl semimetals

The ideas presented above can now be used to calculate the expected size of the longitudinal magnetoresistance in the Weyl semimetals investigated, based on their calculated and experimentally verified band structure.

The electronic structures of TaAs, TaP, NbP and NbAs were calculated using density functional theory (DFT) [12, 13, 14]. Calculations on NbAs, TaAs and TaP were done by Binghai Yan, Shu-Chun Wu and Yan Sun, with experimental input refining and confirming these by F. Arnold, E. Hassinger and the author. For NbP measurements and calculations were done by Klotz *et al.*, also with input from Binghai Yan's group [14].

The used functional for the exchange correlation energy and Fermi energy E_{F} for each material are shown in table 2.5.1. They were chosen such that the calculated angle dependent quantum oscillation frequencies (see section 2.8) agree with the ex-

Table 2.5.1. – Overview of the parameters used in the DFT calculations of the electronic structure of the Weyl semimetals.

	TaP[12]	TaAs[13]	NbP[14]	NbAs[15]
Functional	MBJ	MBJ	GGA	GGA
E_F	$8.26\,\mathrm{eV}$	$7.56\,\mathrm{eV}$	$10.858\,\mathrm{eV}$	$6.417\,\mathrm{eV}$

perimental ones. The equations presented in chapter 2.3 are now used to calculate the expected change in conductivity. The ratio S/Σ, proportional to the zero field contribution of the individual Fermi surface to the total transport, will prove helpful in the interpretation of the experimental results presented in section 4.2.2. Visualising the integrand of Eq. 2.3.4 on the Fermi surface helps to gain an understanding of what particular corrugation will contribute most to a change of longitudinal conductivity in field. This can be seen in figure 2.5.1 for both Fermi surfaces of TaP.

First, we should examine the case where field and current are along c as shown in figure 2.5.1 c) and f) and compare orbits α and β. The α orbit is around the waist of the Fermi surface, which is in parallel to the c direction. Consequently, the average Fermi velocity component along c is close to zero and so are the deviations from this average. As a result, this part of the Fermi surface does not contribute to the longitudinal magnetoresistance and shows up in blue.

The β orbit is qualitatively different. A large length of the orbit is along the sides (blue, on the right), with a very small $u_{\mathrm{F}c}$ which dominates the average of the orbit. Between the two 'horns' on the top, there is an area facing towards c, which consequently has a large Fermi velocity component along this direction, deviating strongly from the average and showing up in yellow.

In a similar way, the influence of geometries can be explained for field along a as presented in subfigure d). Along orbit γ the a component of the Fermi velocity is rather unified, with little deviation from the average. Therefore it shows up in blue. Along δ however, the side surfaces facing the b direction, with very small Fermi velocity component along a dominate the orbit. This causes the top bits, which face the a direction, to light up in yellow.

In order to calculate the expected orbital longitudinal magnetoresistance in the TaAs family, the replication of the Fermi surfaces by the crystal symmetry has to be taken into account (see chapter 4.1.2). Every Fermi surface, which is depicted in figure 4.1.3, is reproduced four times in the Brillouin zone, rotated by ±90° and 180° around the c axis. Figure 4.1.1 shows the full assembly of all replications of the Fermi

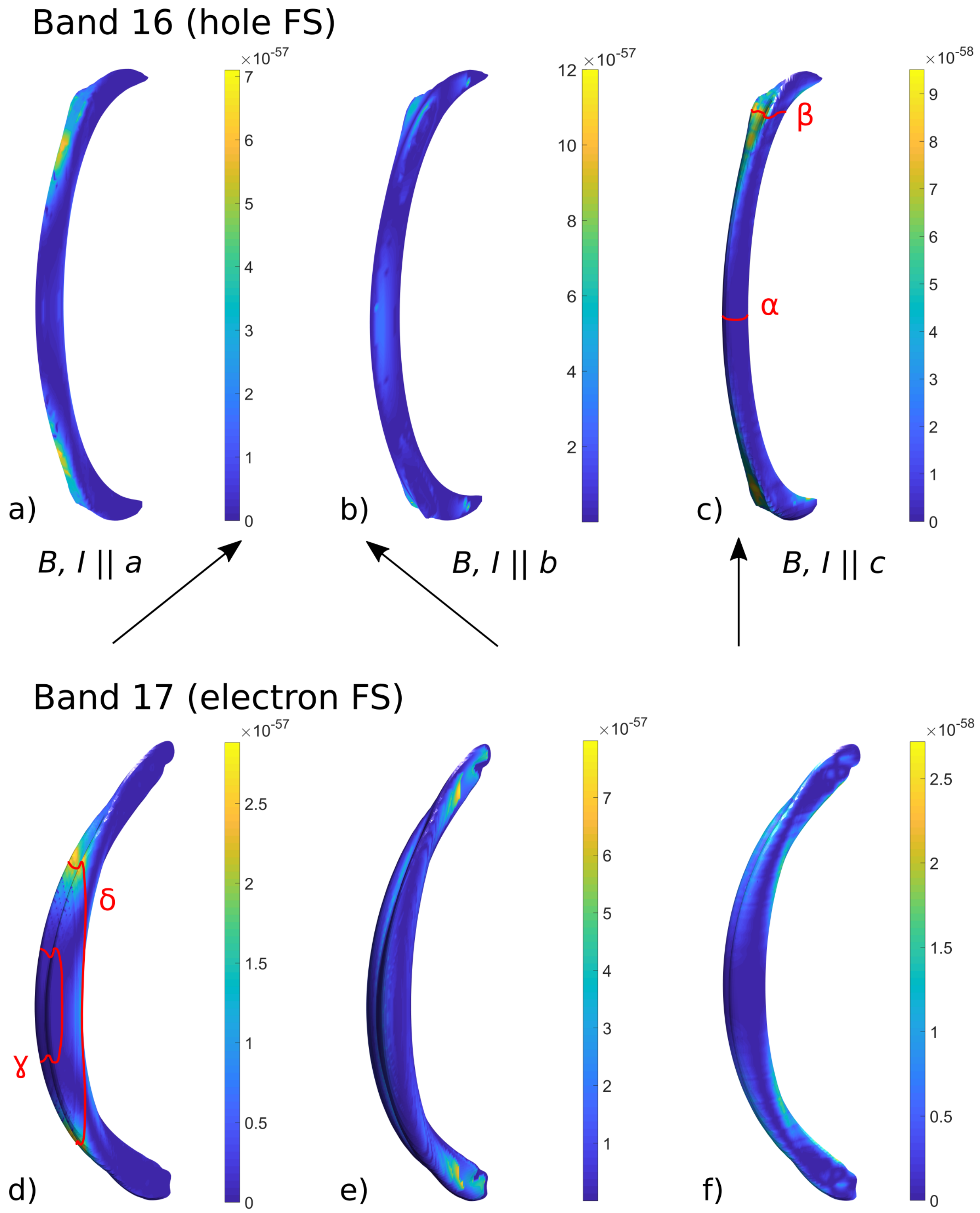

Figure 2.5.1. – Value of the integrand of Eq. 2.3.4 color coded on the Fermi surfaces of TaP for the three relevant orientations of magnetic field and current. The red cyclotrons orbits α to δ are only guides to the eye for the explanation.

surfaces in the Brillouin zone. The reproduction by 180° contributes the same way as the 'original', i.e. with current along a. Those surfaces rotated by 90° are different due to their symmetry and have to be treated separately. Therefore, calculation for current along a and b were performed, both constituting the in-plane ($I||a$) transport. For current along c, there is no influence of any rotation of the Fermi surfaces around the c axis, making all surfaces equivalent.

From all compounds an appreciable orbital longitudinal magnetoresistance along c of $\delta\sigma/\sigma = 0.62 - 0.96$ is expected. The experimental results, which will be presented in chapter 4.2.2, are shown for comparison. While there is some deviation between the calculation and experiment in TaP (0.96 theoretical vs. 0.77 experimental), both niobium compounds show a good agreement. In TaAs, there is a large uncertainty in the experimental results, as will be discussed in chapter 4.2.2.

Also, both tantalum compounds are expected to show some appreciable change in conductivity along a, while in both niobium compounds this is limited to below 10 %.

What is more, in NbAs there is one band dominating the transport in both orientations. In all other compounds, there are contributions from usually two bands. This will be of importance for the fit of the longitudinal magnetoresistance, especially along c, in these materials.

Table 2.5.2. – The orbital longitudinal magnetoresistance in all four materials. The results of the calculation, 'orbital $\delta\sigma/\sigma$' is compared to the experimental $\delta\sigma/\sigma$.

	$S_0 = \int_{\mathrm{FS}} \mathrm{d}^2 k v_z^2 / \sum$			$\Delta S/S_0$		
$I\vert\vert$	a	b	c	a	b	c
			TaP			
Band 16	0.11	0.38	0.72	0.53	0.13	0.93
Band 17	0.077	0.42	0.31	0.47	0.22	0.95
orbital $\delta\sigma/\sigma$				0.24		0.96
experimental $\delta\sigma/\sigma$				0.28		0.77
			NbAs			
Band 15	0.01	0.032	0.016	0.095	0.012	0.32
Band 16	0.002	0.76	0.95	0.4	0.02	0.8
Band 17	0.023	0.15	0.028	0.19	0.038	0.45
Band 18	0.00	0.00	0.00	0.07	0.32	0.13
orbital $\delta\sigma/\sigma$				0.075		0.77
experimental $\delta\sigma/\sigma$						0.7
			NbP			
Band 15	0.04	0.094	0.08	0.25	0.008	0.57
Band 16	0.092	0.26	0.40	0.44	0.017	0.82
Band 17	0.027	0.30	0.35	0.44	0.05	0.62
Band 18	0.013	0.18	0.17	0.54	0.04	0.83
orbital $\delta\sigma/\sigma$				0.097		0.73
experimental $\delta\sigma/\sigma$						0.7
			TaAs			
Band 16 (2x!)	0.004	0.21	0.39	0.9	0.35	0.72
Band 17	0.15	0.63	0.61	0.43	0.24	0.55
orbital $\delta\sigma/\sigma$				0.29		0.62
experimental $\delta\sigma/\sigma$				0.55 ± 0.15		~0.24[16]

2.6. Localisation and antilocalisation

Disorder is present in every experimental condensed matter system. In metallic samples, disorder results e.g. in the presence of a finite zero temperature resistivity. However, once the mean free path is of the order of or smaller than the phase coherence length of the quasiparticles, a more subtle effect can arise, the so called weak localisation.

Localisation and antilocalisation effects are also referred to as ’quantum interference effects’ [17] or ’quantum interference at defects’ [18, 19]. The term ’weak’ already hints this effect to be between two cases: On one side, the free electron gas, with the mean free path l_{mfp} being much longer than the electron wavelength λ. On the other side, if $\lambda \gg l_{\mathrm{mfp}}$, the system is fully localised. This is also referred to as Anderson localisation. However, despite its name, the weak localisation is a perturbative extension of the free electron gas [20].

The following introduction is similar to the one in Ref. [19]. If not stated otherwise, the next pages are based on this reference. The gedankenexperiment is to look at the probability for an electron to move from a point A to a point B (see figure 2.6.1). This might by accomplished by the passage of an infinite number of paths i, each with a quantum mechanical amplitude A_i, summing up to a total probability w such as

$$w = \left|\sum_i A_i\right|^2 = \sum_i |A_i|^2 + \sum_{i \neq j} A_i A_j^*. \quad (2.6.1)$$

While the sum over the first term at the end of equation 2.6.1 corresponds to the classical, Boltzmann type of transport, the second contains interference contributions. Those are the quantum corrections to transport which are at the heart of the effect described in this chapter.

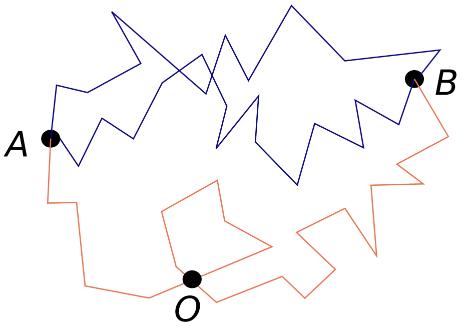

Figure 2.6.1. – Schematic illustration of the selfinterference process described in the text. There is a number of ways to get from A to B. Crucial here, is the differenciation between those which are not intersecting (blue) and those which intersect themselves (red).

Mostly, the interference between various paths is not of great importance: Their length and phase vary strongly, causing the interference term to be an oscillatory contribution, which cancels out. The exception are self-intersecting paths (see figure

2.6.1, red), which have sufficient coherence to produce an appreciable contribution to w.

The amplitude of the probability to find a particle at the point O in figure 2.6.1, is the sum the probabilities of a particle travelling around the loop clockwise, A_1, and counter-clockwise, A_2:

$$w = |A_1 + A_2|^2 = |A_1|^2 + |A_2|^2 + 2\Re A_1 A_2^* = 4|A_1|^2, \text{ since } A_1 = A_2. \tag{2.6.2}$$

The assumption was made that $A_1 = A_2$, since there is no reason why they should differ. Apparently, the probability to find a particle at O is twice the probability one would expect in a classical picture. Since particle number is conserved, an elevated probability to find a particle at O implies a decreased probability to find it anywhere else, e.g. at B. Therefore, the conductivity is decreased and the resistivity increased with respect to the classically expected value.

Still, self-interfering paths are not the only way from A to B. In order to estimate the size of the effect, one can look at the ratio $\delta\sigma/\sigma$, with $\delta\sigma$ being the quantum correction to conductivity. The volume of a path of an electron within a time t can be estimated as a tube, with a crosssection of λ^2 and a length of $v_\mathrm{F}t$, thus $\lambda^2 v_\mathrm{F} t$. Here, v_F denotes the Fermi velocity. At the same time, the classical transport can be described as a diffusive motion. The volume an electron can 'cover' is set by the diffusion constant D and is $(Dt)^{3/2}$. Since the amplitude change over a classical picture in Eq. 2.6.2 is of order unity, and prefactors of that size were omitted anyway, the change in conductivity will be of the order of the volume ratio of an electron path to total paths (the classical diffusive motion), therefore

$$\frac{\delta\sigma}{\sigma} \sim -\int_{\tau}^{\tau_\phi} \frac{\lambda^2 v_\mathrm{F}}{(Dt)^{3/2}} \mathrm{d}t. \tag{2.6.3}$$

The boundaries of the integration are set such, that it covers the time between an elastic scattering event τ and the time when all phase coherence is lost τ_ϕ. The minus sign is set, since the effect was already found to decrease the conductivity.

Although its where about is rather hand waiving, equation 2.6.3 illustrates the influence of various quantities on the process. To get an appreciable effect, a long Fermi wavelength and a high Fermi velocity is beneficial. A low diffusion constant will constrict the transport to a smaller volume (We stick to the picture sketched above) and hints that materials with a certain degree of disorder are the natural place to look for weak localisation physics[3].

---

[3] Indeed, most studies were done on quenched thin films [18].

The boundaries of the integration show a separation of time scales to be necessary for the effect in the first place: If the dephasing and the elastic scattering time are of the same magnitude, there will be no self-interference. It is only a separation of time scales between elastic scattering and dephasing, such as $\tau_\phi \gg \tau$ that allows for a detectable $\delta\sigma/\sigma$

Last but not least, there is a glimpse on the dependence on dimensionality d: The diffusion process in the denominator is to the power of 3/2 only in the 3D case. In 2D, a particle will cover an area of the order Dt during the same time. Apparently, the evaluation of the integral should yield a rational function in 3D while in 2D a logarithmic dependence on D, τ_ϕ, etc. is to be expected and can indeed be found in equation 2.6.5. This also sets the length scale for the crossover between various dimensions: It is when the sample size in a dimension perpendicular to the transport direction gets smaller than $L_\phi = (D\tau_\phi)^{1/2}$, that the crossover from d to $d-1$ happens.

What was not taken into account yet, is the effect of the electron spin and spin-dependent scattering [18]. The latter will introduce another phase shift of π to the completion of the loop, thus resulting in destructive instead of constructive interference at O and consequently an increase in conductivity. This is referred to as weak *anti*localisation.

Effect of an applied magnetic field

The phase coherence along the loop is maintained as long as the magnetic field is sufficiently small or turned off. While travelling the loop in a magnetic field, both the clockwise and counter-clockwise trajectory will acquire another phase of the same magnitude but with different sign, ultimately destroying phase coherence and the effect itself.

Since the qualitative background of the weak localisation has now been clarified, we can turn our attention to the quantitative results of the theory. These are a result of a field theoretical treatment of the quantum corrections to transport which are beyond the scope of this thesis.

In a d dimensional conductor, the field dependence of the correction to conductivity for a system with intact spin-rotational symmetry is given by [19, 20]

$$\sigma(B) - \sigma(0) = \delta\sigma = \frac{e^2}{2\pi^2\hbar}\frac{1}{l_{\mathrm{m}}^{d-2}} f_d\left(\frac{4De\tau_\phi B}{\hbar}\right). \tag{2.6.4}$$

The quantity $l_{\mathrm{m}} = \sqrt{\hbar/(eB)}$ is the so called magnetic length. In 2D and 3D, the function $f_d(x)$ is

$$f_2(x) = \ln(x) + \Psi\left(\frac{1}{2} + \frac{1}{x}\right), \tag{2.6.5}$$

$$f_3(x) = \sum_{n=0}^{\text{inf}} \left[2(n+1+1/x)^{1/2} - 2(n+1/x)^{1/2} - (n+1/2+1/x)^{-1/2}\right]. \tag{2.6.6}$$

Ψ denotes the Digamma function. As mentioned above, the logarithmic dependence in the 2D case is clearly observable [21, 22].

However, there are scattering processes, which influence the spin of an electron. When the scattering probability depends on the spin orientation of the incident and scattered particle, the process is called 'spin-orbit' scattering, with a scattering time τ_{so} [18]. In 3D this enters the correction to the conductivity of the antilocalisation such as

$$\sigma(B) - \sigma(0) = \delta\sigma = \frac{e^2}{2\pi^2\hbar}\sqrt{\frac{eB}{\hbar}}\left[\frac{3}{2}f_3\left(\frac{B}{B_2}\right) - \frac{1}{2}f_3\left(\frac{B}{B_\phi}\right)\right]. \tag{2.6.7}$$

Here, for the sake of convenience some factors were rewritten: $B_i = \hbar/4eD\tau_i$ where $i = \phi$,so and $B_2 = B_\phi + 4/3B_{\mathrm{so}}$. When this equation is used to model experimental data in chapter 4.2.2, it will appear in the models as $\sigma_{\mathrm{3DWAL}}(B_\phi, B_{\mathrm{so}})$. The physical meaning of the introduced 'magnetic fields' B_i will become more clear, by rewriting them using the flux-quantum, $\Phi_0 = h/2e$, which yields $B_x = \Phi_0/4\pi D\tau_x$. The diffusion constant D has units of area over time, therefore $D\tau_x = \tilde{A}$ refers to the area a diffusing electron state can cover in its 'lifetime', or sticking to the picture above, the area the loop encloses. Multiplying with this area, on gets $\tilde{A} \cdot B_x = \Phi_0/4\pi$. Therefore, the field B_x is the field, at which the loop-shaped electron orbit encloses a flux of a flux-quantum, at least down to a prefactor 4π.

Comparing equations 2.6.4 and 2.6.7 one can see the former to be the special case of the latter if $B_{\mathrm{so}} = 0$. In fact, the $3/2f_3(B/B_2)$ term describes the propagation of triplets, while the $-1/2f_2(B/B_\phi)$ is associated with the propagation of electron singlets [23]. Note the prefactors 3/2 and 1/2, since there are three times more possible states in the triplet channel. This also shows spin-orbit scattering to influence only the triplet propagation (via B_2). Also, if τ_{so} is sufficiently strong, both f_3 terms will vary on different field scales, giving rise to a sign inversion of the effect as can be seen in figure 2.6.2.

Actually, the question of a localisation or antilocalisation is purely down to the universality class and does not relate to the increasing or decreasing resistivity [24]. A system with intact time-reversal symmetry can be distinguished into two different

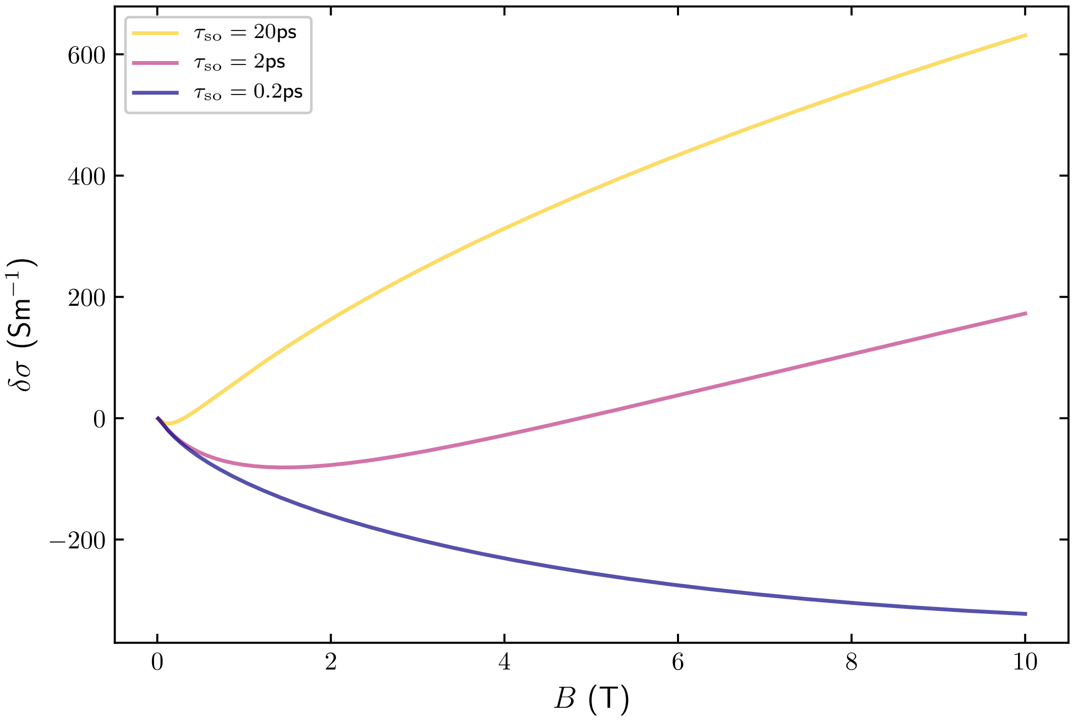

Figure 2.6.2. – The correction to the conductivity from a 3D antilocalisation according to Eq. 2.6.7 for various τ_{so}. The assumed dephasing time τ_ϕ is 0.1 ns.

classes: The 'orthogonal' class, when spin-rotational symmetry is conserved will result in a localisation while the 'symplectic' class when it is broken will result in an anti-localisation. The latter is the case e.g. in systems with strong spin-orbit coupling and spin polarised Fermi surfaces. As will be pointed out in section 4.1, this should be the case for Weyl semimetals. However, as will be described below, this is only true in the simplest model, therefore in the absence of inter-valley (or inter-node) scattering.

2.6.1. Localisation physics in Weyl systems

The derivations presented above are based on a free-electron model, where the kinetic energy E_{kin} depends on the momentum k such as $E_{\mathrm{kin}} = \hbar^2 k^2/2m^*$, with m^* being the effective mass. In contrast, Weyl systems have a linear relationship between E_{kin} and k, such as $E = \pm\hbar v_{\mathrm{F}}\sigma\mathbf{k}$, with σ being the vector of Pauli matrices (see chapter 4.1). This obviously favours an (anti)parallel spin orientation with respect to the momentum $\mathbf{k}$. A first treatment of localisation physics in Weyl systems was done by Lu and Shen [17].

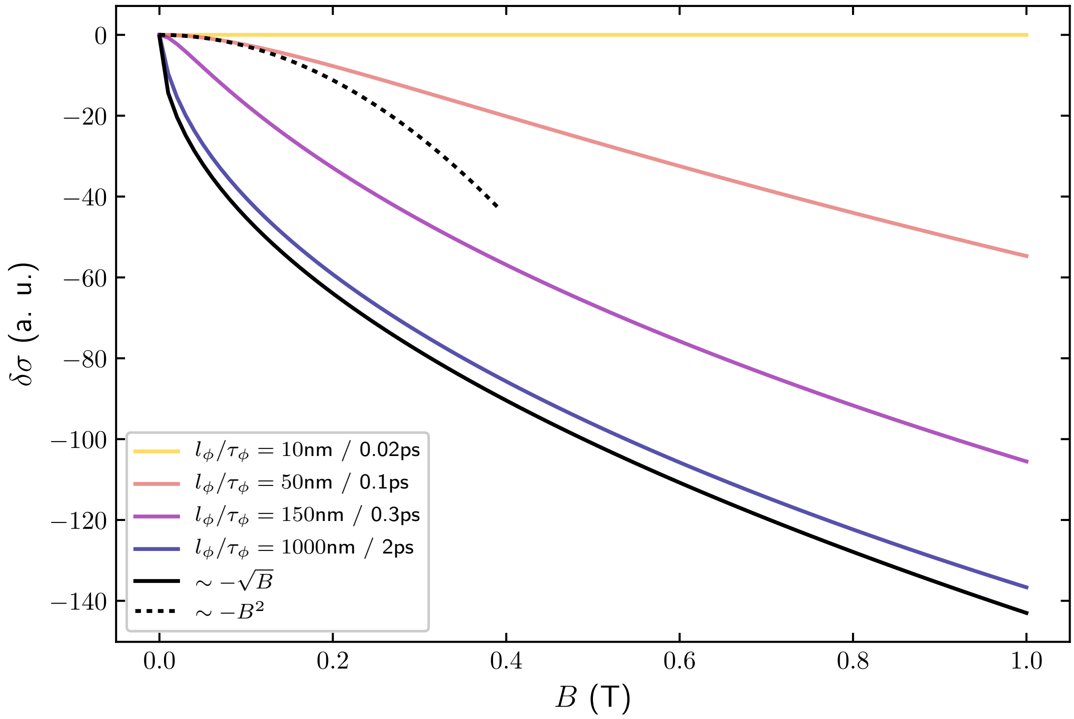

Figure 2.6.3. – Illustration of the field dependence of the quantum interference correction to conductivity for Weyl fermions. Both limits of a $-B^2$ dependence at low fields and low coherence lengths and a $-\sqrt{B}$ dependence at large coherence lengths are illustrated. A mean free path l of 10 nm was assumed, which corresponds to a total scattering time of 0.02 ps. For all calculations of the scattering time from the used mean free paths a Fermi velocity of $5 \cdot 10^5\,\mathrm{m\,s^{-1}}$, corresponding to the one found in TaAs [13] or NbP [25], was assumed.

The spin-momentum relation in the Hamiltonian breaks spin rotational symmetry, thus putting the system into the symplectic universality class which should result in an antilocalisation. The field dependence of the magnetoconductivity $\delta\sigma(B) = \sigma^{\mathrm{qi}}(B) - \sigma(0)$ is given by

$$\sigma^{\mathrm{qi}}(B) = \frac{2e^2}{h} \int_0^{1/l} \frac{\mathrm{d}x}{(2\pi)^2} \left[\Psi\left(\frac{l_{\mathrm{B}}^2}{l^2} + l_{\mathrm{B}}^2 x^2 + \frac{1}{2} \right) - \Psi\left(\frac{l_{\mathrm{B}}^2}{l_\phi^2} + l_{\mathrm{B}}^2 x^2 + \frac{1}{2} \right) \right]. \tag{2.6.8}$$

Here, $l_\mathrm{B} = \sqrt{\hbar/4eB}$ denotes again the magnetic length[4], l the mean free path and l_ϕ the phase coherence length. As above, Ψ is the digamma function. Figure 2.6.3 shows equation 2.6.8 with an assumed scattering length of 10 nm.

At low coherence lengths, equal to the mean free path there is no correction to conductivity, since the prerequisite of the effect $\tau \gg \tau_\phi$ is not full filled. Upon increasing the coherence length, at low fields a $-B^2$ dependence emerges evolving into a $-\sqrt{B}$ dependence at high coherence lengths.

As will be presented in section 4.1, Weyl nodes do come in a pair, and equation 2.6.8 is derived for only a single Weyl node, or 'valley'. This is of no concern, as long as both are decoupled, therefore in the absence of intervalley scattering. Under certain conditions, including strong inter-valley scattering, an effective orthogonal symmetry can be reinstated, which will consequently give rise to a localisation rather than an antilocalisation [17].

This crossover is not a speciality of Weyl systems and has already been studied theoretically for carbon nanotubes [26].

2.7. Chiral anomaly

A more detailed introduction into Weyl systems can be found in chapter 4.1. In these systems, points exist in which there is a band crossing with a dispersion distinct from the typical quadratic one. It is linear, with a fixed relation between spin and momentum ('chirality') and therefore the same as for massless Dirac fermions. These points, the Weyl points, do come in pairs of opposite chirality, which means that in one, spin and momentum are parallel and in one they are antiparallel.

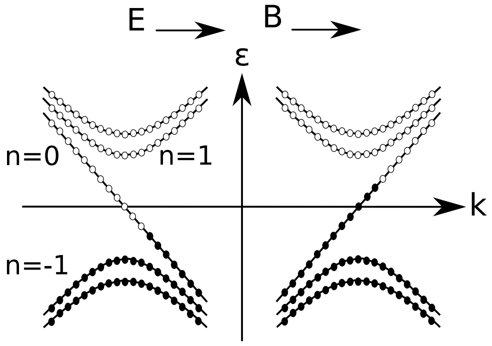

Figure 2.7.1. – Schematic illustration of the charge pumping effect due to the 'Adler-Jackiw-Bell' or 'chiral' anomaly

What is also different to a normal metal, is the Landau-level structure (see chapter 2.8) in high magnetic fields. In a normal metal, all Landau-levels have a quadratic dispersion along the field direction and their energy is affected by the applied magnetic field. In contrast, in a Weyl system the $n = 0$ (therefore the lowest) Landau level is still linear at the Weyl point. It gives rise to

---

[4] The authors use another definition than the one used before. Note the additional factor 4 in the denominator.

one left moving branch at one point and the corresponding right moving branch at the other (see figure 2.7.1). This dispersion is the foundation of the chiral anomaly.

To describe this effect in 3D, it is illustrative to start thinking about transport in the closely related 1D case first. In a one dimensional system of Weyl points, an applied electric field will result in an acceleration of particles according to $\dot{k} = eE/\hbar$. Once the acquired momentum exceeds the distance of the Weyl points, a particle can hop from its branch to the Weyl node towards which it was accelerated to, thus generating an imbalance in the charge carrier number $n_{\mathrm{R/L}}$ between the right and left node. The rate at which the particle imbalance is acquired is proportional to the applied electric field [27]

$$\frac{\mathrm{d}n^{\mathrm{1D}}_{\mathrm{R/L}}}{\mathrm{d}t} = \pm\frac{e}{h}E. \tag{2.7.1}$$

Here, $n_{\mathrm{R/L}}$ denotes the number of particles on the right (+) and left (−) moving branch. The 1D denotes the 1D case. Essentially, this describes transport in a 1D Weyl system.

The situation in a 3D Weyl system in an applied magnetic field is similar. As described, the dispersion perpendicular to the field direction will by quantised into Landau levels (see chapter 2.8) while the energy levels will still be dispersing along the field direction. In a Weyl system, there will be a left and a right moving branch of the zeroth Landau-level as a remainder of the zero field dispersion (see figure 2.7.1). This situation somewhat resembles the one-dimensional case described above. The 3D number density of a conduction channel is related to its 1D counterpart by its crosssection $\mathcal{A}$, which only contains one flux quantum Φ_0 such as $n^{\mathrm{3D}}_{\mathrm{R/L}} = (1/\mathcal{A})n^{\mathrm{1D}}_{\mathrm{R/L}}$ with $\mathcal{A} = \Phi_0/B$ [27]. This can be put into Eq. 2.7.1, where the change in dimensionality changes some prefactors as well [27]

$$\frac{\mathrm{d}n^{\mathrm{3D}}_{\mathrm{R/L}}}{\mathrm{d}t} = \pm\frac{e^2}{h^2}\mathbf{E}\cdot\mathbf{B}.. \tag{2.7.2}$$

Since an imbalance in right and left moving charge carriers as depicted in figure 2.7.1 is equivalent to a current, the conductivity is affected such as

$$\Delta\sigma(B) = \frac{e^2}{4\pi^2\hbar c}\frac{v_{\mathrm{F}}}{c}\frac{(eB)^2 v_{\mathrm{F}}^2}{\mu^2}\tau_\nu. \tag{2.7.3}$$

Here, v_{F} is the Fermi velocity, μ is the chemical potential in zero field relative to the energy of the Weyl points and τ_ν denotes the inter-valley or inter-node scattering time. The last result was found by Son and Spivak by a Boltzmann approach [28],

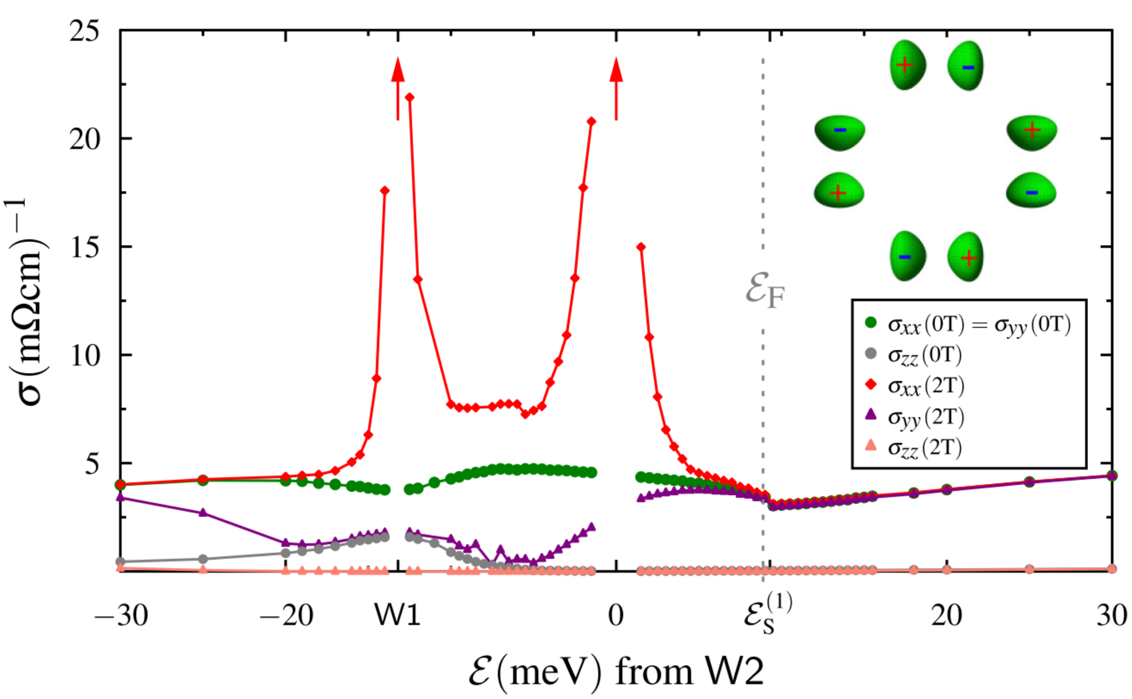

Figure 2.7.2. – Supposed energy dependence of various conductivity contributions in a model system resembling TaAs. The indices refer to the crystallographic axis (x, y is the a axis, z is the crystallographic c direction), the magnetic field is applied along x. Red, σ_xx: longitudinal conductivity contribution of the chiral anomaly in field. Green: zero field conductivity along the same direction. The transverse in-plane conductivity σ_yy (therefore, along a but perpendicular to the magnetic field) is the stronger suppressed the close the Fermi energy is to the Weyl points. Figure from [32].

under the assumption of a finite chemical potential as measured relative to the Weyl point. It essentially reproduces the field-theoretical calculation done by Nielsen and Ninomiya [29] which are based on the Adler-Jackiw-Bell anomaly from high energy physics [30, 31].

This correction to the conductivity is positive in field, therefore the conductivity rises as B^2 and likewise, the resistivity decreases as B^{-2}.

2.7.1. Energy dependence

The Fermi energy and angle dependence of the transport properties of a Weyl system is investigated in a publication by Johansson *et al.* [32]. The authors also choose a Boltzmann transport theory approach, similar to Son and Spivak [28], but including a Hamiltonian that is closer to the real system. It includes two Weyl (in its simplest version) nodes and bands connecting these at higher and lower energy. Therefore, a shift in Fermi energy μ can merge both Weyl pockets similar to what happens in a real system. Also, this approach comes with anisotropic Fermi surface pockets, which crucially influences the magnetoresistance properties as already outlined in chapter 2.1. From this starting point, taking the non-trivial Berry curvature and delta-shaped impurities into account, a full Boltzmann transport calculation is performed. This is done for a system of two Weyl points (i.e. a system with broken time-reversal symmetry), four (one with broken inversion symmetry) and 24 (TaAs as a model system, taking the Fermi energy and Fermi velocity found in [13] into account).

The result regarding the energy dependence is a μ^{-4} scaling, found for a two or four Weyl point system and a rough μ^{-3} scaling for the TaAs-like system. This is in contrast to the μ^{-2} scaling in equation 2.7.3 and the experimental results presented in [33], although the later are questionable and will be discussed in chapter 4.1.

The Boltzmann approach is independent on a well defined chirality, but only 'senses' the locally non-trivial Berry curvature. This still persists once both Weyl pockets have merged at μ greater the saddle-point energy, which is why there is still a finite, albeit vanishingly small contribution of the chiral anomaly at these high Fermi energies. Still, since the magnitude of the chiral anomaly is falling of with at least some power of μ, it is already suppressed to a experimentally irrelevant size *before* both pockets merge, i.e. when chirality is actually still defined [34, 32].

2.7.2. Angular dependence

The connecting direction of the Weyl points breaks the threefold rotational symmetry of the system. Therefore, a dependence of the size of the effect on the orientation between current and the connecting direction of the Weyl points, α, is not unexpected and has indeed been found [35, 32]. Both references differ in their approach and findings.

Behrends *et al.* [35] derive an expression of the angle dependence of the ratio of the inter-node and intra-node scattering time. Since the inter-node scattering time linearly scales the $\delta\sigma \sim B^2$ contribution, this is a measure of the angle dependence of the chiral anomaly. Their approach starts with the Hamiltonian of a Weyl system and includes impurity scattering, modeling the impurity potential with an extended, Gaussian shaped impurity potential. To get a qualitative idea of their argument, it is useful to look at the Landau-level structure of the Weyl nodes, as illustrated in figure 2.7.1. The x-axis is along the field direction and as such qualitatively independent on α. On the other hand, the Weyl node separation in figure 2.7.1 is the projection of node separation in zero field onto the field axis and consequently depends on $\cos\alpha$[5]. In other words, the further away the field is oriented from the node-separation axis, the closer the Weyl nodes get, which should increase inter-node scattering. The ratio between inter-node (τ_ν) and intra-node scattering (τ) can be calculated such as

$$\frac{\tau_\nu}{\tau} = \exp\left[\frac{1}{2}\xi^2 b^2 \left(\cos^2\alpha + \frac{l_\mathrm{B}^2}{l_\mathrm{B}^2+\xi^2}\sin^2\alpha\right)\right]. \tag{2.7.4}$$

As usual, $l_\mathrm{B} = \sqrt{\hbar/eB}$ denotes the magnetic length, further b is the Weyl-node separation and ξ is the impurity potential correlation length. Since the intra-node scattering time is angle independent, the angular dependence is from the inter-node scattering time only. This enters into the correction to the conductivity $\delta\sigma$ linearly (Eq. 2.7.3), making the ratio of the two scattering times a measure of the angle dependence of $\delta\sigma$.

With equation 2.7.4 at hand, a lower boundary for the anisotropy of the chiral anomaly in the TaAs family can be estimated. The Weyl-node separation b is known to depend on the size of spin-orbit coupling and is therefore larger in Ta than in Nb systems, with a range of $3\cdot10^8$-$1\cdot10^9\,\mathrm{m}^{-1}$ [36]. The impurity potential correlation length will be estimated with the Debye length $l_\mathrm{D} = \sqrt{(\epsilon/e_0^2 D(E_\mathrm{F}))}$, with $D(E_\mathrm{F})$ the density of states at the Fermi energy. A detailed account of the used parameters for this is given in appendix A.4, where a range of $l_\mathrm{D} = 10-100\,\mathrm{nm}$ is retrieved. Since the anisotropy is proportional $\exp(\xi^2 b^2)$, the lower values of both will serve for an estimate of a lower boundary of the anisotropy, shown in figure 2.7.3. This shows a change of nearly a factor two, while higher estimates for both ξ and b will result in variations over a few orders of magnitude.

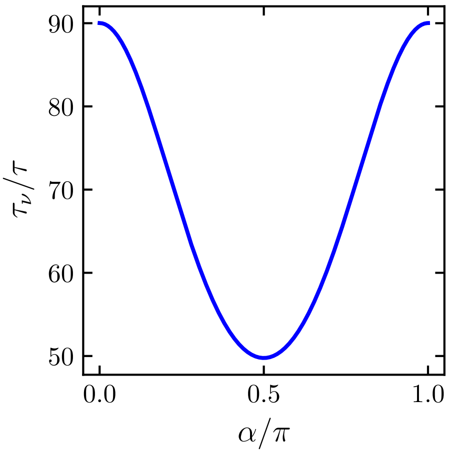

Figure 2.7.3. – Lower boundary for the angle dependence of the ratio of the internode to intranode scattering time.

It should also be noted, that this is independent on the amount or kind of scatterers. This would only scale the absolute size of the scattering times, while the angle

---

[5] We will omit the field dependence of the Weyl-node separation in this zeroth order illustration of the mechanism.

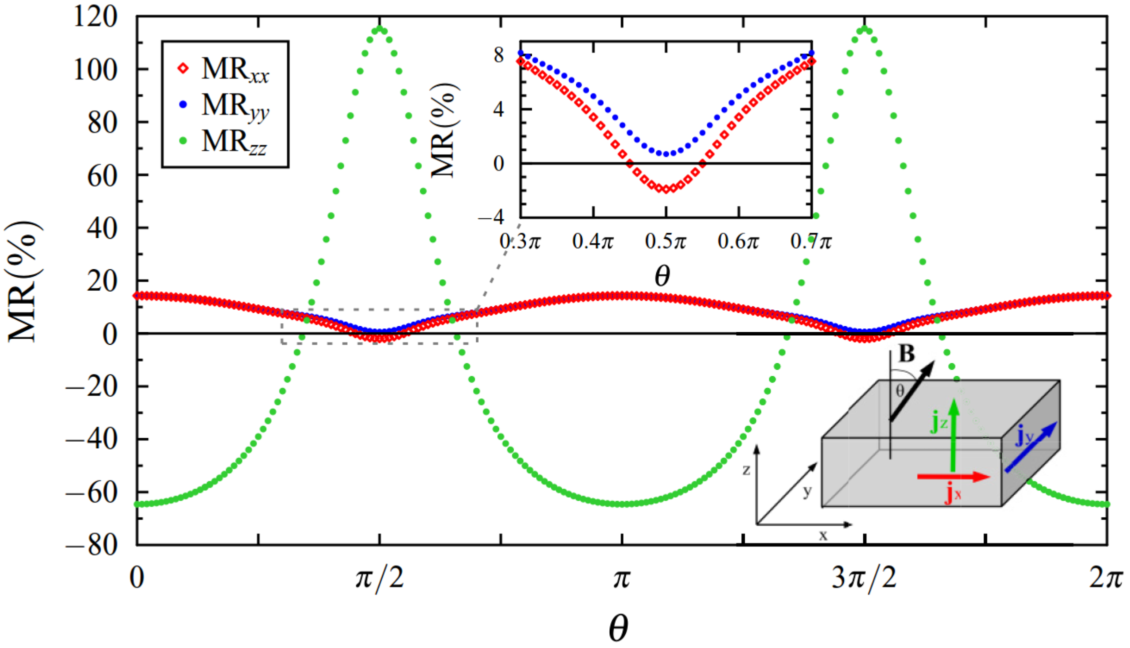

Figure 2.7.4. – Angle dependence of the magnetoresistance in a TaAs model system. The indices xx, yy and zz refer to the orientation with respect to the crystallographic axes a, $b = a$ and c respectively. The field is rotated from the $c = z$ axis to the $x = a$ axis, i.e. $\mathrm{MR}_{\mathrm{yy}}$ is always the transverse magnetoresistance. Figure taken from [32].

dependent ratio is a result of the projection of the Weyl-node distance onto the field direction.

In Johansson *et al.*, the authors chose a more realistic Boltzmann approach but treat impurities as delta-shaped potentials [32]. The angle dependence can be seen in figure 2.7.4 and is in contrast to the results of Behrends *et al.*. A strong increase in the chiral anomaly contribution to the conductivity is found, if field and current are along c, therefore, *perpendicular* to the axis connecting the Weyl nodes. This is supposed to be caused by the anisotropy of the Fermi surface, which is elongated along c, giving rise to a higher resistivity in this direction which is 'amplifying' the effect.

Also, upon tilting the field 1° away from the a axis, the intermixing of the transverse magnetoresistance will cause an initial increase before the chiral anomaly contribution is taking over, dominating the high field longitudinal magnetoresistance which is again negative. Since misalignments of 1° are absolutely reasonable in any experiment which only has a single axis rotation stage, this could very well explain the low field increase in resistivity seen in a number of studies [37, 38, 33, 39].

The difference in findings of Behrends *et al.* and Johansson *et al.* is probably caused by the different models both are using. While in Behrends study the results depend crucially on the scaling of the impurity potential size ξ with respect to the Weyl node separation b, Johansson *et al.* only takes delta-shaped impurity potentials into account. This might be one of the reasons of the deviations. The other possible reason is, that Johansson uses the full Boltzmann transport theory including Fermi surface anisotropies etc. which goes far beyond Behrends approach.

It should also be noted, that despite presenting the most comprehensive study of transport in a Weyl system known to the author, there are naturally still some differences between the model used in Johanssons work and TaAs. Since the magnetoresistance depends strongly on the Fermi surface geometry, the real shape of the Fermi surfaces of TaAs and the presence of the trivial hole pocket (see figure 4.1.3) will certainly alter the transport properties. Also, the lower charge carrier density compared to normal metals results in an enlarged impurity potential size, rather distinct from the delta-shaped potentials assumed in Johanssons work. The localisation of these facilitates scattering over large k, while in a real system this would be suppressed.

2.8. Quantum Oscillations

The following section is largely based on the thesis of J.-F. Mercure [40], from which some of the notation has been adopted as well as C. Bergemanns thesis [41]. An alround and indepth reference is the book by Shoenberg [42].

Historically, the effect was first discovered in pure Bismuth after its prediction by Landau only a few month earlier [43]. Studying its resistivity at low temperatures in an applied magnetic field, Wander Johannes de-Haas and Lev Shubnikov observed oscillations in the resistivity, which were later referred to as Shubnikov-de Haas (SdH) oscillations [44]. At the same time, de Haas also studied the field dependence of the magnetisation of Bismuth together with Pieter M. van Alphen. Likewise, quantum oscillations observed in magnetisation or magnetic torque are referred to as de Haas-van Alphen (dHvA) oscillations [45].

2.8.1. Theoretical background

In section 2.1 it was discussed how an applied magnetic field can change the conductivity of a free electron gas. But more consequences can arise if the field is sufficiently strong. If the magnetic field is applied along z to an electron gas which is constrained to a box-shaped volume, it will cause the emergence of quantised circular orbits in the $k_\mathrm{x} - k_\mathrm{y}$ plane. Meanwhile, the dispersion along z will remain untouched, leaving k_z as a good quantum number. The spectrum of the free electron gas will therefore be altered by the presence of the magnetic field to

$$E_n = \left(n + \frac{1}{2}\right)\hbar\omega_\mathrm{c} + \frac{\hbar^2 k_\mathrm{z}^2}{2m^*}. \tag{2.8.1}$$

The second term in equation 2.8.1 describes the dispersion along the field direction which remains unaffected, while the first term describes the so called Landau levels with level index n and the cyclotron frequency $\omega_\mathrm{c} = eB/m^*$. The reason for the quantisation is in the wave character of the electrons: Since the magnetic field forces charged particles to move on cyclotron orbits, they will eventually come to a point they already passed, interfering with themselves. As only constructive interference allows the state to persist, this gives rise to a discretisation of orbits reflected in the introduced Landau level number n.

Since the k_z dispersion is unaffected, all possible k_z states can be covered. At the same time, the discretisation of levels in the $k_\mathrm{x} - k_\mathrm{y}$ plane allows only states on individual rings [43]. Together this gives rise to tube shaped states in the Brillouin zone, called Landau tubes.

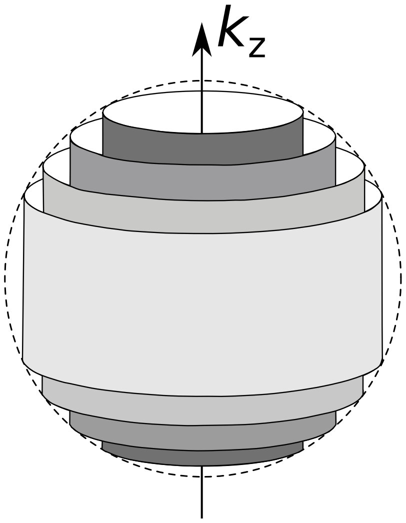

Figure 2.8.1. – Illustration of the Landau cylinders (grey) of which the Fermi surface (dashed sphere) is composed of in an applied magnetic field.

In a condensed matter system, a finite number of electrons occupies all states from zero energy up to some maximum known as Fermi energy. In k-space this gives rise to a sphere shaped equal energy contour at the Fermi wavevector called Fermi surface. While all possible states discretise into Landau tubes, so will the Fermi surface while its actual shape remains largely unaffected (see figure 2.8.1). Upon increasing the magnetic field, the energy of an individual Landau level will increase, causing the radius of the Landau tube to grow with it. Once one tube exits an area of the Fermi surface where there is an extremal cyclotron orbit, i.e. one enclosing an extremal crosssection, a sudden jump in the density of states of the material arises. Since the Landau tubes leave the Fermi surface one after another, there will be a periodic succession of jumps in the density of states, with a periodicity in $1/B$. This will cause all measureables of the material which depend on the density of states to vary periodically as well, the so called quantum oscillations.

The Onsager relation connects the frequency of the oscillations F with the enclosed extremal Fermi surface crosssection S perpendicular to the field direction such as [46]

$$S = F \cdot \frac{2\pi e}{\hbar} = F/10.476\,\mathrm{kT}\,\text{Å}^2. \tag{2.8.2}$$

The detailed influence of parameters such as temperature T, effective mass $m^* = m/m_0$ or scattering time τ on the amplitude of the oscillations A is described by the Lifshitz-Kosevich equation, which will be discussed in more detail in the following [47]

$$A = \sum_i \sum_{p=1}^{\infty} C_0 LK(B,T) D(B) B^{-\alpha} \cos\left(2\pi p \left(\frac{F}{B}\right) + \varphi\right). \tag{2.8.3}$$

Since the periodicity is in $1/B$ and, as will be shown, so is the field dependence of all the prefactors, it is convenient to replace the field B by its inverse $X = 1/B$:

$$A = \sum_i \sum_{p=1}^{\infty} C_0 LK(X,T) D(X) X^{\alpha} \cos\left(2\pi p\,(FX) + \varphi\right) \tag{2.8.4}$$

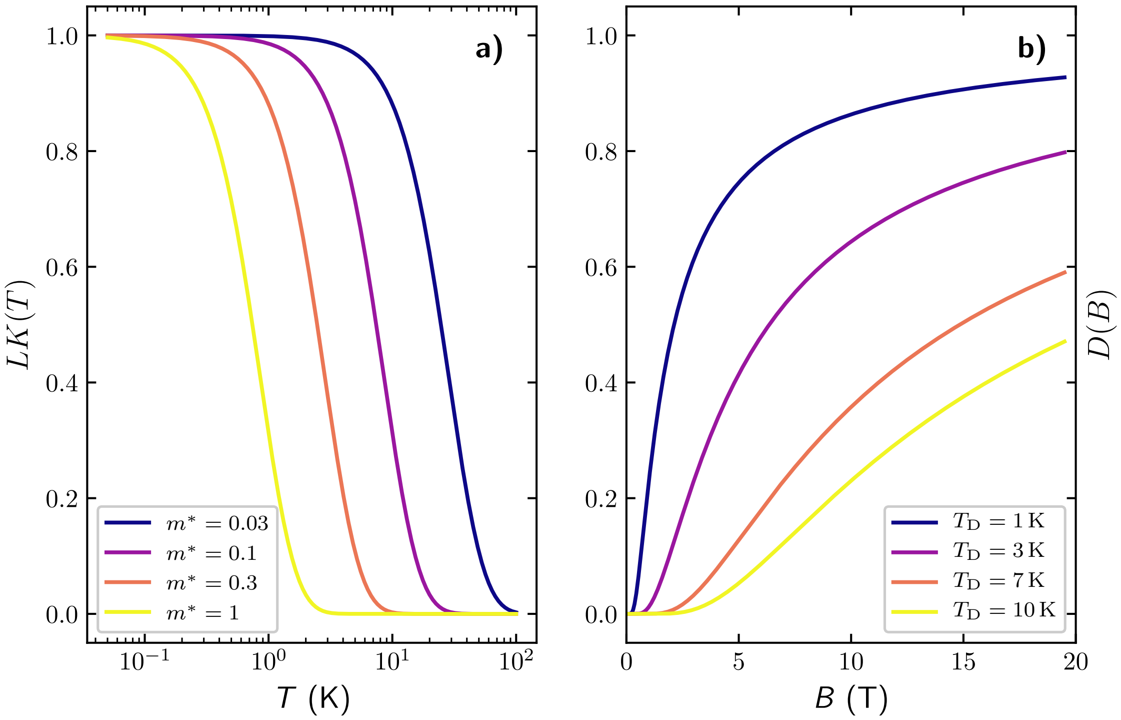

Figure 2.8.2. – a) Example of the influence of the effective mass on the amplitude of the quantum oscillations. A magnetic field of 5 T is assumed. b) The magnetic field dependence of the Dingle damping factor for various Dingle temperatures T_D and an effective mass of $m^* = 0.1$.

- The summation runs over the number of extremal orbits i and the harmonics of the oscillation p.

- C_0: This factor is field and temperature independent and unique to each individual orbit. It is proportional to

$$C_0 \sim \frac{F}{p^{3/2}\partial^2 S/\partial k_\mathrm{z}^2}. \tag{2.8.5}$$

The amplitude of the oscillations can be seen to be directly proportional to their frequency and to decay with increasing harmonic, i.e. the first harmonic should be the most pronounced.

The derivative $\partial^2 S/\partial k_\mathrm{z}^2$ describes the curvature of the Fermi surface at the extremal orbit. An almost cylindrical Fermi surface will have a small curvature resulting in an increased amplitude of the corresponding frequency. On the other hand, an ellipsoid with its long axis perpendicular to the applied field, will see the amplitude of the quantum oscillations to be suppressed by a rather large curvature at the extremal orbit.

- The exponent of the inverse field $X^{-\alpha}$ depends on the method used to detect the quantum oscillations. For example, $\alpha = 1/2$ if a magnetisation measurement is used. If the normalised electric conductivity of the sample $\delta\sigma/\sigma$ is investigated, this would be $-1/2$ [42].

- The term $LK(X,T)$ is occasionally denoted as the Lifshitz-Kosevich term, which describes the influence of finite temperatures on the amplitude of the quantum oscillations. If $T > 0$, the cutoff of the Fermi-distribution function is broadened, causing a blurring of the Fermi surface. This also smears out the change in the DOS when a Landau level is leaving the Fermi surface, resulting in a damping of the amplitude of the oscillations. The LK term depends on the temperature T, inverse field X and the effective mass of charge carriers m^* and is the Fourier transform of the derivative of the Fermi distribution function

$$LK(X,T) = \frac{2\pi^2 k_\mathrm{B} T m^* X/(e\hbar)}{\sinh\left(2\pi^2 k_\mathrm{B} T m^* X/(e\hbar)\right)}, \tag{2.8.6}$$

$$LK(X,T) = \frac{14.69 m^* T X}{\sinh\left(14.69 m^* T X\right)}. \tag{2.8.7}$$

  In the second line, the prefactors were contracted into the universal number 14.69, assuming a magnetic field in Tesla and temperature in Kelvin. The effective mass in this equation is the cyclotron mass $m^* = m/m_0 = \hbar^2/2\pi \cdot \partial S/\partial E_\mathrm{F}$, with the Fermi energy E_F. A plot of the temperature dependence of Eq. 2.8.7 can be seen in Figure 2.8.2 a). A lower effective mass allows the quantum oscillations to persist up to higher temperatures, since the Landau level spacing $\hbar \cdot eB/m^*$ remains comparable to the thermal energy $k_\mathrm{B}T$.

  If the temperature dependence of the amplitude follows the LK function, this is a proof of the existence of a Fermi liquid in the material investigated. On the contrary, if this is not the case such as in CeCoIn$_5$ [48] or PtCoO$_2$ [49], there is a deviation from the temperature dependence described by the LK function.

  The temperature dependence of the amplitude of a particular frequency can be used to extract the effective mass of the corresponding orbit.

- $D(X)$ is the so called Dingle term, which governs the field dependence and accounts for the influence of impurity scattering on the amplitude of the oscillations. The scattering of electrons from impurities causes their quantum mechanical state to have a finite lifetime τ. Heisenberg's uncertainty principle states that an uncertainty in time and energy is related such as $\Delta E\tau \geq \hbar/2$, therefore a shorter lifetime will result in an increased energetic width of the state. Since in a simple relaxation time model, the probability of a quasi particle to occupy an orbit is vanishing exponentially in time, the lineshape of the state in energy, i.e. its Fourier transform, is a Lorentzian. This will be the broader, the shorter the scattering time. This broadening of the Landau levels will now dampen the oscillations in a similar way as a 'blurred' Fermi surface will due to elevated temperatures. Since the field dependence of the amplitude is again the Fourier transform of the, Lorentzian, energy dependence, it is an exponential

$$D(X) = \exp(-14.69 \cdot m^* T_\mathrm{D} X). \tag{2.8.8}$$

Here the prefactors have already been contracted into the 14.69. T_D is the so called 'Dingle temperature' and depends on the scattering time such as $T_\mathrm{D} = \hbar/(2\pi k_\mathrm{B}\tau)$. It has the dimensions of a temperature and is expressed in units of Kelvin[6]. The field dependence of this factor can be seen in Figure 2.8.2 b). A shorter scattering time and therefore a higher Dingle temperature will result in the necessity of higher magnetic fields to make the oscillations observable. Since the amplitude of the oscillations depends exponentially on the scattering time, they are particularly susceptible to defects and impurities. Therefore, high quality single crystalline samples are are an essential requirement to observe the effect in the first place.

- What was not included in equation 2.8.7 is the influence of the electron spin. On top of the influence of the Landau quantisation onto the energy of the electrons, the Zeeman splitting acts such as

  $$\Delta E_\mathrm{S} = g\mu_\mathrm{B}B = g\frac{e\hbar}{2m^*}B. \tag{2.8.9}$$

  Since the energy splitting due to the Landau quantisation, $\Delta E_\mathrm{L} = \hbar\omega_\mathrm{c} = e\hbar B/m$, is of the same field dependence if $g = 2$, both contribute the same energy. Therefore, the spin-up state of the n-th Landau level will have the same energy as the spin-down state of the $(n-1)$-level, which is why the influence of spin-splitting is not be observable in most cases. If, however, $g \neq 2$, the Landau levels will split according to their spin. If their index is still large (i.e. at low fields relative to the quantum oscillation frequency) the splitting might not be observable directly and only give rise to an additional amplitude factor $\cos(1/2\ \pi g m^*)$. This was of no relevance in this work and was therefore omitted in equation 2.8.7.

---

[6] Although, googling 'Dingle temperature' will mostly result in the answer '10 °C, rainy'.

However, as the cosine might change its sign, it might contribute to the phase of the oscillations.

- Finally, there is the phase of the quantum oscillations, φ. In a 3D system with a quadratic dispersion, this can be computed such as

  $$\varphi = \frac{1}{4} \pm \frac{1}{4} + \gamma$$

  The ± is the sign of the cosine of the spin-splitting term described above, which is -1 in a system with $g = 2$ and $m^* = 1$. The factor γ is the so called Onsager phase factor. In a system with quasiparticles of a finite mass, this can acquire values of 3/8 or 5/8: It is 3/8 when the extremal orbit is from electron-like quasiparticles around a minimal orbit (also referred to as a 'neck') or a hole-like maximal orbit ('belly'). Opposite, it is 5/8 for an electron 'belly' or hole 'neck'.

  In systems with massless quasiparticles, i.e. with linear dispersion such as Weyl-systems the situation is less straightforward and still subject of ongoing research. In the simplest picture of a spherical Fermi surface around a single Weyl point (see section 4.1.2), an additional phase of π is introduced into γ when the charge carriers complete an orbit. This results in γ to be $\pm 1/8$ depending on electron or hole like quasi particles. If the Fermi energy is moved away from the Weyl points causing the individual pockets to merge, or the Fermi surface pocket is somewhat deformed, any other phase can be acquired [50]. In general, the phase of the quantum oscillations in systems with chiral dispersion is a topic still under investigation and beyond the scope of this work.

In summary, large amplitudes can be expected by measuring at low temperatures relative to the temperature dependence of the LK function, in high magnetic fields and on samples which are as perfect and defect free as possible. This explains the wide use of this effect in the study of semimetals where the relative size of the oscillations of the density of states is large compared to the total one, such as in this thesis.

2.8.2. Data analysis

While the experimental challenges in the measurement of quantum oscillations might be appreciable in most cases, careful data analysis is also required. The procedures used and their background will be discussed in the following section. The example of a magnetisation measurement was chosen to illustrate the process.

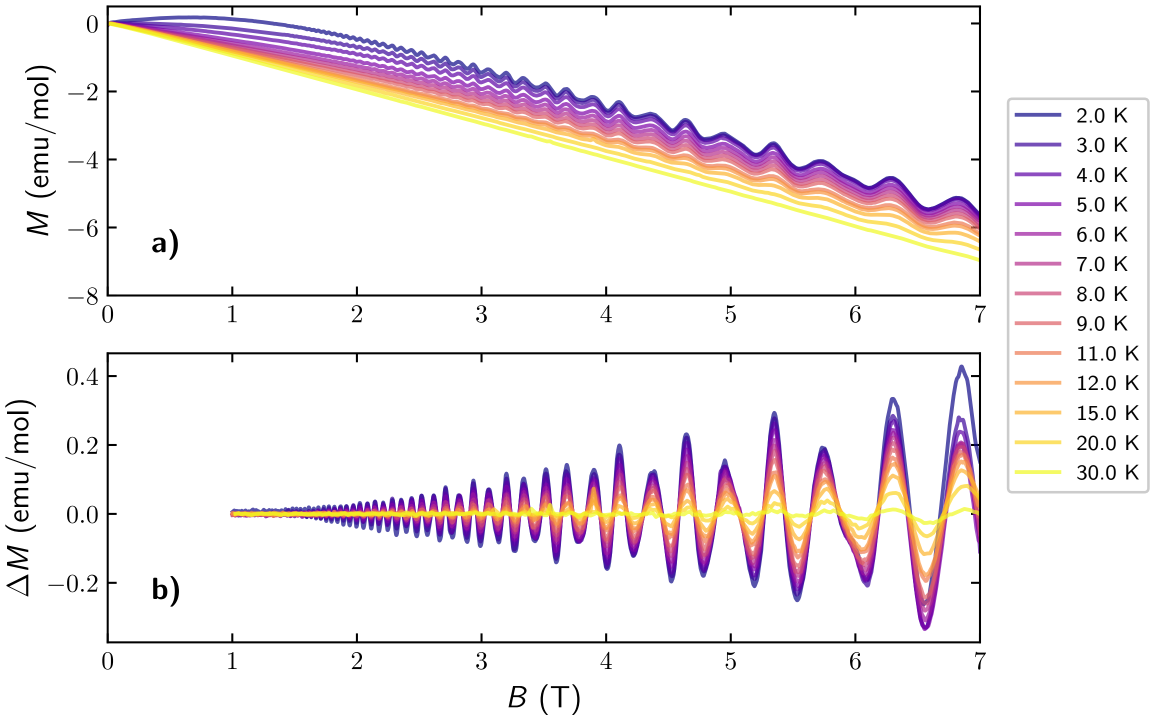

Figure 2.8.3. – Example of a possible signal, magnetisation vs. magnetic field in this case, being superimposed by quantum oscillations (a). Panel b) shows the oscillations after subtraction of a suitable background (see text).

Background

A typical example of magnetisation M vs. magnetic field B curves at various temperatures is shown in Figure 2.8.3 a). This measurement was done on a crystal of $CoSb_3$ by coworker Dan Sun while data analysis was entirely done by the author. The signal is a superposition of various contributions:

- Contributions typically referred to as ’background’. If the resistivity of a sample is measured, it might arise from the magnetoresistance. In measurements of the magnetisation, as shown here, some dia- or even paramagnetic contributions are typically present.
- The second contribution to the signal shown in Figure 2.8.3 a) is the oscillatory component ΔM which are the quantum oscillations shown in panel b).

To allow for the analysis of the quantum oscillations, the background is subtracted. In resistivity measurements this is mostly accomplished by fitting a polynomial and subtracting it. In this particular case, the background is a superposition of para-and diamagnetism, which is why a Brillouin function is fitted and subtracted since it accounts much better for the background than a polynomial (see Eq. 4.2.1 and Sec. 4.2.3).

The oscillatory component of the magnetisation, isolated by subtracting the background, can be seen in figure 2.8.3 b). The increasing amplitude in field is clearly observable. It is a combined result of the influence of the Dingle term, the field dependence of the LK term and the $B^{1/2}$ in equation 2.8.3. The damping of the oscillations with increasing temperature can also be seen.

Fourier transform

Since the signal is clearly a superposition of various frequencies, the decomposition is typically done via a Fourier transform. A nice introduction into this and the broader field of signal analysis is given in [51]. If $g(t)$ is a signal, its Fourier transformed $\tilde{g}(f)$ can be calculated such as [40]

$$\tilde{g}(f) = \frac{1}{\sqrt{2\pi}} \int_{-\infty}^{\infty} g(t) \mathrm{e}^{-\mathrm{i}ft} \mathrm{d}t = \mathcal{F}(g(t)). \tag{2.8.10}$$

$\tilde{g}(f)$ is referred to as the frequency- or Fourier spectrum of $g(t)$, which is a complex number in most cases. Typically, its absolute value $|\tilde{g}(f)|$ is plotted. In contrast, $|\tilde{g}(f)|^2$ is the power spectrum, and likewise $\int |\tilde{g}(f)| \mathrm{d}f$ is the energy radiated by the signal.

When working with Fourier transformations, it is helpful to remember some of its mathematical properties [51]. Let $g(t)$, $h(t)$ be functions in real space and $\tilde{g}(f)$, $\tilde{h}(f)$ their Fourier transformed. Further, ξ is an arbitrary constant and $*$ denotes a convolution.

- Linearity:

$$\xi\mathcal{F}(g(t) + h(t)) = \xi\tilde{g}(t)) + \xi\tilde{h}(t)) \tag{2.8.11}$$

- Equivalence of multiplication in real space and convolution in Fourier space:

$$\mathcal{F}(g(t) \cdot h(t)) = g\tilde{(t)} * \tilde{h}(t)) \tag{2.8.12}$$

Also, it is useful to remember the Fourier transform of certain functions [51]:

- Let $\mathrm{rect}_a(t)$ be the rectangle function of total length a, which is 1 where $|t| < a/2$ and zero anywhere else (blue curve in figure 2.8.4 a), here, shifted by half its width), then

  $$\mathcal{F}(\mathrm{rect}_a(t)) = a \cdot \mathrm{sinc}(af), \tag{2.8.13}$$

  $$\mathrm{sinc}(f) = \frac{\sin(\pi f)}{\pi f}. \tag{2.8.14}$$

  The sinc function shows an oscillatory behaviour and is shown in figure 2.8.4 b). The first root is at $\pm 1/a$.

- The Fourier transform of an exponential decay $\exp(-2\pi \cdot k_0 \cdot t)$, with k_0 being a constant is

  $$\mathcal{F}(\exp(-2\pi \cdot k_0 \cdot t)) = \frac{1}{\pi} \cdot \frac{k_0^2}{f^2 + k_0^2}. \tag{2.8.15}$$

  This is a Lorentzian function. The width of the Lorentzian is defined by the decay constant of the exponential.

- Finally, the Fourier transform of a sine or cosine with frequency f:

  $$\mathcal{F}(\sin(2\pi f_0 t)) = \delta(f - f_0). \tag{2.8.16}$$

  This is a delta function at the frequency of the sine or cosine.

Since data is processed and stored digitally, with a discrete sampling in B, the actual transformation is done using a Fast Fourier Transformation algorithm, short FFT.

Let a sinusoidal signal with a frequency f be recorded over a finite length in time a. Its Fourier transform is equivalent to a transform of a sine multiplied by a rectangle function of width a. Therefore, the transformed signal is a convolution of a delta-function and a sinc, i.e. a sinc centred at the frequency of the sine. Since the first root of the sinc is at $1/a$, the frequency resolution can be seen to be inversely proportional to the length of the signal.

Typically, the signal is cropped to a certain limited range. If a good frequency resolution is sought, the inverse field window will be extended as far as possible towards higher X. Since there are no oscillations at low fields or high X, this will reduce the weight of the oscillations in the FFT window, causing the peaks in the spectrum to shrink and eventually vanish in the noise floor. If not the frequency resolution is of importance, but the intention is to follow an amplitude as far as possible in temperature to conduct an analysis of the effective mass, the FFT window will be

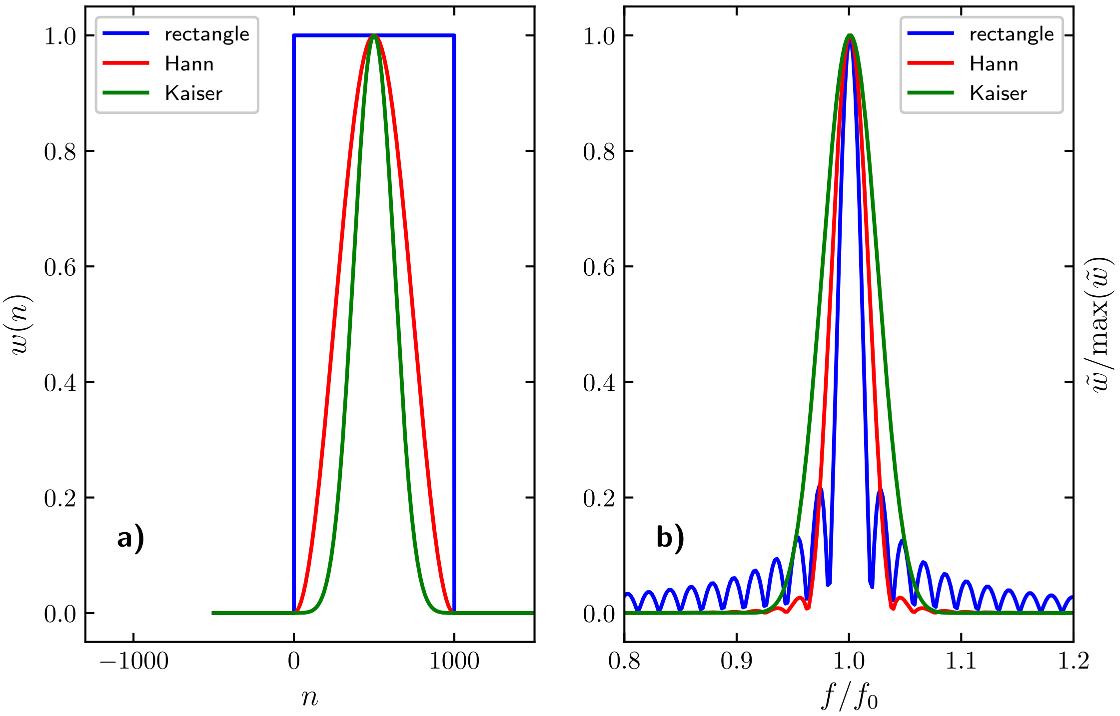

Figure 2.8.4. – Panel a): Shape of the window functions mentioned in the text for a signal of length $N = 1000$. Panel B: FFT lineshape resulting from various window functions. For the Kaiser window, $\alpha = 5$ was chosen.

restricted to highest fields. Thus, the maximum amplitude of the oscillations can be kept within the window.

The minimal and maximal inverse field values used for the FFT will be denoted as X_{min} and X_{max} respectively. Just cropping the signal would result in the introduction of the sinc-function to the transformed as described above. This comes along with strong side-lobes, smaller peaks next to the main FFT peak, which might be mistaken for additive quantum oscillation frequencies (see figure 2.8.4 b)). To avoid these, the signal can be multiplied by a so called window function before the FFT is performed. Window functions are similar to box function, put reduce the signals amplitude smoothly to zero at both their ends[7].

---

[7] This is not true in the general case, since the window does not have to be symmetric. In the course of this thesis only symmetric windows were used, however, so called T2-filtering was tried without any improvement.

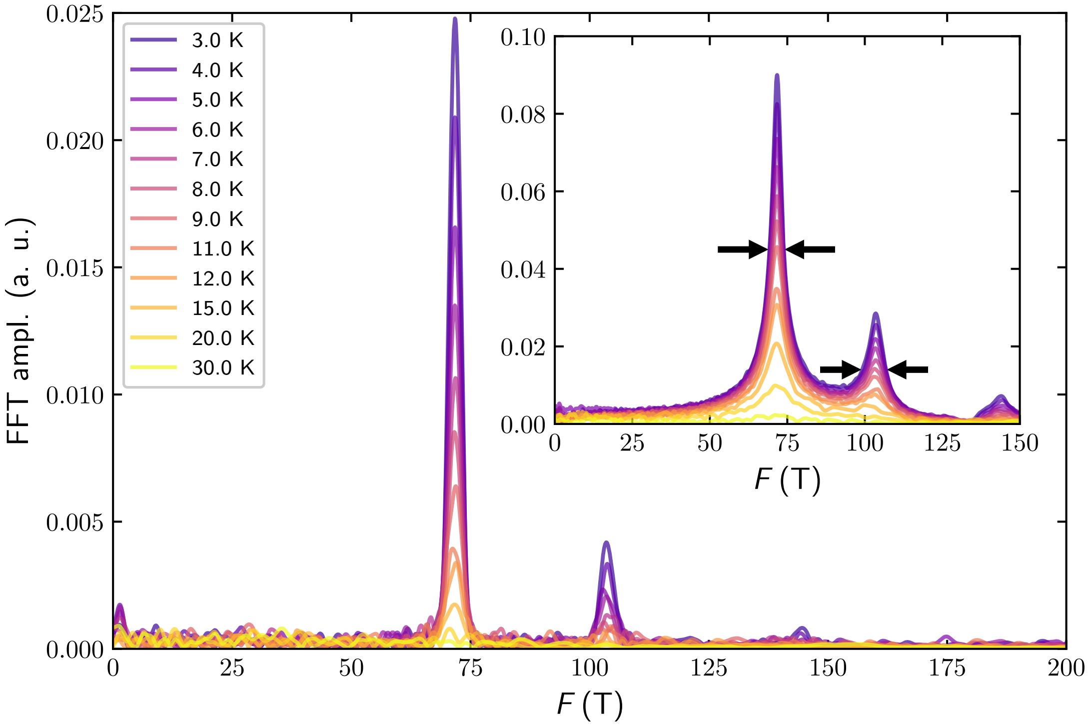

Figure 2.8.5. – FFT of the signal shown in figure 2.8.3. The main plot was made using a Kaiser window with $\alpha = 5$. The insert was made for the Dingle analysis, without any window function but by additionally multiplying the signal with a factor $\sqrt{B}$ (see equation 2.8.7).

Out of the large set of available window function, mostly the *Hann* window (also referred to as 'Hanning') and the *Kaiser* window were used in the course of this thesis. For a signal consisting of a discrete number of points N they are defined as [52]:

$$w_{\text{Hann}}(n) = \sin^2\left(\frac{\pi n}{N-1}\right), \tag{2.8.17}$$

$$w_{\text{Kaiser}}(n) = \frac{I_0\left(\pi\alpha\sqrt{1-\left(\frac{2n}{N-1}-1\right)^2}\right)}{I_0(\pi\alpha)}. \tag{2.8.18}$$

Here, n denotes the index of the point, I_0 the zeroth order modified Bessel function and α is an adjustable index. The higher the α value, the higher the side-lobe suppression and the poorer the frequency resolution. Mostly, $\alpha = 5$ was used as a good compromise. The window functions and the resulting line shapes can be seen in figure 2.8.4 a) and b), respectively. In general, there was no relevant difference between the windows, however, cross-checking by using different window functions was done whenever some ambiguity arose.

Another useful tool when working with FFTs is called *zero padding*. After the signal is multiplied with the window function, a series of zeros is appended to it, e.g. tenfolding its length. This results in an artificial increase in spectral resolution, making the interpretation of the frequency spectra easier.

With this knowledge, the FFT of the signal shown in figure 2.8.3 can be calculated and is depicted in figure 2.8.5. Clearly, two frequencies at $F_1 = 72\,\mathrm{T}$ and $F_2 = 103\,\mathrm{T}$ can be distinguished with amplitudes A_1 and A_2 respectively. The additional peak at 144 T is the second harmonic of the lower frequency.

Analysis of the effective mass

Since the signal is decomposed into its parts, their amplitudes A can be followed in temperature. One possibility to extract the effective mass from the temperature dependence of A is to fit the $LK(X_0,T)$ function shown in Eq. 2.8.7 multiplied with a prefactor ξ to account for the size of the amplitude

$$A(T) = \xi LK(X_0,T) = \xi \frac{14.69 m^* T X_0}{\sinh(14.69 m^* T X_0)}. \tag{2.8.19}$$

The magnetic field value to enter into this fit is the average inverse field $X_0 = \frac{1}{2}(X_{\mathrm{min}} + X_{\mathrm{max}})$ of the FFT window and ξ and m^* are free parameters. This procedure is widely used in the analysis in the literature. However, problems arise if the envelope of the signal has a strong field dependence within the window, e.g. as shown in figure 2.8.3.

This effect was first taken into account by J.-F. Mercure in his PhD thesis[8][40]. If the amplitude of the envelope varies strongly in the FFT window, the majority of the signal will not stem from the average inverse field X_0

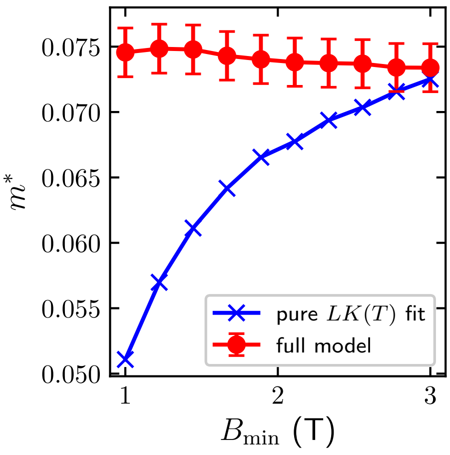

Figure 2.8.6. – Effective mass of the 72 T component of the signal depicted in figure 2.8.3, as determined by an analysis using a FFT window of B_{min}-7 T. In blue, extracted from fitting the LK term only (Eq. 2.8.19). In red by taking the window and Dingle factor into account (Eq. 2.8.22)

---

[8] I am indept to Dr. J. Klotz for pointing me to this thesis.

but rather be shifted to higher field values or lower X. This is mainly due to the field dependence of the Dingle term. Here, the signal decays more slowly in temperature, as though the effective mass of the charge carriers is lower. If this is not accounted for, the effective mass can be underestimated by as much as 50 %.

To avoid this, Parsevals theorem can be used, which relates the amplitude of a signal in real space $g(t)$, to its amplitude in Fourier space $\tilde{g}(f)$. It states

$$\int_{-\infty}^{\infty} |\tilde{g}(f)|^2 \mathrm{d}f = \int_{-\infty}^{\infty} g(t)^2 \mathrm{d}t. \tag{2.8.20}$$

From a different point of view, Parsevals theorem reflects the energy conservation in the time and frequency domain. No matter which basis is chosen for the description of a signal, whether the time integrated power or the frequency integrated spectral power density, both should be equal.

This can now be applied to the problem of the analysis of the effective mass. If the time domain is associated by X and the frequency domain by the quantum oscillation frequency F, we arrive at

$$\int_{0}^{\infty} \mathcal{A}^2(F)\mathrm{d}F = \int_{X_{\mathrm{min}}}^{X_{\mathrm{max}}} w^2(X)C_0^2D^2(X)LK^2(X,T)X^{-2\alpha}\cos^2(2\pi(FX+\gamma))\mathrm{d}X \tag{2.8.21}$$

Here, the integration boundaries in F were restricted to the single sided spectrum and those in X to the actual inverse field interval. Again, $w(X)$ denotes the used window function. In order to fit the effective mass, there is no interest in absolute values of the amplitude, but only in field or temperature dependent contributions. Therefore, C_0 can be omitted. Given its periodicity, so will be the cosine, under the assumption of a sufficiently large frequency.

The field dependence of the $X^{-\alpha}$ term will also be neglected: As will be shown later, the final procedure will result in a slight overestimation of the effective mass. The factor α is known to be $1/2$ in a magnetisation measurement, and would therefore be straightforward to include. However, if resistivity is measured, in e.g. a system with $\rho_{\mathrm{xx}} \sim \rho_{\mathrm{xy}}$ but the Hall component was not determined simultaneously, the tensor inversion to arrive at σ_{xx} is not possible. This leaves α undefined. Given these possible hurdles and inconsistencies in the analysis between different methods (include it in measurements of M, not include it in measurements of ρ) and the only minor influence on the final result, this factor will be omitted. This leaves only the window, Dingle and Lifshitz-Kosevich term on the right hand side of the equation.

On the left hand side, an integral over the full power spectrum would be required. In reality, there might be multiple frequencies, restricting it to an integral over the actual line in the FFT within some interval to recover the 'energy' radiated by the frequency[9]. Once the LK function gets sufficiently small in T, this might be difficult since noise and FFT artefacts will alter the line shape, making the integration error prone. To avoid this, the area under the line is approximated by the peak height of the line in the FFT, A. Upon testing this against simulated data, this was found to underestimate the actual energy of the line at high temperatures, since the line broadens slightly. Underestimating the actual energy of the line, means it decays more quickly which is equivalent to a higher effective mass. With simulated data this effect was found to account for an overestimation of $\leq 2.5\,\%$. This is considered to be a sufficient accuracy.

All things can be combined to arrive at the new fit function of the effective mass, where again, ξ denotes a prefactor accounting for the actual size of the amplitude

$$A^2(f_0) = \xi \int_{X_{\min}}^{X_{\max}} D(X,T_{\mathrm{D}} \cdot m^*)^2 LK^2(X,T,m^*) w^2(X) \mathrm{d}X \tag{2.8.22}$$

Only ξ and m^* were treated as free parameters. The effective mass in the Dingle term, entering via $T_{\mathrm{D}}m^*$ was kept constant, for reasons which will become clear later.

The effective mass of the 72 T orbit, as determined by Eqs. 2.8.19 and 2.8.22 from the exemplary data presented in figure 2.8.3, can be seen in figure 2.8.6. The mass is shown for various window sizes, ranging from 1-7 T to 3-7 T. Both analysis procedures seem to converge for increasing $B_{\min}$ at a mass of about $m^* = 0.073$, since the field dependence of the amplitude vanishes for this limes. A slight window-size dependence remains with the usage of 2.8.22, which is why the aforementioned ~2.5 % of error are taken as uncertainty of the method and are illustrated by the error bars.

Since it includes the Dingle term $D(X)$ it requires the knowledge of the Dingle temperature, or at least, the product $T_{\mathrm{D}} \cdot m^*$. In reality, however, the dependence of the effective mass on the assumed $T_{\mathrm{D}}m^*$ is rather small, and an educated guess which tends to underestimate it will already yield good results with errors below 5-10 %. This insight was gained from running the described analysis procedure against simulated data. In a real experiment with noisy data, the upper boundary is probably a reasonable estimate of the uncertainty of the effective mass as determined by this method.

---

[9] The term 'energy' will be used for the integral over the spectral power density. This is technically not correct, since the quantum oscillations do not radiate any energy, but will be used nevertheless to stick to the vocabulary used in signal processing.

Analysis of the Dingle term

The analysis of the Dingle term for a system with a single frequency is rather straightforward: After dividing off the LK and B^{α} term, the amplitude $A'(X)$ can be extracted manually or by means of a MATLAB script. Due to the exponential in D, $\ln A'(X)$ should be linear in X, with the slope corresponding to $14.69m^{*}T_{\mathrm{D}}$ (see Eq. 2.8.8). Converting this into the Dingle temperature should be straightforward, once the effective mass is known. Alternatively, this will yield the product $T_{\mathrm{D}}m^{*}$, which is sufficient for the mass analysis.

If there is more than one frequency present, this method cannot be applied directly. Two other ways were used:

1. If both frequencies are sufficiently distinct and the signal to noise ratio is good, the signal can be filtered. By applying a bandpass including only one frequency and a consequent inverse FFT, the problem of the single frequency is recovered. Care has to be taken to not introduce artefacts from the FFT filtering procedure.

2. Another way is to look at the line shape of the FFT. If the LK and B^{α} terms are divided off, only the exponential of the Dingle term is governing the amplitude. If the FFT is performed without any window function, this should result in a Lorentzian line shape. Since its full width at half maximum (FWHM) Δf_{FWHM} is related to the decay constant of the exponential it can be used to extract T_{D} via

   $$T_{\mathrm{D}} = \frac{\pi \Delta f_{\mathrm{FWHM}}}{14.69m^{*}}. \tag{2.8.23}$$

   Care has to be taken to choose X_{max} such, that the signal has fully decayed. Otherwise, this is equivalent to the multiplication with a rectangle function, which would introduce a sinc, artificially broadening the linewidth.

   The downside of the method is the always present noise. Since the LK function is very small at low fields, dividing by it will increase the amplitude of the noise at low fields considerably. This again appears as a rectangle function in the FFT and broadens the linewidth, giving rise to uncertainties of around 50 %.

   It should be kept in mind, that trying to extract the Dingle temperature from a typical measurement, which comes along with multiple frequencies and low signal to noise ratios is error prone to a large extend. The only reasonable use is mostly as an input parameter for the analysis of the effective mass and to get an idea of the order of magnitude of the scattering times or mean free paths.

3 | Methods

3.1. Resistivity measurements

In chapter 4, results on the longitudinal magnetoresistance in TaAs-type Weyl semimetals are presented. In this chapter, the necessary sample preparation and measurement methods are discussed, as well as simulations done to aid the interpretation of the acquired data.

In order to study the resistivity of a sample in an experiment, a standard four-point measurement is typically used to avoid the influence of contact resistances. If additional contacts are added to measure the Hall voltage, this is referred to as a six-point measurement depicted in figure 3.1.1.

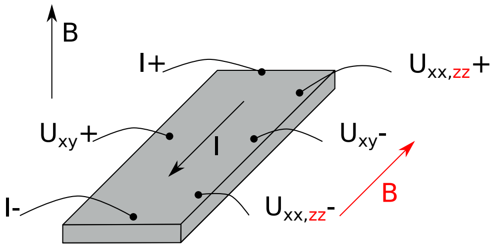

Figure 3.1.1. – Schematic illustration of a six-point measurement.

While the geometry for the measurement of all components of the resistivity tensor might be clear in theory, real contacts and their alignement on the sample are never perfect. This can lead to an intermixing of, e.g. the Hall voltage into ρ_{xx} (and vice versa), such that the measured signal ρ'_{xx} is an admixture of both ρ_{xx} and ρ_{xy}, $\rho'_{\mathrm{xx}} = \rho_{\mathrm{xx}} + \xi\rho_{\mathrm{xy}}$. Here, the prime denotes the measured signal and ξ some small number scaling the arbitrary admixture. To correct this, the magnetic field is swept to both polarities, and the symmetry of the signals is used: While the ρ_{xx} is symmetric under field inversion, the ρ_{xy} is antisymmetric. The true ρ_{xx} and ρ_{xy} can therefore be recovered as:

$$\rho_{\mathrm{xx}} = \frac{1}{2}(\rho'_{\mathrm{xx}}(B^+) + \rho'_{\mathrm{xx}}(B^-)) \tag{3.1.1}$$

$$\rho_{\mathrm{xy}} = \frac{1}{2}(\rho'_{\mathrm{xy}}(B^+) - \rho'_{\mathrm{xy}}(B^-)) \tag{3.1.2}$$

$$\tag{3.1.3}$$

The superscript + and - denotes the magnetic field values at positive or negative polarity.

3.1.1. Measurement setup

In most cases, measurements were performed with Stanford Research SR830 and SR850 Lock-In amplifiers at frequencies between 10 Hz and 20 Hz. The internal oscillator was used as current source, with currents of about 5 mA as adjusted by the oscillator voltage and a 1 kΩ pre-resistor. For microstructured samples of NbAs, an excitation of 100 µA was used.

The sample environment, regarding temperature and magnetic field was mostly provided by a Quantum Design PPMS, where measurements down to 2 K and up to 14 T were possible. Around the sample, a residual helium atmosphere of about 1 mbar served as exchange gas.

Angle dependent measurements were performed using a computer controllable in-situ rotation stage with an angular resolution of 0.5°. When performing field sweeps at different angles, this was done at decreasing angles only to avoid lag in the rotator gears.

3.2. Field-induced anisotropic conductivity

The resistivity measurement described above relies on a homogeneous current distribution within the sample. This means, the equipotential surfaces of the electrical potential are parallel to the cross section of the sample. In figure 3.2.1 a) this is shown schematically. The current is injected through point shaped contacts into a bar shaped sample. Since the isotropic case is shown with the conductivity anisotropy $A = \sigma_{\mathrm{zz}}/\sigma_{\mathrm{xx}} = 1$, the current homogenises quickly and flows homogeneously from one current contact to the other. The voltage contacts would sit on top of the sample and pick up the potential difference. This is an illustration of a typical transport measurement.

However, in the 1950s the study of the magnetoresistance in the longitudinal configuration in materials such as antimony showed unexpected results: Some materials appeared to show a so far unexplained negative longitudinal magnetoresistance [53]. This was later explained by K. Yoshida with strong current inhomogeneities [54, 55, 56, 11].

The transverse conductivity in a compensated system scales as $(\mu^2 B^2)^{-1}$ (see chapter 2.1.2) while the longitudinal conductivity changes only very little. This induces a strong conductivity anisotropy, where $\sigma_{\mathrm{zz}}/\sigma_{\mathrm{xx}}$ can reach values up to 1000 or higher [2]. If the current is injected through a point like contact it cannot spread through the width of the sample to achieve a homogeneous current distribution once the field and

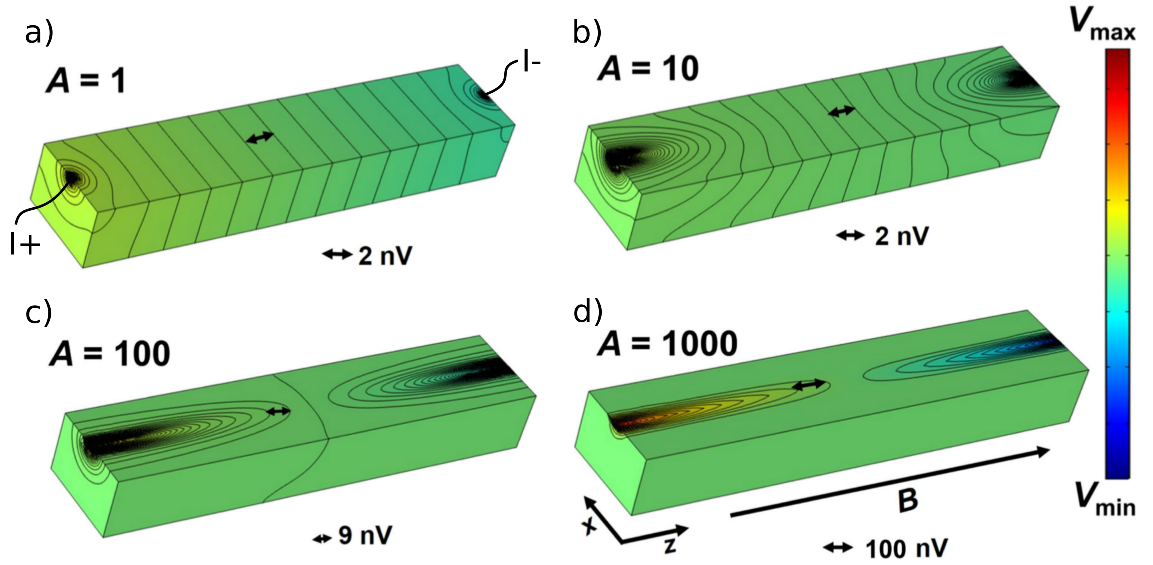

Figure 3.2.1. – Illustration of the current jet originating from a point like current contact on the surface of a sample. Figure taken from [57].

therefore resistivity anisotropy is high enough (see figure 3.2.1). The evolution of this process with increasing conductivity anisotropy is illustrated in figure 3.2.1 a) to d).

Upon a modest anisotropy of $A = 10$ as shown in b), the distortion of the equipotential lines is already visible. Increasing it to 100 (c) and beyond (A =1000, d)) causes the potential drop at the edge of the sample to vanish. Here the current is focused on a narrow jet travelling from each current contact along the magnetic field direction. If a voltage contact was positioned at the edge of the sample, current density would be moved away from it upon increasing the field. Since Ohm's law applies locally, this results in the recorded potential difference to drop dramatically. In consequence, the experimentator will *perceive* the decreasing 'resistivity'[1] as a negative longitudinal magnetoresistance. Meanwhile, in a typical experiment the current through the sample is kept constant. Therefore, the decreasing current densitiy in some parts of the sample finds its counterpart in an increasing current density within the jet. This can be seen in the colour coded high density of equipotential lines in figure 3.2.1 d), which might be perceived as a strong increase in 'resistivity' [11, 54, 55, 56, 57].

In the following, the resistivity anomaly caused by an inhomogeneous current distribution as described above will be referred to as 'current jetting'.

---

[1] The term 'resistivity' in apostrophes will be used in the following, to indicate that this is voltage divided by current and some geometry related factor, but does not correspond to the true ρ_{zz} of the material.

3.2.1. Current jetting in Weyl semimetals

Since the chiral anomaly described in section 2.7 should appear as a negative longitudinal magnetoresistance, the latter was sought after and found soon after the discovery of Weyl semimetals in TaAs [38, 33]. However, doubts regarding the interpretation as chiral anomaly were raised when a negative LMR was found in TaP [12]. Here, the Fermi energy lies such that there are no independent Weyl points, thus there is no well-defined chirality and chiral effects should be absent[2]. In this and a following publication it was shown, that the conductivity anisotropy in these high mobility materials leads to strong current jetting effects [12, 57]. The observed negative longitudinal magnetoresistance in NbP and TaP can be very well explained with these current inhomogeneities, as was shown by simulations of the potential distribution, depicted in figure 3.2.2. This shows the example of a measurement on NbP with two pairs of voltage contacts, V_1 and V_2. While V_2 is situated 'above' the line of the current contacts, V_1 is on the opposite side of the sample. In an experiment, both voltages increase up to some point, before they decrease to some low saturation value. This can be explained by calculations of the current distribution in the sample: At low fields, the focusing of the current leads to a strongly increasing voltage in both contacts, more pronounced and up to higher fields in V_2, since it is situated closer to the current contacts. Increasing the field narrows the jet and removes current density from the contacts; first from V_1 at a few mT and at about 750 mT also at V_2. Finally, the voltage appears to run into some saturation, probably because the anisotropy of the resistivities increases more slowly at highest fields.

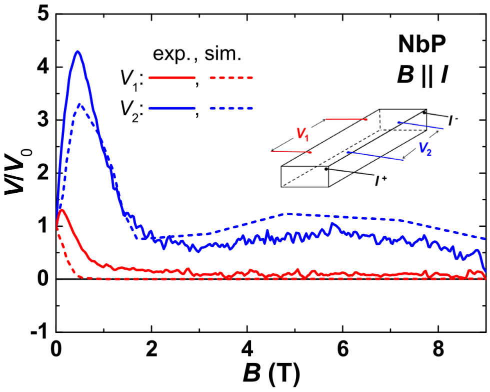

Figure 3.2.2. – Simulated and experimental longitudinal magnetoresistance of NbP for the contact geometry shown. Graphic taken from [57].

3.2.2. Influence of contact geometries

The main strategy to avoid the experimental artefact described in the previous subsection was to make soldered current contacts, covering the full cross section of the sample, which inject the current as homogeneous as possible. If current and field are

---

[2] A more detailed discussion on the dependence of the size of the chiral anomaly on the Fermi energy can be found in section 2.7.1.

aligned, the jet should have the size of the sample which is then equivalent to an almost homogeneous current distribution. However, it was realised that the process of soldering was tedious, often leaving small sections of the cross section un-contacted. Also, the data presented in chapter 4 suggests a still inhomogeneous current distribution within the sample. Therefore, simulations were performed to try and understand how slightly imperfect current contacts influence the potential distribution and what vestigial of the true intrinsic longitudinal magnetoresistance remains in the signal.

For this, self written code in Matlab was used. The calculation is based on a finite-difference approach to solve the 3D Laplace equation for the potential field on a discretised lattice. Details of the algorithm can be found in appendix A.3. For calculations depicted in figure 3.2.3, the size and voltage contact geometry of a bulk sample of NbAs with current along *a* was used. The sample had a size of 1600 µm x 540 µm x 240 µm. The transverse conductivity was taken from measurements on a different sample and the longitudinal conductivity assumed was from our measurements on a microstructured sample. Since only qualitative conclusions were to be drawn from these simulations, minor differences in resistivities between various samples were not of any relevance here.

In figure 3.2.3 top the resulting potential distribution as equipotential surfaces in a field of 10 T, corresponding to a conductivity anisotropy of 840, can be seen. The dots denote the voltage tap positions in the colour corresponding to the curves in the bottom panel and in grey the current contact area is shown. The latter was chosen such that a realistic imperfection is reflected. For example, the edges of the sample are never perfectly sharp, therefore there should always be a rim around which is not contacted. What is more, it is occasionally difficult to wet the whole width of the sample with solder (see section 3.3 for the contacting method). Therefore, a reasonable imperfection of the current contact would be one that leaves about a quarter of the sample width empty. While in figure 3.2.3 A one contact, I-, is almost perfect apart from a rim along the edges, I+ covers only about 3/4 of the width of the sample. In B, both cover about 3/4, however, they are arranged such that they don't face each other.

There are not only imperfections in current contacts. The voltage contacts can also be misaligned relative to the samples long axis. An example of this is the difference between U3 and U4. They reflect the uncertainty in determining the precise position of the contact area and the influence of a transverse offset of voltage contacts. For this, the voltage contact U3- is offset by about 40 µm to the left, and U4 is determined by the difference between U3+ (green) and U4 (purple).

At the bottom, the resulting 'resistivities' from the voltage contact pairs are presented. They can be compared to the actual ρ_{zz} from the measurement on the microstruc-

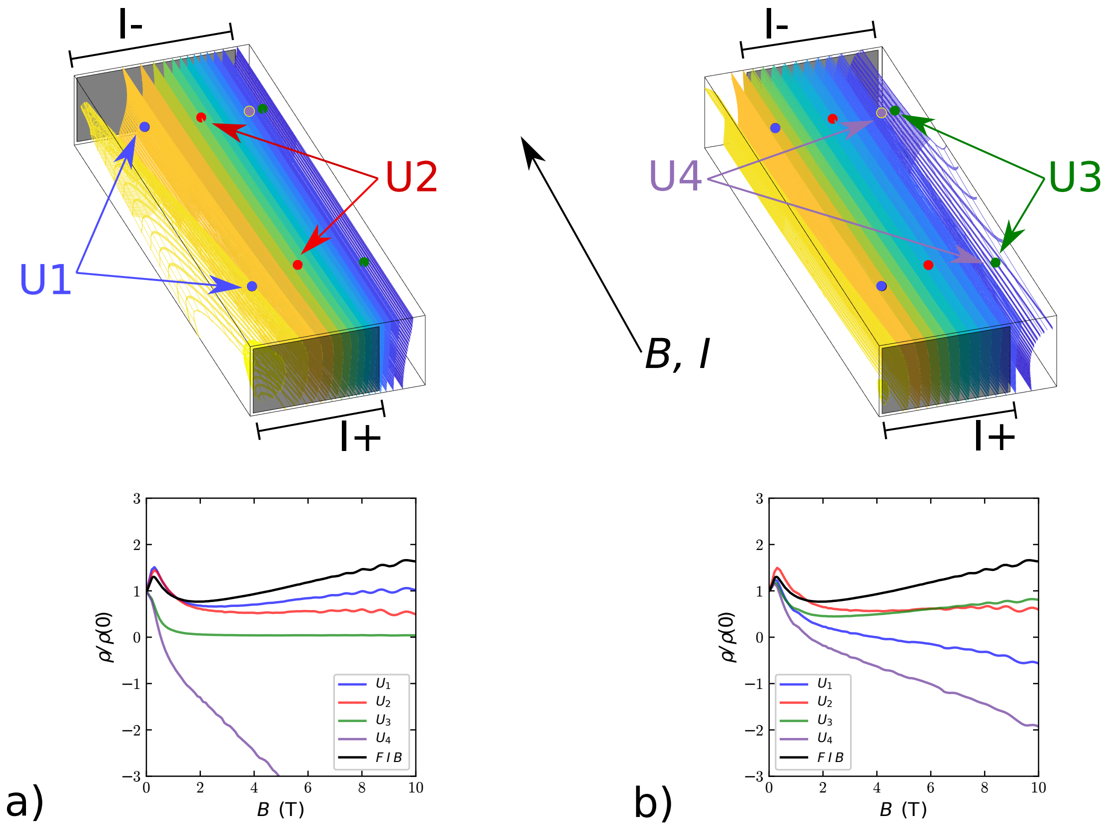

Figure 3.2.3. – Potential distribution in a sample of NbAs (top) and resulting 'resistivities' (bottom) for two different current contact geometries. **A:** I- covers almost the whole width of the sample, I+ around 3/4. **B:** Both contacts cover only about 3/4 of the sample, but displaced such they are not facing each other. In black, the actual longitudinal magnetoresistance assumed for the measurement is shown.

tured samples (FIB), i.e. the 'real' longitudinal magnetoresistance in this simulation, shown in black. The real experimental results are shown in figure 3.2.4.

In both cases, the main potential drop is across the width of the sample rather then across its length. In a) a jet like equipotential surface can be seen on the left side (in yellow) reaching from one contact to the other. Still, the perpendicular potential drop does not imply the main current to be directed perpendicular to the samples main axis. Since Ohms' law applies locally, the local current density is the gradient of the potential divided by the resistivity. Since the latter is strongly anisotropic and rather large perpendicular to B, the current density component along this direction might be small. Still, the primarily perpendicular potential drop explains, why all resulting 'resistivities' shown in the bottom panel are lower than the actual one. A special case is U4. This contact pair is misaligned perpendicularly and therefore picks up the magnitude of the perpendicular potential drop. However, due to the particular geometry chosen it becomes negative around 1 T. This is similar to what was seen in the measurement depicted in figure 3.2.4, which resembles the contacts U1, 2 and 4.

In panel b), the alignment of the current contacts further facilitates the perpendicular potential drop. The equipotential surfaces are almost *parallel* to what would be the expected current direction in the absence of current jetting. Consequently, the resulting resistivities shown at the bottom of panel b) are lower than in a). Here, the signals of two pairs (U1 and 4) get negative.

Some lessons can be learned:

- Current contacts, which cover the best part of the side surface of the samples will still generate a largely inhomogeneous current distribution.
- The main potential drop can be perpendicular to the main sample axis, rather than parallel as in a usual resistivity measurement.
- Therefore, slight misalignements of the voltage contacts in the direction perpendicular to the main sample axis can cause the signal to change sign.
- Despite all of this, qualitatively, features of the actual longitudinal resistivity such as the hump at lowest fields are present in almost all presented contact geometries.

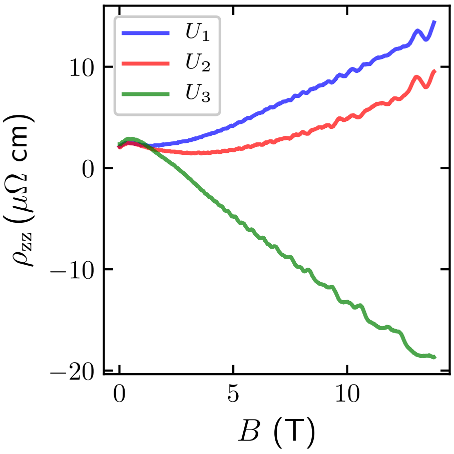

Figure 3.2.4. – Results of the measurement on NbAs with current along a. Sample size and contact geometry in the simulation shown in figure 3.2.3 were the same as in this measurement.

This illustrates the challenges in determining longitudinal resistivities in high magnetic fields in materials with a strong conductivity anisotropy $\sigma_{zz} \gg \sigma_{xx}$ such as high mobility semimetals. On the other hand it also shows that general conclusions regarding e.g. whether the longitudinal magnetoresistance is monotonous or not can still be drawn with some caution.

3.2.3. Silver epoxy voltage contacts

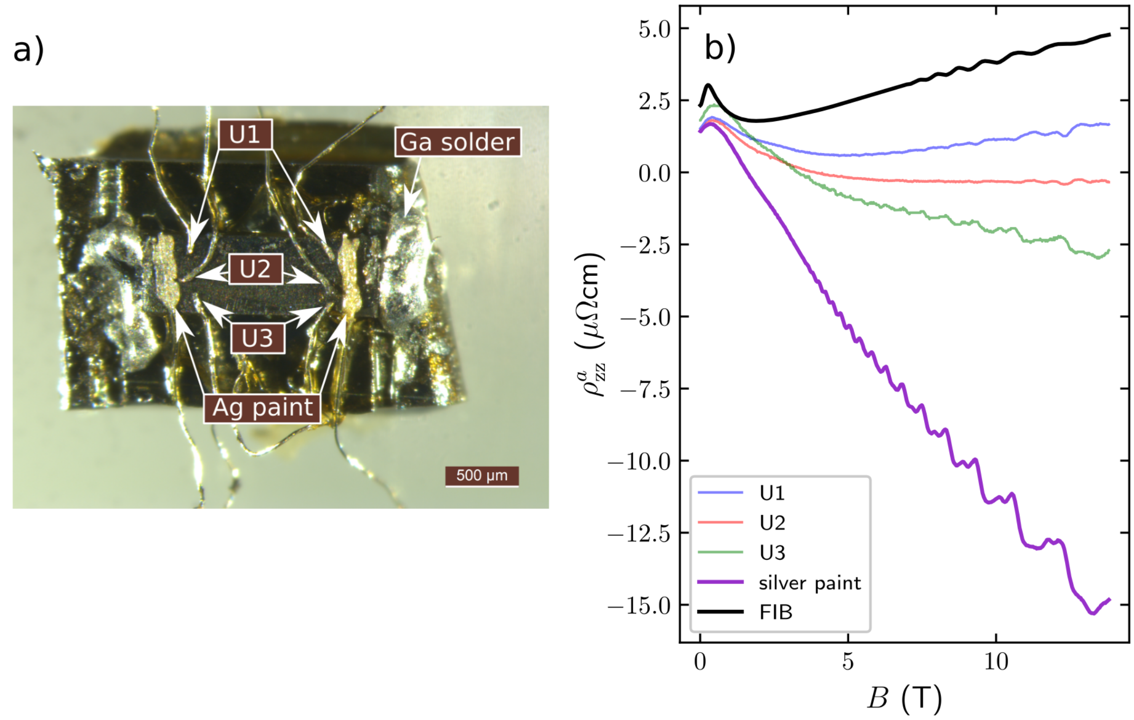

Figure 3.2.5. – a) Photography of a sample with silver paint and spotwelded voltage contacts. Note the gallium does not cover the full crosssection since the leads reaching into it have been retracted, thus moving it. b) Resulting 'resistivities' of the longitudinal magnetoresistance in this sample. Clearly, the silver paint contacts are arbitrarily off. In black, the intrinsic longitudinal magnetoresistance as determined on a microstructured sample (FIB) is shown for comparison.

There are reports which claim that silver epoxy voltage contacts, which cover the width of the sample will avoid current jetting artefacts. The idea is, that by covering the width of the sample some averaging is done which compensates the current inhomogeneities.

In order to test this approach, a sufficiently big sample of NbAs was chosen to try out this method of contacting while monitoring the current distribution with another set of the spotwelded voltage contacts. A picture of the sample can be found in figure 3.2.5 a), the measured 'resistivities' of this experiment in subfigure b).

The strong deviation between individual contacts immediately suggest the presence of strong current inhomogeneities in this sample. Still, while the spotwelded voltage contacts agree in a positive 'resistivity', the silver paint contact agrees with neither of these, turning negative at rather low fields.

This renders voltage contacts made in this particular way inappropriate for the determination of the longitudinal magnetoresistance in these materials, which is not surprising: It was already demonstrated that current contacts, covering the whole side surface of the sample do not improve the current homogeneity substantially [57]. A probable cause is the spatial inhomogeneity of the contact resistance of the contact layer between epoxy and sample. In case of current contacts this leads to an inhomogeneous current injection, in case of voltage contacts to a rather arbitrary pickup of the potential distribution. Since the whole width of the sample is covered, it is not unlikely that well-contacted areas in both contacts have some transverse offset. As shown in the previous subsection, this can cause the potential difference to turn negative.

3.3. Sample preparation

Samples were grown by a vapour transport method as described e.g. in reference [12] by Vicky Süß and Marcus Schmidt at MPI CPfS. Resulting single crystals were cut on a wire or dicing saw and polished on grit 1000 and 4000 SiC paper into shape. Sample alignment was mostly done on a Laue machine or by eye with reference to the facets of the as grown crystals. Voltage contacts were spotwelded unless noted otherwise using 25 µm platinum wire.

The mounting on sample holders for cutting and grinding was done with polyvinyl acetate. This solid polymer can be melted at about 200 °C and the sample embedded in it. After finishing the cutting or grinding process, it can be easily dissolved in acetone.

With the challenges regarding a homogeneous current distribution in field as described in section 3.2, special care was taken in making the current contacts. Mostly, it was attempted to inject the current as homogeneous as possible. For this, current contacts were soldered. A first evolution of this process was employed on TaP where samples of large size were readily available. Here, PbSn solder and a flux[3] from a commercial soldering kit was successfully employed. The flux was used later on whenever contacts got soldered. Another solder used was 'Solder 121', which contains 96.5 % Sn, 3.5 % Ag. The challenge during the whole procedure was to wet the surface of the sample. While this worked rather well on TaP, the other Weyl semimetals were more difficult to wet with any solder.

---

[3] 'The Indium Coorporation of America', flux 'Indalloy #3'.

Usually, voltage contacts were spotwelded first. Then the end surfaces of the sample were cleaned with acetone, allowed to dry, some flux was applied and one to three attempts to solder the current contact onto it were undertaken. If this was not successful, the sample was covered in the residue of the flux and had to be cleaned in an ultrasonic bath in acetone and occasionally an abrasive (SiC 800 grit) as well. After this, voltage contacts which had come off had to be spotwelded on again and the procedure repeated.

Trying to improve this, an attempt with gallium was made. This was motivated by the low melting point of about 30 °C[4] and the hope that it would wet the surface well without issues regarding oxidation at high temperatures. The usage of flux did not improve the wetting process, therefore it was omitted. First attempts were done by encapsulating the mounted sample in polyvinyl acetate and cut into it perpendicular to the current direction in order to get a fresh, clean surface. The trench resulting from the cut would then be filled with Ga, while the polyvinyl acetate would avoid any spillage over the sample. This did not work, since the surface tension of the Ga made it difficult to get it into the trench in the first place. In order to overcome the surface tension of the material, it was still needed to use a soldering iron at about 400 °C. This was used later on samples which were not encapsulated in polyvinyl acetate due to its melting point of about 200 °C. It was also important to avoid any contact of the Ga with the Pt voltage contacts in the process. Here, the wires snapped at the position where the gallium touched them. This is probably due to some alloying process, similar to the amalgam formation in mercury. Since gallium can also be supercooled by quite a margin[5], the PPMS platform with the sample had to be put above a liquid nitrogen bath in order to solidify it before inserting it into the cryostat, in order to avoid any influence of the solidification process on the measurement. Mostly, this method was used on TaAs were 'traditional' soldering proved to be the most cumbersome. However, there was no appreciable difference in the current homogeneity over standard solder.

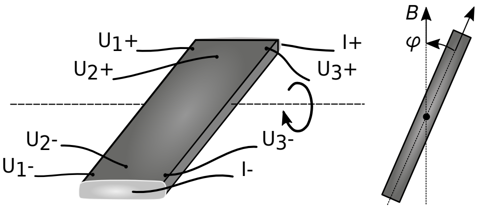

Figure 3.3.1. – Schematic illustration of the measurement geometry for the angle-dependent resistivity measurements presented in this section.

---

[4] https://www.webelements.com/gallium/

[5] It was observed, that gallium on a microscope slide on which some humidity had already frozen was still liquid.

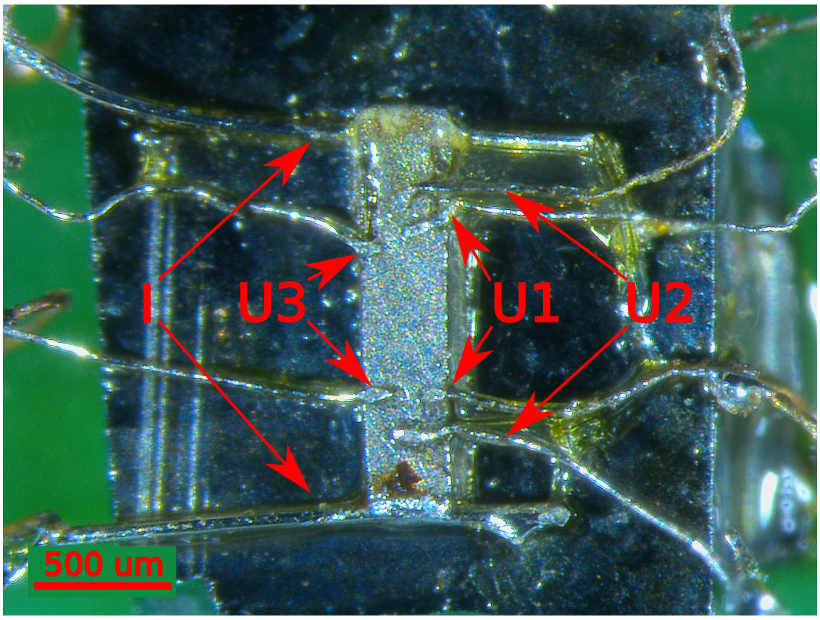

Figure 3.3.2. – Typical picture of a sample contacted for a measurement of the longitudinal magnetoresistance, here TaP with current along *c*. Three pairs of voltage contacts can be seen on the top surface of the sample. The soldered current contacts are at the top and bottom.

Later on, it was also attempted to gold plate the end surfaces with a sputtering process before soldering[6]. Here, a Cr buffer layer was used before sputtering gold onto it. However, already upon application of moderate heat with a soldering iron the layer came off immediately, even at the lowest possible temperatures for lead solder (220 °C).

Another way of sample preparation is microstructuring using a focused ion beam (FIB)[7] [58]. This method allows for larger aspect ratios then bulk samples and a more homogeneous current injection then soldered contacts. These measurements had to be complemented by those on bulk samples and were not applied to all materials, since the method comes with drawbacks such as an unknown contribution to the transport from to a degraded surface layer and the possible degradation of the material due to the large heat input during the processing.

During the actual measurements, an in-situ rotation stage was used in order to get a good alignment between the main sample axis (and therefore, the current) and the external magnetic field. The used geometry can be found in figure 3.3.1, an illustrative picture of a sample in figure 3.3.2.

---

[6] I am indept to Sebastian Seifert for trying this.

[7] The samples were prepared by Maja Bachmann.

3.4. Magnetisation

Magnetisation measurements were done in a Quantum Design SQUID vibrating sample magnetometer. This allowed measurements down to 2 K and up to 7 T. The samples are glued to a quartz glas holder using GE varnish, which is screwed on a probe whose vertical position can be controlled by the device. It is periodically moved at about 14 Hz, moving the sample through a superconducting pick-up coil assembly forming a gradiometer of second kind. Details of the SQUID circuit can be seen in figure 3.4.1. The signal from the gradiometer is amplified by a flux-transformer before it is coupled inductively into the SQUID for further amplification.

The resistance R of the SQUID varies periodically with the fluxed Φ coupled into it. A flux, at which $\mathrm{d}R/\mathrm{d}\Phi$ is maximal is also referred to as the working point, to which the device is biased by the attached compensation circuit. The compensation is used to keep it at the working point independent on the flux coupled into it by the signal. This mode, where the SQUID only serves as a null-detector, is referred to as a flux-locked loop. In the circuit which feeds current into the inductance used for compensation, a so called feedback resistor is used to generate a voltage proportional to the compensating flux and therefore also proportional to the input signal. The choice of this resistor defines the amplification of the SQUID [59, 60].

Since the sample is moved twice into and out of the gradiometer in every cycle of the drive, the *second* harmonic of the signal is proportional to the magnetisation. Consequently, a lock-in process on the second harmonic is performed by the digital signal processor [59]. Both, the low-noise amplification by the SQUID and the lock-in process on the second harmonic enable an extraordinary resolution of $1 \cdot 10^{-7}$ emu according to the specifications of the instrument.

In reality, however, the resolution was one order of magnitude worse, on some days even more for no obvious reasons, which impeded measurements. Still, the rapid measurement capability of the device and the, if working properly, good resolution proved a powerful tool in the investigation of semimetals in general.

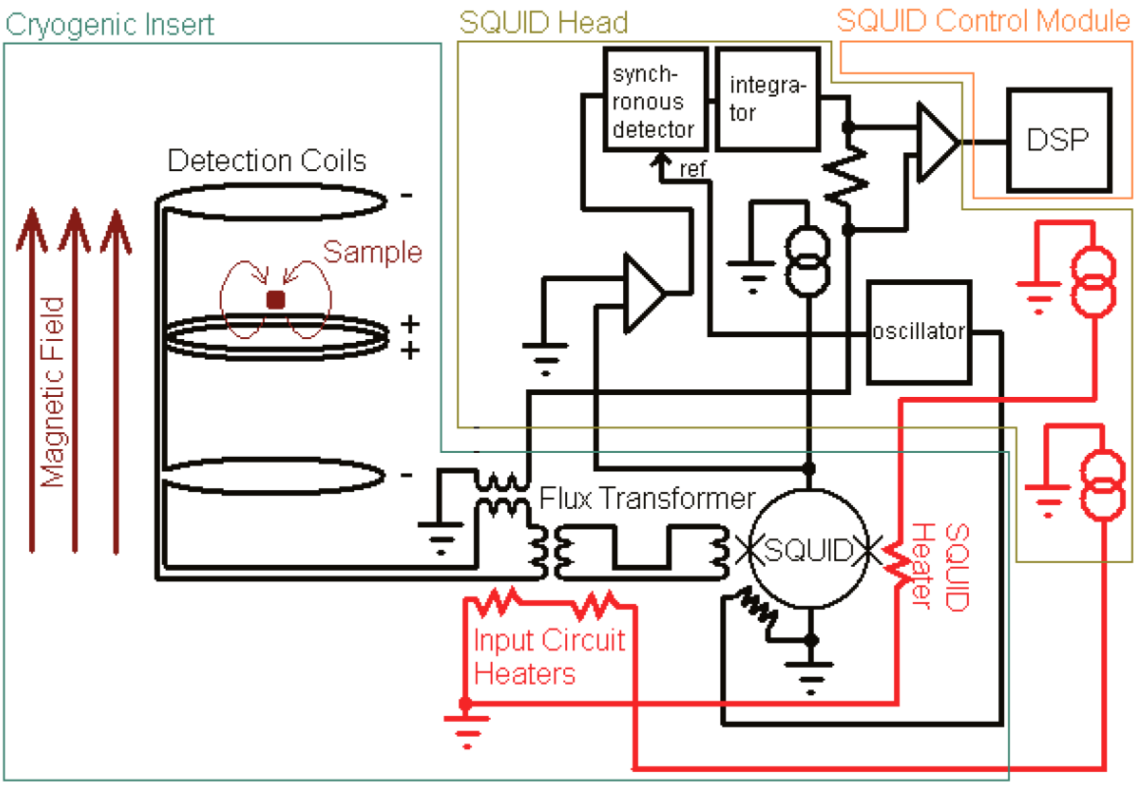

Figure 3.4.1. – Schematic diagram of the Quantum Design SQUID VSM. Figure taken form [59].

4 Weyl semimetals - longitudinal magnetoresistance

4.1. Introduction

4.1.1. Weyl semimetals

Before experimental results on the longitudinal magnetoresistance in the TaAs-family will be presented in chapter 4.2, the material family and current state of research shall be introduced.

Despite the Weyl semimetals being a rather recent topic in experimental physics, the actually studied object, Weyl fermions, were described 90 years back in 1929 theoretically [61].

They are the solution to the massless, three-dimensional Dirac equation [27]

$$\mathrm{i}\partial_t\psi_\pm = H_\pm\psi_\pm, \tag{4.1.1}$$

$$H_\pm = \mp\mathbf{p}\cdot\sigma. \tag{4.1.2}$$

Here, ψ denotes a two component spinor, $\mathbf{p}$ the momentum and σ the vector of Pauli matrices. The dispersion will be linear in 3D, consisting of two bands denoted by the ± which are degenerate at $E = 0$.

The eigenstates have a number of interesting properties: There is a close relation between spin and momentum. The state with $\mathbf{k}$ will have a spin orientation $\uparrow$ and vice versa [27]. This spin and momentum lock is called 'chirality'. If spin and momentum are parallel, that particle has a chirality of 1, if they are antiparallel the chirality is -1. An arbitrary orientation between the two, as in most condensed matter systems, will give rise to an ill-defined chirality. One consequence of the chiral fermions is the reduction of back scattering: Since back scattering would require a well defined change in spin depending on the change in momentum, this is very unlikely. Another consequence is the chiral anomaly described in section 2.7 and [27]. The Weyl points also serve as sources and sinks of the Berry curvature. In any 3D material, the integral of the Berry curvature over any 2D manifold (e.g. a Fermi surface) can only take integer multiples n of 2π, with n being the Chern number. If a Fermi surface encloses a single Weyl point, the Chern number can be either +1 or -1. Since the Chern number of the

Table 4.1.1. – Room temperature lattice constants of the four members of the TaAs family.

	TaAs[38]	NbAs[64]	TaP[12]	NbP[25]
a	3.48 Å	3.45 Å	3.33 Å	3.34 Å
c	11.80 Å	11.17 Å	11.33 Å	11.38 Å

total Brillouin zone has to vanish, Weyl points have to come in pairs, as source and sink [27].

While the model described above can be deduced canonically, its experimental realisation has been sought after for almost a century. In a condensed matter system, linear band crossings in general can be realised by a band inversion. If spin-orbit coupling is strong, this might open a gap throughout the Brillouin zone. In this case, linear metallic surface states will be the result and a topological insulator is created [62]. If the gap is opened throughout the Brillouin zone except for singular points, the material is a Weyl or Dirac semimetal. The latter can be thought of as a realisation of two Weyl semimetals superimposed on each other so a band degeneracy of the states with $|\mathbf{k}\uparrow\rangle$ and $|\mathbf{k}\downarrow\rangle$ is present [62]. This is also a consequence of Kramers theorem, stating that in a system with preserved time-reversal and inversion symmetry every band has to be doubly degenerate. If time-reversal or inversion symmetry is broken, the Dirac cone will split into two Weyl points of opposite chirality [62]. While there can be just one pair of Weyl points in a system with broken time-reversal symmetry if the crystal symmetry allows for it, a breaking of inversion symmetry results in at least two pairs: Since the intact time reversal symmetry transforms a Weyl point at $\mathbf{k}$ to one at $-\mathbf{k}$ but keeps the chirality unchanged, the corresponding partners of opposite chirality have to be present to keep the total Chern number at zero [27].

In a real material, the Weyl points have to be near the Fermi level to have any influence on the electronic properties. One example, where this is the case and where a broken inversion symmetry leads to the existence of Weyl points is the TaAs material family [63].

4.1.2. The TaAs-family of Weyl semimetals

The non-centrosymmetric, tetragonal TaAs family belongs to the symmetry group $I4_1md$ and consists of the four materials TaAs, TaP, NbAs and NbP [63]. Their room temperature lattice parameters are presented in table 4.1.1. In 2015 they were found to host Weyl points close to the Fermi surface by computational methods [63]. At the

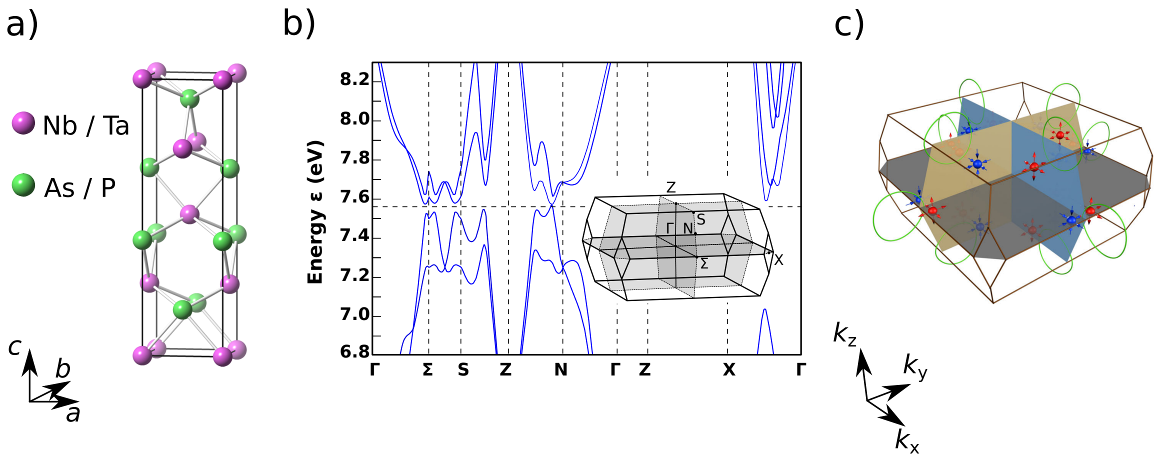

Figure 4.1.1. – Panel a): shows the chemical structure of the TaAs-family of transitionmetal monopnictides. Figure reproduced from [66]. Panel b): The bandstructure of TaAs close to the Fermi energy is shown together with the Brillouin zone and the high symmetry points. The Figure is based on the bandstructure published in [13]. Panel c): The Brillouin zone depicted together with the position of the pairs of Weyl points and nodal rings. Reproduced from [63].

same time, a first article on the experimental observation of Weyl fermions by angle-resolved photoemission spectroscopy in TaAs appeared [65]. The crystal structure can be seen in figure 4.1.1 a). If spin-orbit coupling is not included, the electronic structure is found to host so called nodel-rings, ring shaped band degeneracy's in the $k_\mathrm{x} - k_\mathrm{z}$ and $k_\mathrm{y} - k_\mathrm{z}$ planes, shown in green in figure 4.1.1 c). Upon including spin-orbit coupling, the degeneracy is lifted apart from singular points, the Weyl points, which are slightly offset from the described crystal planes. The nodal rings are shown together with the Weyl points in figure 4.1.1 c).

All four materials are compensated semimetals according to DFT calculations, which is in accordance with experimental results in both niobium compounds [14, 67]. Experimentally, a slight electron doping is found in both TaP and TaAs [12, 13]. Measurements of the typical observables agree with that: The magnetisation shows a diamagnetic response, superimposed by quantum oscillations which are extremely strong in some cases (see e.g. figure 4.2.7 and [12, 13]). The temperature dependence of the resistivity shows metallic behaviour (see figure 4.2.1). Upon application of a magnetic field, ρ_xx rises sharply due to the compensation and high mobility of the charge carriers [12, 13, 67, 25]. The Hall component, ρ_xy shows non-linearities which can be explained by a two-band model which is in agreement with the existence of more than one band crossing the Fermi energy (see later). Both ρ_{xx} and ρ_{xy} are typically superimposed by Shubnikov-de-Haas oscillations to a varying degree.

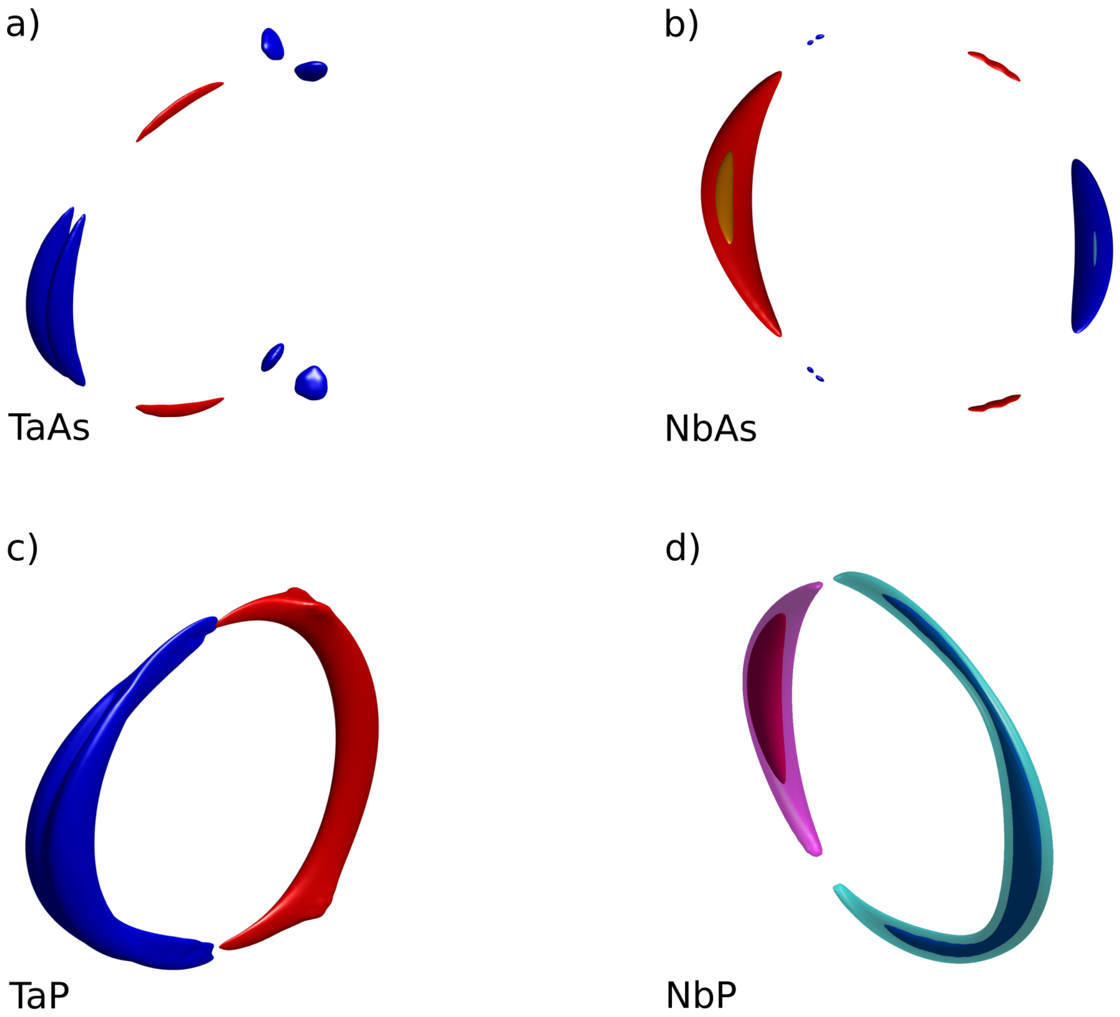

Figure 4.1.3. – Fermi surfaces of TaAs, NbAs, TaP and NbP. Blue denotes electron-like, red hole-like surfaces. Figures reproduced from the Bandstructures published in [13, 15, 12, 14].

Regarding the electronic structure, the lack of inversion symmetry leads to a spin-splitting of both the valence and the conduction bands due to spin-orbit coupling and the lack of inversion symmetry. In figure 4.1.1 b) the bandstructure of TaAs close to the Fermi energy is shown and the spin splitting of both the valence of conduction band is well visible. Two bands can be seen to touch at the Fermi energy close to N. Here, the valence band briefly crosses the Fermi energy, giving rise to the hole Fermi surface (red) depicted in figure 4.1.3 a). Around Σ and S, the conduction bands come close to the Fermi energy without crossing it. The actual crossing cannot be seen here, since the cuts through the band structure are along high symmetry directions and the Weyl points are slightly off those (see figure 4.1.2).

Since tantalum is considerably heavier than niobium, spin-orbit coupling is stronger. This leads to a larger spin-splitting in both tantalum compounds, pushing the energetically higher (lower) conduction (valence) band away from the band edge and Fermi energy. As a consequence, only two bands cross the Fermi energy giving rise to only two Fermi surfaces, one electron and one hole surface. In both niobium compounds, a second smaller spin-split Fermi surface is typically nested within a larger one (see figure 4.1.3 b) and d)).

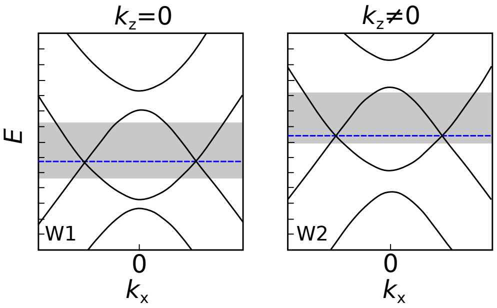

Figure 4.1.2. – Schematic illustration of the bandstructure around the two distinct pairs of Weyl points.

In figure 4.1.2, the bandstructure around the two Weyl points is shown schematically as a cut along k_x, which is the connecting direction of the Weyl points. Both spin-split valence and conductance bands are shown, as well as the offset in energy between W1 and W2. The Fermi energy ranges within which two separate Fermi surfaces around each Weyl point are present, are illustrated in grey. This energy range does not coincide with the band edges: Since what is shown is a cut along e.g. k_x, the dispersion along k_y makes a merger of the surface at different k_y possible. The particular placement of the Fermi energy in the individual compounds now determines the number and kind of Fermi surfaces:

- Separate and therefore chiral, Fermi surfaces around each Weyl point if E_F is in the grey area.
- The merger of the two surfaces if the Fermi energy is between the grey area and the next band edge.
- The existence of an additional Fermi surface from the spin-split band once the Fermi energy is above or below the next band edge.

The existence of individual Fermi surfaces around each Weyl point is of crucial importance. The 'simplest' models such as Son *et al.* [28] are based on individual Weyl Fermi surface pockets. More elaborate models such as Johansson *et al.* (see chapter 2.7.1) find a vanishing contribution of the chiral anomaly at Fermi energies which are below the saddle-point energy at which both pockets merge. On the other hand, there is still a finite contribution above this energy, although heavily suppressed. The actual size of the suppression depends on details of the band structure and its computation including all relevant details has not been performed yet for the real systems presented here. Therefore, the classification into those materials where chiral contributions are expected ('chiral') and those where they are absent ('non-chiral') is done purley on the presence of individual Fermi surfaces around each Weyl point.

The Fermi surfaces of all four materials are presented in figure 4.1.3.

In TaAs, both Weyl points are found in individual electron-like Fermi surfaces [13]. Additionally, the hole band crosses the Fermi energy such that two banana shaped trivial surfaces appear in between the chiral ones enclosing both pairs of Weyl points. Therefore, this compound is chiral.

In TaP the nodal ring separates into two big banana shaped Fermi surfaces, enclosing either both W1 (electron surface) or both W2 (hole surface) Weyl points. On the hole surface, the W2 points give rise to the 'horns' at the ends of the 'banana'. Since both pairs of points are enclosed in one Fermi surface, this compound is non-chiral.

NbAs hosts four Fermi surfaces. Within the bigger electron surface, both W1 Weyl points are enclosed. Nested within it, is its spin-split equivalent. Both W2 Weyl points are enclosed in an individual Fermi surface pocket from the same electron band as the bigger pocket. On the opposite side of the nodal ring, two banana shaped hole pockets from the spin split bands are situated, again nested within each other. Due to the tine separate W2 Weyl pockets, NbAs is also chiral.

NbP also hosts four Fermi surfaces, two electron surfaces nested within each other and two hole surfaces. The electron surfaces are almost C-shaped, spanning about 2/3 of the nodal ring. Since all Weyl point pairs are merged, the compound is non-chiral.

In summary, while both arsenides are chiral compounds, both phosphides are 'trivial' semimetals, but with spin-polarised Fermi surfaces.

4.1.3. Previous experimental reports of the chiral anomaly

After the discovery of Weyl points in the band structure of the TaAs-family, the negative longitudinal magnetoresistance in TaAs as a signature of the chiral anomaly was quickly discovered [38]. In this publication, the authors report sample growth, DFT calculations and transport measurements, together with a rather rough analysis of the quantum oscillations observed in transport. Since the existence of current jetting in these materials had not been reported yet, it was not taken into account, also lacking notes regarding contact preparation. Their resistivity for $I||B$ shows a pronounced increase in field, followed by a decrease and another high field increase, giving rise to a peak at 1 T and a broad dip around 5 T (see figure 4.1.4 a)). The angle-dependent

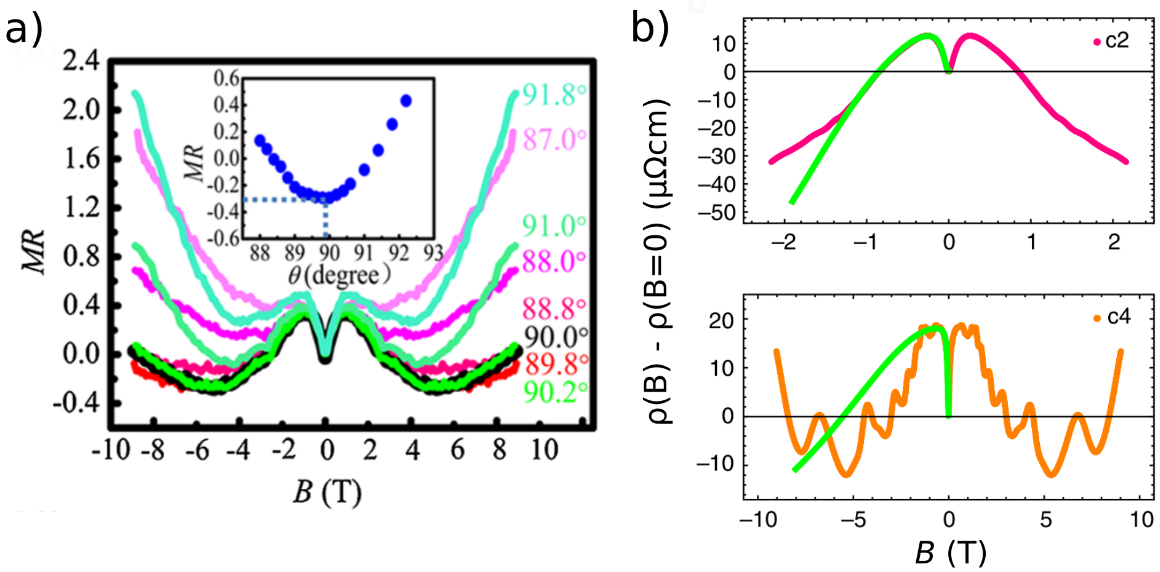

Figure 4.1.4. – Literature reports on the chiral anomaly in TaAs. a) First report on the observation of the chiral anomaly, figure taken from [38]. b) Supposed chiral anomaly in two samples with current along c. The Fermi energy in sample c2 is reported to be closer to the Weyl points than in sample c4. Figure taken from [33], labels were added afterwards.

longitudinal magnetoresistance data presents a rather smooth variation of the resistivity with angle at fixed magnetic field (see insert of figure 4.1.4 a)). This shows to be almost symmetric around the parallel orientation with a negative longitudinal magnetoresistance of around 30 %. The authors interpret the negative longitudinal magnetoresistance as a chiral anomaly, with the low-field increase of resistivity as a weak antilocalisation which they approximate as $\sqrt{B}$. It should be noted, the last approximation is only strictly true for a large separation of the dephasing length and the mean free path (see chapter 2.7 and [17]).

Another report on TaAs also presents the dependence of the negative longitudinal magnetoresistance on the position of the Fermi energy with respect to the Weyl nodes, μ [33]. Their work also includes results on samples with current along the crystallographic a and c axis (see figure 4.1.4 b)). As described in chapter 2.7, an angular dependence of the size of the chiral anomaly with respect to the angle between the current and the Weyl node separation is expected: Depending on the model it should be either suppressed or enlarged if the current is applied along the c direction rather then a (see chapter 2.7.2 and [35, 32]). Still, the size of the negative longitudinal magnetoresistance in their report depends on μ alone (for the data with current along c, see figure 4.1.4 b), or the original publication). Also, the fit shown in figure 4.1.4

b), bottom, is rather far off. At the same time the fit parameter describing the size of the chiral anomaly contribution agrees perfectly with their model (see [33]).

Besides the physical questions raised in reference [33], there are also experimental ones: While they do acknowledge the possibility of current jetting effects, they do not proof their absence. To avoid them, they use silver paint for current and voltage contacts likewise, both covering the width of the sample. As shown, silver paint voltage contacts, made in a similar manner, were found to yield results which are completely arbitrary, by no means yielding an average of the potential distribution in the sample as claimed (see chapter 3.2.3, figure 3.2.5).

It would also be of interest to know, how the group of authors managed to grow samples with various doping levels in the first place. Reports on TaAs so far agree in their quantum oscillation frequencies, all reporting a dominant frequency of 7 T with striking reproducibility [38, 13, 16]. We found that from almost a dozen batches, only a single batch did yield a slightly different doping level, indicated by the main quantum oscillation frequency of 10 T.

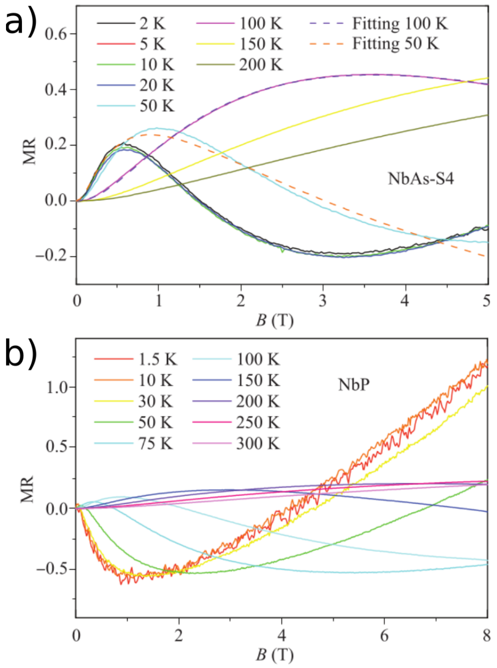

Figure 4.1.5. – Literature reports on a) NbAs and b) NbP. Figure taken from [39].

There are also reports about a negative longitudinal magnetoresistance interpreted as chiral anomaly in both niobium compounds [68, 39]: Both materials exhibit a negative longitudinal magnetoresistance for $B||I$ in the literature as well as in our results. In NbAs, an initial increase in resistivity, which is interpreted as weak antilocalisation, is followed by a decrease and another increase, similar to TaAs (see figure 4.1.5, [68]). NbP shows the same behaviour, apart from the initial increase [39]. The authors interpret the results as an interplay between a weak antilocalisation and a chiral anomaly, which somehow becomes a localisation at higher temperatures. It remains unclear how it is possible, that the negative longitudinal magnetoresistance is entirely caused by the chiral anomaly at low-temperatures, while the decreasing phase coherence time turns *on* the localisation at higher temperatures. A more detailed description of weak localisation effects can be found in chapter 2.6, but it should be mentioned that a decreasing phase coherence time will switch off all weak-localisation effects.

4.2. Results

4.2.1. Transport: temperature dependence

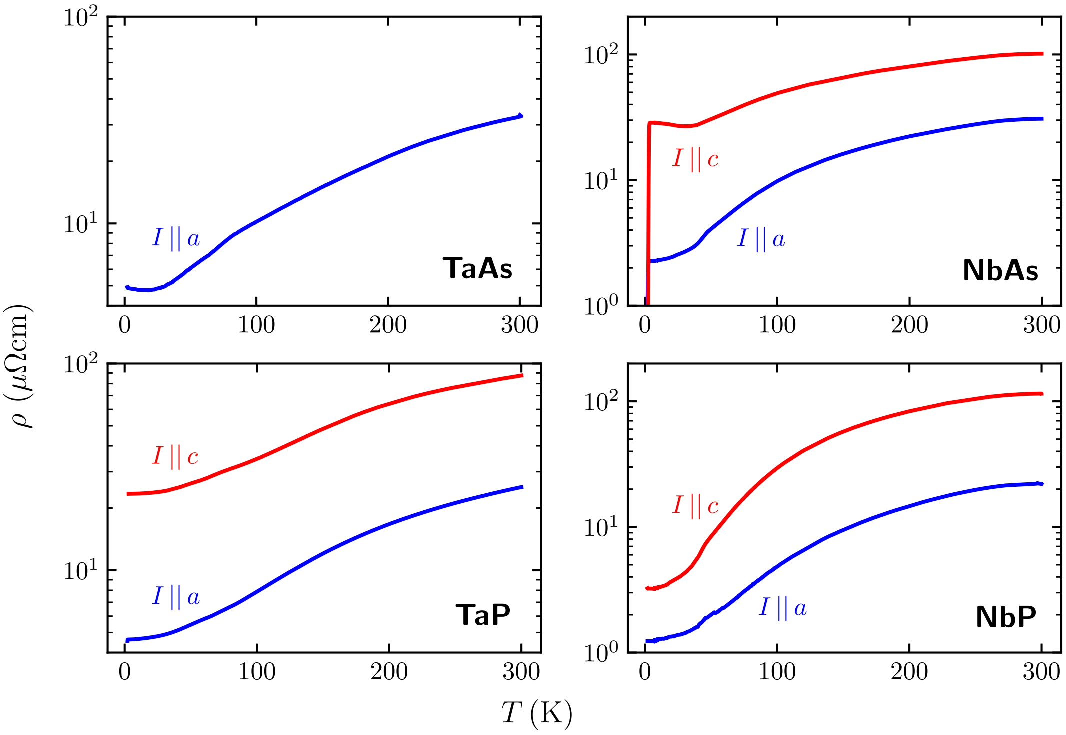

Figure 4.2.1. – The temperature dependent resistivity as determined during the warmup (TaP, TaAs) and cooldown (NbP, NbAs). Since this was originally only meant to be for diagnostic purpose the thermalisation is not ideal, as the difference in shape between warmup and cooldown indicates. The transport along a is shown in blue, transport along c in red. Since the NbAs samples were microstructured, a superconducting transition of the surface layer around 3 K is visible.

In order to aid the understanding of the magnetotransport results, the temperature dependent zero-field resisitvity $\rho(T)$ was determined and is shown in figure 4.2.1. All materials show metallic $\rho(T)$ behaviour. Both TaAs and NbAs with current along c show a slight increase in resistivity at lowest temperatures, indicative of some impurities influencing the resistivity as will be discussed later in section 4.2.4.

Both samples of NbAs ($I||a$ and $I||c$) were cut from the same crystal by a microstructuring process. This implies, the increase in resistivity at low temperature for current along c must be related to the crystallographic orientation of the current and does not have its origin in any sample dependence. At lowest temperatures, a superconducting transition can be seen in both NbAs microstructures. The focused ion beam process selectively sputters more As then Nb, leaving a niobium rich surface layer behind which turns superconducting [58]. This is therefore not related to intrinsic properties of the material.

Comparing the resistivities from various voltage contacts (not shown) indicates a slight rearrangement of the current within the sample during the cooldown, as indicated by minor differences in the $\rho(T)$ curves.

The residual resistivities are higher than what has been reported in the literature: In e.g. NbP reported values are as low as $0.63\,\mu\Omega\,\mathrm{cm}$ [25], while our sample shows about twice that residual resistivity. The other compounds show a similar trend. This implies a higher defect concentration in the samples investigated over those reported in the literature.

The resistivity anisotropies between current along a and c are typically below 10, indicating the materials to be threedimensional, although anisotropic. This is discussed in more detail in section 4.2.3.

4.2.2. Transport: field dependence

The technical details of the angle-dependent measurements on the Weyl semimetals can be found in section 3.3. The result of these measurements were $\rho(B)$ curves at various angles, as determined by the raw rotator angle, which had to be converted to angles with respect to the sample orientation in the magnetic field. Both were closely related, but still slightly offset due to differences in sample mounting in each measurement run and more systematic differences between the actual position of the rotation platform and the readout at the top of the rotator.

This realignment was typically done taking two things into consideration: In one approach, the $\rho(B)$ curves for various angles were inspected and the angle with the highest or lowest resistivity at high fields was chosen as parallel orientation. If current jetting effects were stronger, there was too much ambiguity in this method. The second approach was to look at the $\rho(\theta, B = 14\,\mathrm{T})$ results of the rotation in field. Here, symmetry points were sought (such as the maxima for $B \perp I$ being 180° apart) and the middle between these was taken as the angle with parallel orientation between field and current. Typically, both approaches led to the same raw PPMS rotator angle in most measurement runs with few exceptions. This was taken as an indication for the criteria to be reliable. The few outliers (e.g. TaP, $B||a$) probably stem from offsets during sample mounting. An angular uncertainty of 1° has to be assumed. The angles shown in the following figures are relative to the parallel orientation defined that way.

The field dependent resistivity for some angular window around the parallel orientation is shown in full for a number of reasons. It illustrates the susceptibility of the magnetoresistance to misalignments which can be used to distinguish between various contributions to the resistivity (see chapter 2.1). Also, the variation between voltage contacts over some angles indicates the quality of the current contacts and the general current homogeneity.

In the following, the superscript in the resistivity will denote the crystallographic orientation of the current, e.g. $\rho^{\mathrm{c}}_{\mathrm{zz}}$ denotes the longitudinal resistivity with current along the c axis.

Results for $B \; || \; c$

The results on TaP, NbAs and NbP can be seen in figures 4.2.2 respectively. No measurement on TaAs was performed. TaAs single crystals were mostly long along [100] or [110] and rather thin, making it impossible to yield bulk samples of a somewhat reasonable aspect ratio (>1) with current along c.

The results presented here show an increase in resistivity at lowest fields and a saturation from about 2-4 T onwards. All agree in the existence of a slight dip in the plateau.

While the angular dependence in TaP and NbAs is rather small, it is quite pronounced in NbP. The apparent negative resistances around 1-2° in the contacts U2 and U3 at fields from about 10 T on indicate the presence of current jetting upon some misalignment of the current with respect to the applied magnetic field.

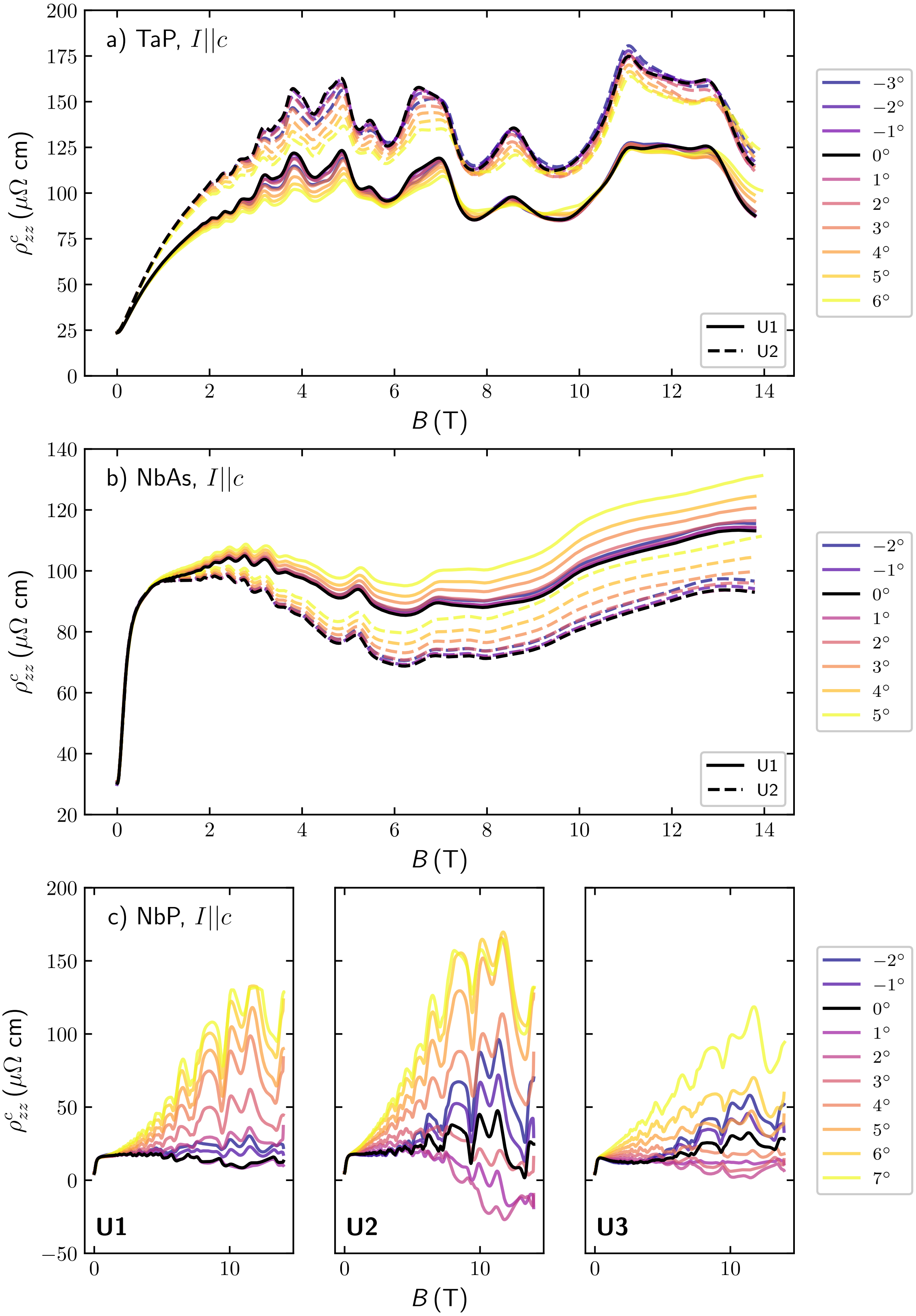

Figure 4.2.2. – The longitudinal magnetoresistance ρ^c_{zz} in a) TaP, b) NbAs and c) NbP .

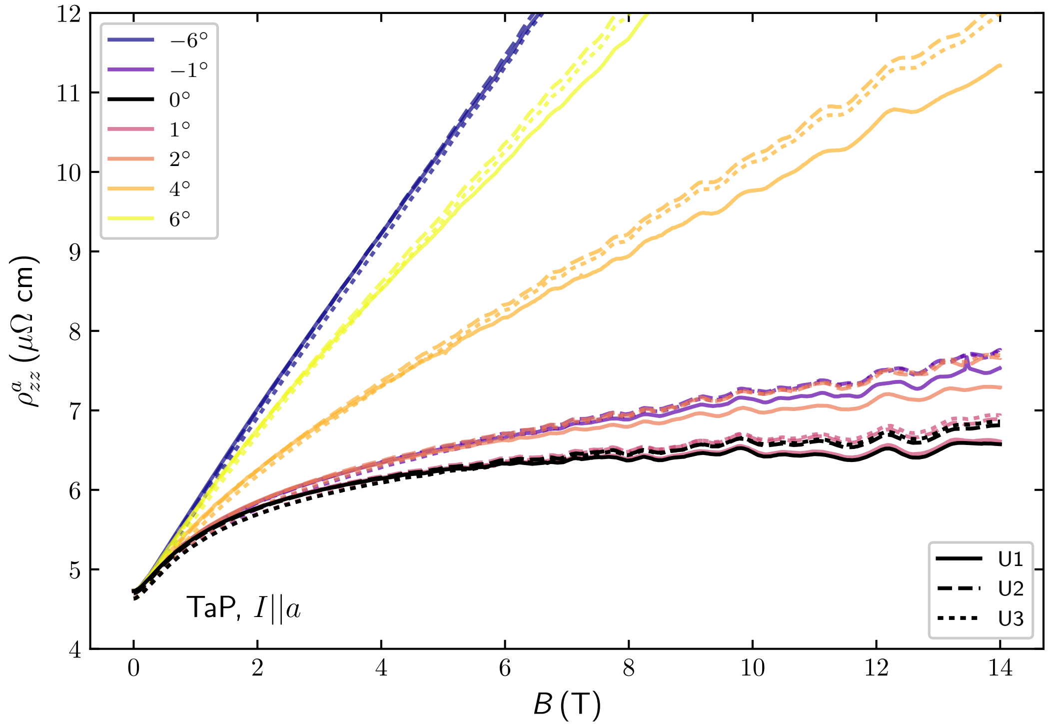

Figure 4.2.3. – The longitudinal magnetoresistance ρ^a_{zz} in TaP. Due to technical problems with the rotation stage the angular sampling frequency is more coarse than in other measurements.

Results for $B \mid\mid a$

The results on TaP (figure 4.2.3) with $B||a$ strongly resemble those with field along c presented earlier. As can be seen, the current homogeneity is rather good, which is partially due to the fact that TaP could more easily be wetted with solder, partially due to the more favourable aspect ratio (2.5 mm length vs. 300 µm width) and partially due to the lower mobility which is in the lower one digit Tesla range (see table 4.2.1). The results could be qualitatively reproduced in a second sample.

The measurements on NbAs with field and current parallel to the crystallographic a axis can be seen in figure 4.2.4. Since the second voltage contact of the FIB structure was broken, only the results of the remaining contact are shown. Despite this, a reasonable current homogeneity can be assumed: A microstructure of very similar size was used for the measurement with current along c and showed no qualitative difference between the two current contacts, with minor quantitative differences (figure 4.2.2 b)). Also, current jetting effects can be expected to play only a minor role if the aspect ratio is higher or of the order of the squareroot of the conductivity anisotropy ratio

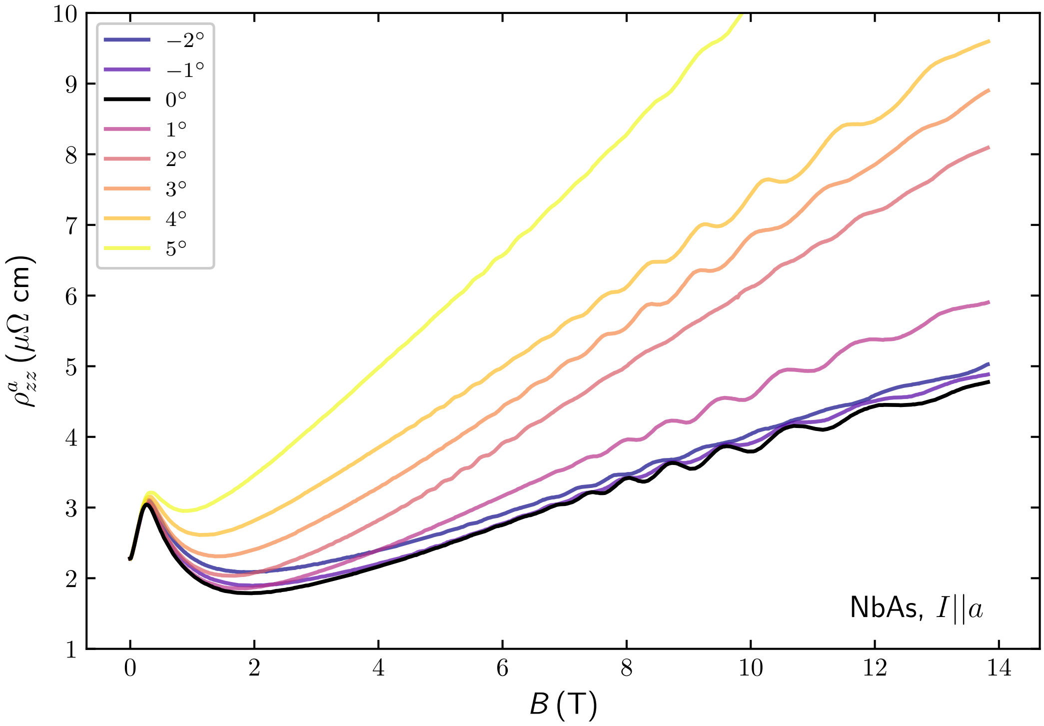

Figure 4.2.4. – The resistivity of NbAs along the crystallographic a direction for small angles between field and current. Since one of the contacts was broken, only the results of the remaining one are shown.

$\sqrt{\sigma_{||}/\sigma_{\perp}}$ [11]. If we estimate this using the longitudinal and transverse resistivities, the later determined in an experiment not shown here, we arrive at 7 or 20 at 0.5 T or 4 T respectively. Since the aspect ratio of the structure is 18, current jetting effects should be absent. Furthermore, measurements by collaborators on e.g. TaAs microstructures in the same field and current orientation in pulsed magnetic fields showed no sign of current jetting as well [16].

At low fields, the resistivity increases quadratically before it decreases again. At higher fields there is a strongly angle dependent increase which has no obvious functional form and is superimposed by quantum oscillations. It is especially noteworthy, that at least the first increase in ρ at low fields (if not the following decrease as well) shows no angle dependence.

Influences of the FIB process can be excluded, since the result was qualitatively reproduced on a bulk sample (not shown).

The data set is less clear in NbP as can be seen in figure 4.2.5. Here, signs of current jetting can be observed: While for negative angles U1 shows positive resistances / voltages, U3 is negative. Upon crossing the parallel orientation, this is inverted. This

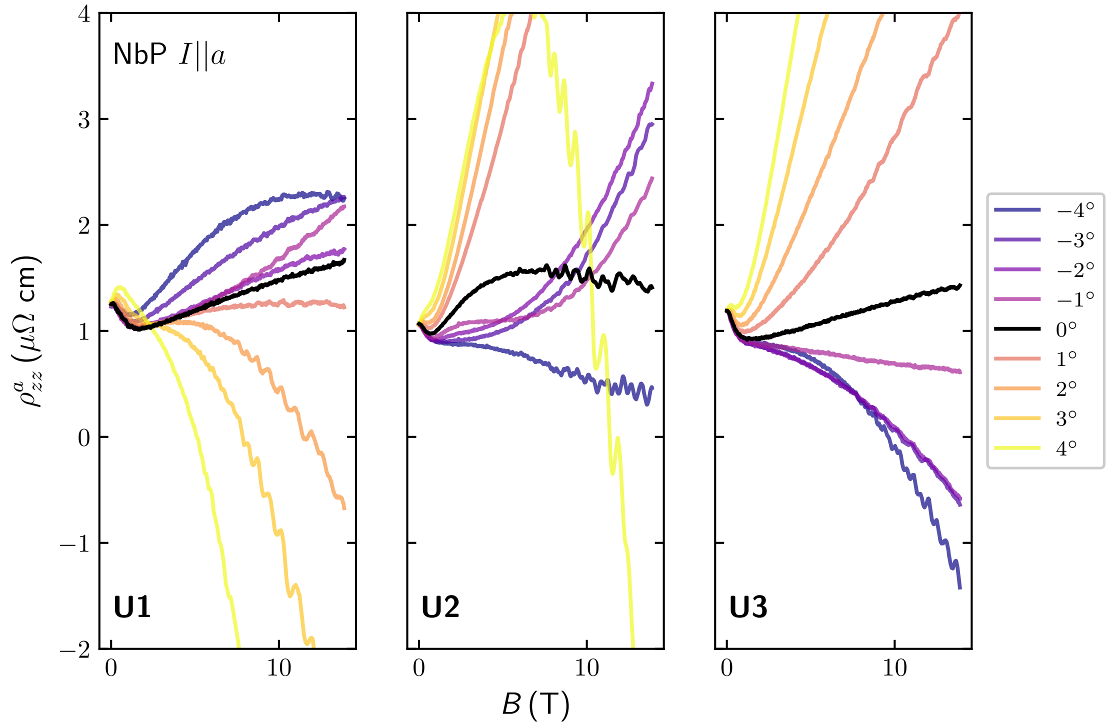

Figure 4.2.5. – The resistivity of NbP along the crystallographic a direction for small angles between field and current.

is indicative of a jet swinging from one pair of voltage contacts to another during the rotation. Still, all contacts agree on the negative longitudinal magnetoresistance at low fields which suggests this to be an intrinsic feature, especially since current jetting effects should be small or almost absent there. In general, the intrinsic LMR seems to be quite small, only of the order of 20 % taking the difference between the 0 T resistivity and the minimum around 1 T as a measure.

Since the results on TaAs are the most ambiguous, data from two measurement runs shall be presented in figure 4.2.6. Both runs used the same crystal which was cut, polished and re-contacted in between. In the first run (figure 4.2.6), the current contacts were made with AgSn solder while in the second, gallium was used.

The difference in zero-field resistivity of 5.5 µΩ cm to 9 µΩ cm is not unexpected for a sample size well below 1 mm and contact distances of 200-400 µm and therefore only represents the measurement uncertainty of the geometry factor.

The initial increase is roughly 3-4 times the zero field resistivity, with the second run on the lower end of the spread. All curves agree in the following decrease, however, at high field strong signs of current jetting take over and apparently dominate the signal. An interesting side note is the apparent symmetry of the curves around the parallel orientation in run 1. The upturn almost overlaps when comparing curves at some angle ϑ vs. $-\vartheta$.

We can now compare these results with the simulation of the signals for imperfect current contacts presented in chapter 3.2.2. Here, it was shown that even in the presence of strong current inhomogeneities at high fields, the low to intermediate field region will still qualitatively show the 'true' intrinsic magnetoresistance. Therefore, the longitudinal magnetoresistance can be assumed to show the hump with the following decrease as well.

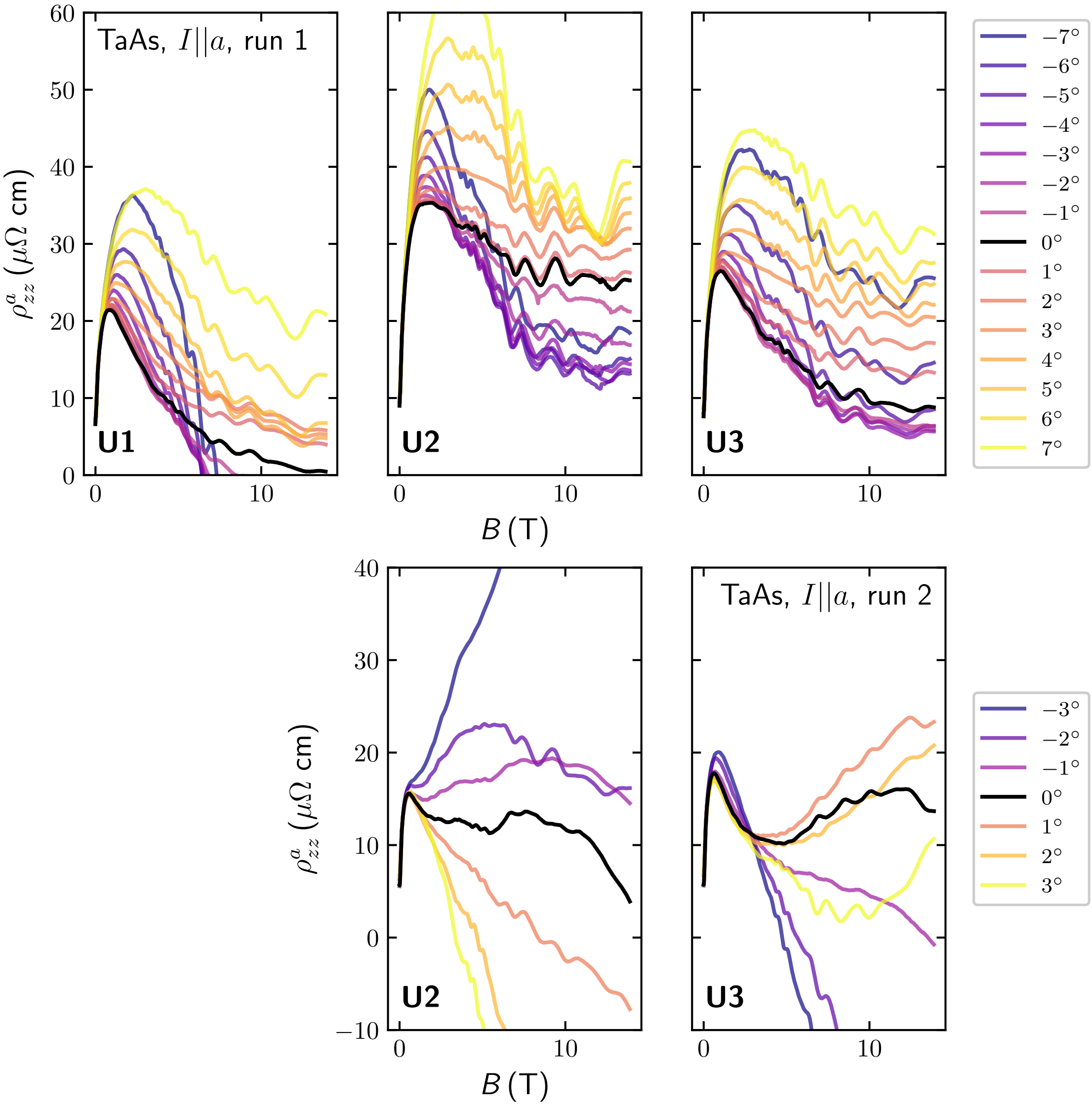

Figure 4.2.6. – The resistivity of TaAs along the crystallographic a direction for small angles between field and current for two measurement runs.

4.2.3. Magnetisation, mass anisotropy and transport parameters

The challenges involved in the analysis of the effective mass detailed in chapter 2.8.2 were only discovered by the author and his group after the publication of the electronic structure of TaP and TaAs in [12, 13]. Therefore, the magnetisation data on all four compounds of the TaAs family was reanalysed in the course of this thesis, taking the effect of a wide FFT window into account. Also, results on zero-field resistivities and mobilities are compiled and presented together with the effective masses in tables 4.2.1 (TaP), 4.2.2 (NbAs), 4.2.3 (NbP) and 4.2.4 (TaAs). This information will be needed in the analysis of the magnetotransport results presented earlier.

Magnetisation of NbP

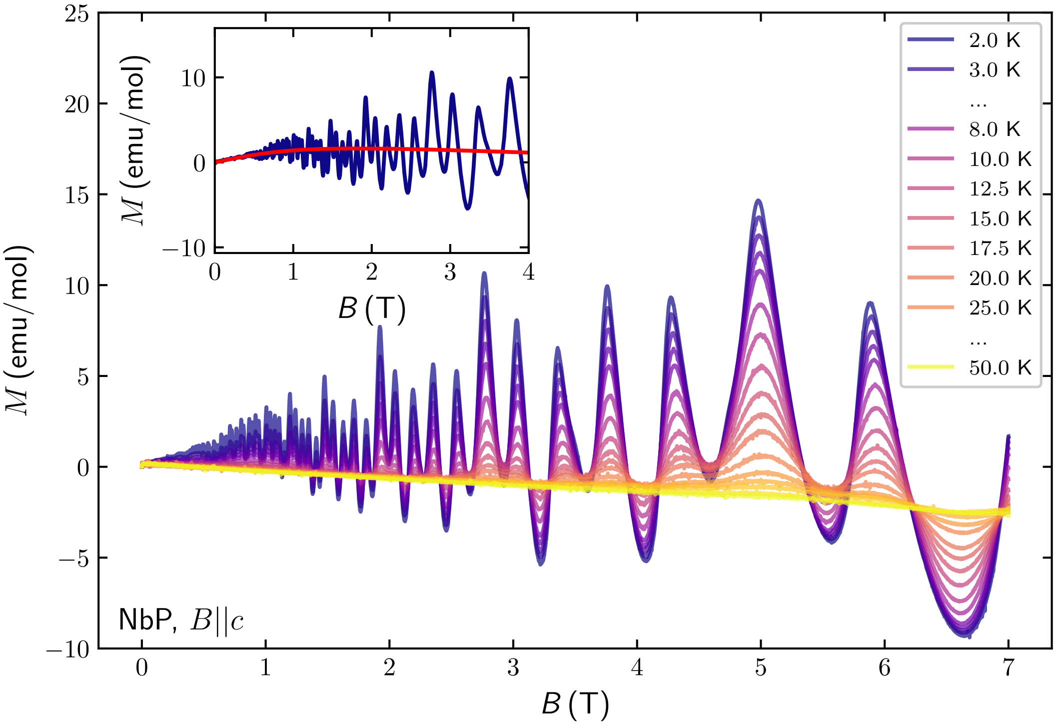

Figure 4.2.7. – Example of the field dependent magnetisation, here of NbP with $B||c$. In this material, the de Haas-van Alphen oscillations were most pronounced. In the insert the magnetisation at 2 K (blue) is shown separately with a Brillouin fit (red) according to Eq. 4.2.1.

In figure 4.2.7, the magnetisation of NbP for field along c is shown as an example. In this material and orientation, the quantum oscillations were most pronounced, giving the actually diamagnetic material even a positive magnetisation at certain fields.

Besides the strong de Haas-van Alphen oscillations, the background shows a superposition of diamagnetism and paramagnetism, the latter from magnetic impurities. Since the paramagnetic background was strongest in this sample, we can use it to estimate an upper boundary of the concentration of magnetic impurities. The magnetisation of these can be modelled by a Brillouin function $B_J(x)$ with a diamagnetic term added to it [69]

$$
\begin{aligned}
M &= M_{\text{para}} + M_{\text{dia}}, && (4.2.1)\\
M_{\text{para}} &= NgJ\mu_{\text{B}}B_J(x),\; x = gJ\mu_{\text{B}}B/k_{\text{B}}T && (4.2.2)\\
B_J(x) &= \frac{2J+1}{2J}\coth\left(\frac{(2J+1)x}{2J}\right) - \frac{1}{2J}\coth\left(\frac{x}{2J}\right), && (4.2.3)\\
M_{\text{dia}} &= \chi B. && (4.2.4)
\end{aligned}
$$

The used notation is: g is the g-factor, μ_{B} is Bohr magneton, k_{B} the Boltzmann constant, J the quantum number of the total angular momentum and χ the diamagnetic susceptibility.

The fit can be seen in the insert of figure 4.2.7. It was performed with a fixed diamagnetic susceptibility of 0.377 emu/mol/T as determined from a linear fit to the magnetisation at 50 K to avoid an influence from the strong quantum oscillations. The resulting total angular momentum J was close to 3 and the resulting impurity concentration N 88 ppm.

Effective mass and transport parameters of TaP

The effective masses from the magnetisation and transport results on TaP are shown in table 4.2.1. Since the oscillations with field along a were hardly resolvable no effective mass or Dingle analysis could be performed here. Along c, both the 15 T and the 18 T frequency were too close to get a reliable estimate of the peak width. As for all results on the effective masses from quantum oscillations presented later, the error bars were estimated from performing the analysis over various field windows and estimating the error from the spread of the results. If this method yields an error smaller 10 %, this will be assumed as error as outlined in chapter 2.8.

The zero field resistivities presented in table 4.2.1 are used to extract the respective mobilities via a Drude model [2]:

$$\sigma = ne\mu_{\text{electron}} + pe\mu_{\text{hole}} \qquad (4.2.5)$$

The charge carrier densities $n = 2.2 \cdot 10^{19}\,\text{cm}^{-3}$ and $p = 1.4 \cdot 10^{19}\,\text{cm}^{-3}$ are taken from [12]. This reduces the equation to two free parameters and therefore requires further

Table 4.2.1. – Transport parameters of TaP: The resistivity anisotropy, mobilities μ_i from magnetoresistance fits and transport scattering times τ_{tr}^{i} for electron (i = e) and hole (i = h) type charge carriers. The effective masses from the dHvA measurement with field along c is presented as well.

transport analysis	$I\|\|a$	$I\|\|c$
$\rho(2\,\mathrm{K})$	4.7-$5.5\,\mu\Omega\,\mathrm{cm}$	$24\,\mu\Omega\,\mathrm{cm}$
$\rho_{\mathrm{c}}/\rho_{\mathrm{a}}$	-	4.4-5
$\mu_{\mathrm{h}}/\mu_{\mathrm{e}}$	4	5.3
μ_{e}	$1.6\,\mathrm{T}^{-1}$	$0.27\,\mathrm{T}^{-1}$
μ_{h}	$6.4\,\mathrm{T}^{-1}$	$1.43\,\mathrm{T}^{-1}$
$\tau_{\mathrm{tr}}^{\mathrm{e}}$	$1.4 \cdot 10^{-12}\,\mathrm{s}$	$6.3 \cdot 10^{-13}\,\mathrm{s}$
$\tau_{\mathrm{tr}}^{\mathrm{h}}$	$1.4 \cdot 10^{-12}\,\mathrm{s}$	$2.7 \cdot 10^{-12}\,\mathrm{s}$
de Haas-van Alphen analysis	$B\|\|c$	
m^*, hole α	0.025 ± 0.003	
m^*, hole β	0.05 ± 0.01	
m^*, electron δ	0.16 ± 0.01	

simplification which is achieved by fixing the ratio of the electron and hole mobility. For a certain orientation i, the ratio $\xi^i = \mu^i_{\mathrm{hole}}/\mu^i_{\mathrm{electron}}$ is computed from mobilities determined by a separate measurement. This might be from the Hall conductivity σ_{xy} analysed by a two-band model or, as in the case of TaP, fits to the longitudinal magnetoresistance described later (tables 4.2.5 and 4.2.6). With the ratio known, the electron mobility for transport along e.g. a, μ^a_{el} is computed such as

$$\mu^a_{\mathrm{el}} = \frac{\sigma^a}{e(n + \xi^c p)}. \tag{4.2.6}$$

The c-axis mobility ratio enters because a Hall or longitudinal magnetoresistance measurement with field along c is governed by cyclotron orbits in the a plane, which is of interest here. In a similar spirit, the transport lifetime τ^a_{tr} is computed such as

$$\tau^a_{\mathrm{tr}} = \frac{\mu^a \cdot m^*_c}{e}, \tag{4.2.7}$$

involving the effective mass as determined from a quantum oscillation measurement with field along the c axis.

The c axis mobilities and transport lifetimes are determined in a similar: Here, the effective masses from a dHvA measurement with field along a enter as well as the

Table 4.2.2. – Transport parameters of NbAs: The resistivity anisotropy, mobilities from magnetoresistance fits and transport scattering times τ_{tr}. Effective masses and Dingle scattering times as determined by dHvA measurements are presented as well.

transport analysis	$I\|\|a$	$I\|\|c$
$\rho(2\,\mathrm{K})$	$2.3\,\mu\Omega\,\mathrm{cm}$	$30\,\mu\Omega\,\mathrm{cm}$
$\rho_{\mathrm{c}}/\rho_{\mathrm{a}}$	-	13
mobility ratio	-	10
electron mobility μ_{e}	$2.6\,\mathrm{T}^{-1}$	$0.2\,\mathrm{T}^{-1}$
hole mobility μ_{h}	$26\,\mathrm{T}^{-1}$	$2\,\mathrm{T}^{-1}$
electron transport scattering time $\tau_{\mathrm{tr}}^{\mathrm{e}}$	$8\cdot10^{-13}\,\mathrm{s}$	$2\cdot10^{-13}\,\mathrm{s}$
hole transport scattering time $\tau_{\mathrm{tr}}^{\mathrm{h}}$	$1.5\cdot10^{-11}\,\mathrm{s}$	$2.3\cdot10^{-12}\,\mathrm{s}$
de Haas-van Alphen analysis	$B\|\|c$	$B\|\|a$
m^*, electron 15.7 T / 72 T	0.055 ± 0.005	0.17 ± 0.01
m^*, hole 21.7 T / 82 T	0.10 ± 0.01	0.20 ± 0.01
τ_{D}, electron 15.7 T	$5\cdot10^{-13}\,\mathrm{s}$	
τ_{D}, hole 21.7 T	$6\cdot10^{-12}\,\mathrm{s}$	

mobility ratio as determined from the longitudinal magnetoresistance with field along *a* (the later, see table 4.2.6). Those actually include orbits in the *a*-*c* plane, but for reasons of simplicity the *a* contribution to this is neglected.

Effective mass and transport parameters of NbAs

The transport parameters of NbAs, gained in a similar way to TaP, are shown in table 4.2.2. The ratio of Hall mobilities and the charge carrier densities are taken from [67], with $\xi = 10$, $n = 1.1\cdot10^{19}\,\mathrm{cm}^{-3}$ and $p = 0.9\cdot10^{19}\,\mathrm{cm}^{-3}$.

The results of an analysis of the quantum oscillations in magnetisation regarding the effective masses of the individual Fermi surfaces and orbits in NbAs can also be found in table 4.2.2, together with the Dingle scattering times τ_{D}. The Dingle scattering times fit reasonably well to the transport lifetimes.

Effective mass and transport parameters of NbP

Unfortunately, data on the mobilities retrieved by a two band model from the Hall conductivity is scarce. The only reference shows results at 100 K [70], where the mobilities have not yet saturated to their low-temperature value. Still, a ratio between

Table 4.2.3. – Transport parameters of NbP: The resistivity anisotropy, mobilities from magnetoresistance fits and transport scattering time τ_{tr}.

transport analysis	$I\|\|a$	$I\|\|c$
$\rho(2\,\mathrm{K})$	$1.2\,\mu\Omega\,\mathrm{cm}$	$5\,\mu\Omega\,\mathrm{cm}$
$\rho_{\mathrm{c}}/\rho_{\mathrm{a}}$	-	4
mobility μ from zero field conductivity	$29\,\mathrm{T}^{-1}$	$7\,\mathrm{T}^{-1}$
mobility μ from magnetoresistance	$17\,\mathrm{T}^{-1}$	-
scattering time τ_{tr}	$0.7 \cdot 10^{-11}$-$1.2 \cdot 10^{-11}\,\mathrm{s}$	$0.2 \cdot 10^{-11}$-$2 \cdot 10^{-11}\,\mathrm{s}$
de Haas-van Alphen analysis	$B\|\|c$	$B\|\|a$
m^*, E2 $6.7\,\mathrm{T}$	0.045 ± 0.005	
m^*, E1 $12.6\,\mathrm{T}$	0.050 ± 0.005	
m^*, $B\|\|c$, E1 / H1? $31.7\,\mathrm{T}$	0.074 ± 0.005	
m^*, $0.7\,\mathrm{T}$		0.016 ± 0.003
m^*, $2.6\,\mathrm{T}$		0.05 ± 0.05
m^*, $34\,\mathrm{T}$		0.18 ± 0.02
m^*, $60\,\mathrm{T}$		0.18 ± 0.02
τ_{D}, $B\|\|c$, all frequencies	$\sim 1 \cdot 10^{-12}\,\mathrm{s}$	

hole to electron mobilities of less than two is suggested, again with the hole mobility being the higher one. If both types of charge carriers contribute to the conductivity with a similar mobility, a single-band model is sufficient for the description and only those mobilities and scattering times are presented in table 4.2.3. The effective masses were again determined from an analysis of the de Haas-van Alphen oscillations. The spread of the transport scattering time τ_{tr} is a result of the spread of the effective masses. Apparently, τ_{tr} is isotropic within experimental errors.

Since the quantum oscillation frequencies in NbP are slightly different to the ones published by Klotz *et al.* [14], it was not always possible to assign all frequencies to particular orbits in the results presented in table 4.2.3. Where this could be done, for $B||c$, the notation of Klotz *et al.* was used.

Effective mass and transport parameters of TaAs

Results in TaAs are most scarce of all four substances. Regarding the transport parameters this is down to the difficulties to find suitable, single crystalline samples. Especially sample which allow for a measurement of the resistivity along c were impossible

Table 4.2.4. – Effective mass and zero field low-temperature resistivity in TaAs. The labelling of the de Haas-van Alphen orbits is taken from [13].

transport analysis	$I\|\|a$	$I\|\|c$
$\rho(2\,\mathrm{K})$	4-5 µΩ cm	
de Haas-van Alphen analysis	$B\|\|c$	$B\|\|a$
m^*, W1 α , 7.1 T	0.068 ± 0.002	
m^*, H1 β, 1.39 T		0.020 ± 0.002

to find. Since not all orbits show up in the de Haas-van Alphen measurement, only the effective mass of the W1 and H1 pocket for field along a and c could be retrieved. Results are presented in table 4.2.4.

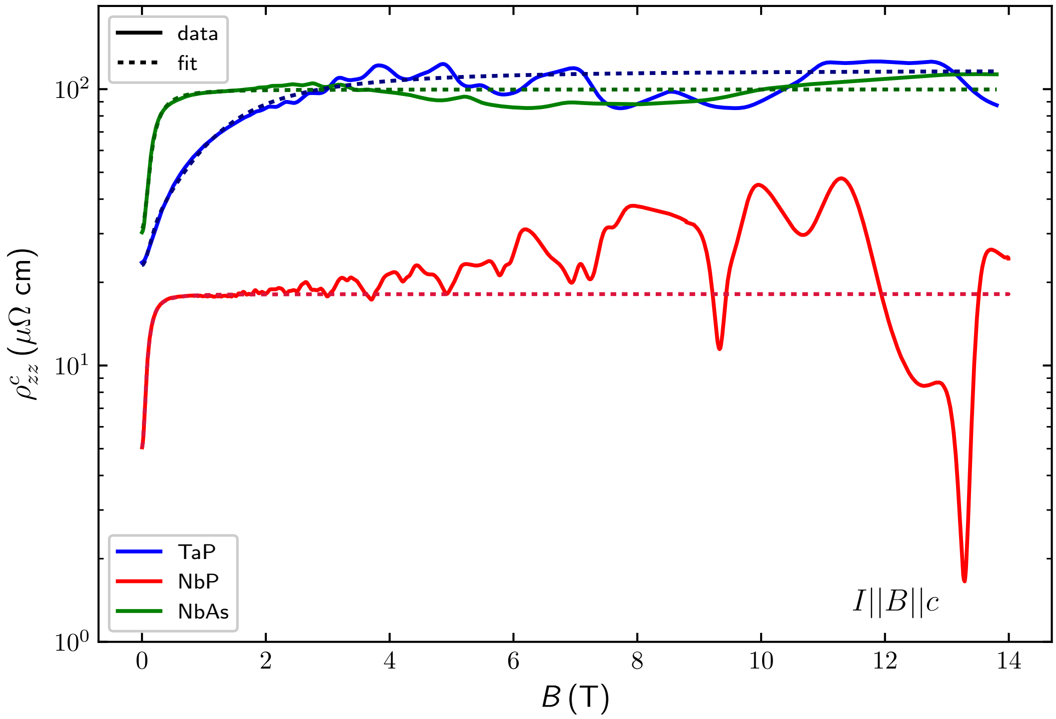

Figure 4.2.8. – The resistivity of TaP, NbP and NbAs along the crystallographic c direction with fits as broken lines describing an orbital magnetoresistance. Fits on TaP between 0-6 T, on the niobium compounds from 0-4 T.

4.2.4. Analysis

B || c - all compounds

Since the resistivity along the c direction in an increasing field rises and saturates without any following downturn it is most likely that orbital effects are at play instead of a weak antilocalisation. The calculations presented in chapter 2.5 also suggest an appreciable change in conductivity for this orientation due to the Fermi surface shape. The following model should be applied:

$$\rho(B) = \left(\sigma_0 + \frac{n_1 e \mu_1}{1 + (\mu_1 B)^2} + \frac{n_2 e \mu_2}{1 + (\mu_2 B)^2}\right)^{-1} \tag{4.2.8}$$

The model has three conductivity contributions: A constant σ_0 which constitutes the saturation value in infinite field and two terms describing a classical orbital magnetoresistance with charge carrier densities $n_{1/2}$ and mobilities $\mu_{1/2}$ as free parameters [2].

However, not all of these five free parameters are needed to explain the results in the three compounds presented. The calculations presented in chapter 2.5 suggest, that in NbAs there is only one band dominating the c-axis transport. In this case it should be possible to explain the c-axis longitudinal magnetoresistance with only one channel subject to a classical magnetoresistance, fixing $n_2 = 0$. In NbP there are two bands dominating roughly equally (table 2.5.2). However, Hall data [70] suggest the mobility of these two to be similar. Here, it should also be possible to fit the data with a reasonable quality and just one channel. Therefore, only in TaP the full model has to be applied. The fits shown in figure 4.2.8 prove this reasoning to be sound. The fit parameters and the experimental and theoretical changes in conductivity in field can be found in table 4.2.5, with the theoretical $\delta\sigma/\sigma$ calculated from the Fermi surface geometry as presented in chapter 2.5. The uncertainties in the fit parameters were determined by performing the fit on data originating from various contacts and over different field intervals.

The results can be compared against the expected change in conductivity in field based on the calculations presented in chapter 2.5 and the in-plane transport mobilities which can be found in tables 4.2.1 (TaP), 4.2.2 (NbAs) and 4.2.3 (NbP). The biggest deviation of 25 % in the change in conductivity can be found in TaP, while in both niobium compounds the agreement is 10 % or better. The mobilities found by the fit also agree with the transport mobilities μ^a, with NbP showing the biggest discrepancy of $17\,\mathrm{T}^{-1}$ vs. $29\,\mathrm{T}^{-1}$. This is probably due to the number of bands contributing in this system: Although the electron and hole mobilities might by very similar, the result for both the a axis transport and the (cyclotron) mobility found here is still composed of contributions from three bands (see table 2.5.2). Some variation between mobilities found by different methods is therefore not unexpected.

Table 4.2.5. – The resulting fit parameters for the field dependent resistivity along c in NbAs, NbP and TaP according to Eq. 4.2.8. For comparison, the expected change in conductivity in field ($\delta\sigma/\sigma$ (theory)) according to chapter 2.5 and the transport mobilities along a, μ^a as discussed in the previous chapter 4.2.3 are shown as well.

TaP	
n_1	$(7 \pm 2) \cdot 10^{16}\,\mathrm{cm}^{-3}$
n_2	$(3 \pm 1) \cdot 10^{16}\,\mathrm{cm}^{-3}$
σ_0	$(8.5 \pm 1.0) \cdot 10^{5}\,\mathrm{S\,m}^{-1}$
μ_1	$(1 \pm 1)\,\mathrm{T}^{-1}$
μ_2	$(4 \pm 1)\,\mathrm{T}^{-1}$
μ^a	$1.6\text{-}6.4\,\mathrm{T}^{-1}$
$\delta\sigma/\sigma$ (exp)	0.77
$\delta\sigma/\sigma$ (theory)	0.96
NbP	
n	$(5.1 \pm 0.3) \cdot 10^{16}\,\mathrm{cm}^{-3}$
σ_0	$(5.5 \pm 0.2) \cdot 10^{6}\,\mathrm{S\,m}^{-1}$
μ	$(17 \pm 1)\,\mathrm{T}^{-1}$
μ^a	$29\,\mathrm{T}^{-1}$
$\delta\sigma/\sigma$ (exp)	0.7
$\delta\sigma/\sigma$ (theory)	0.73
NbAs	
n	$(1.4 \pm 0.1) \cdot 10^{16}\,\mathrm{cm}^{-3}$
σ_0	$(1.02 \pm 0.04) \cdot 10^{6}\,\mathrm{S\,m}^{-1}$
μ	$(10 \pm 2)\,\mathrm{T}^{-1}$
μ^a	$2.6\text{-}26\,\mathrm{T}^{-1}$
$\delta\sigma/\sigma$ (exp)	0.7
$\delta\sigma/\sigma$ (theory)	0.77

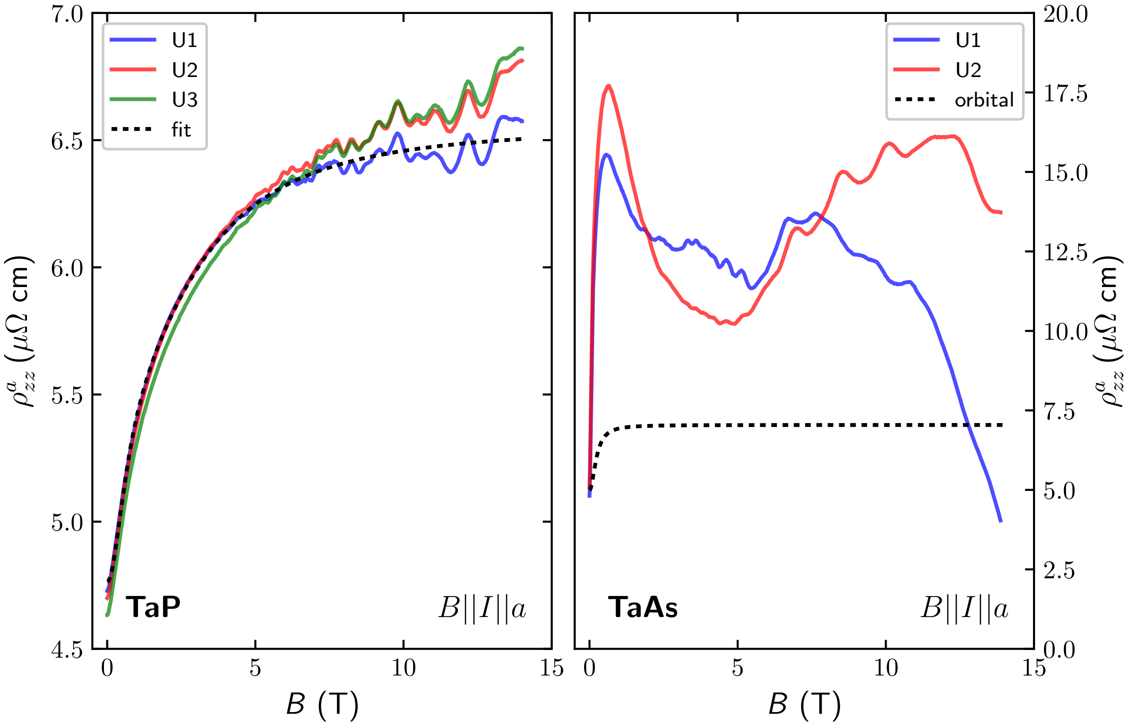

Figure 4.2.9. – The resistivity of TaP and TaAs along the crystallographic a direction. For TaP, a fit according to a model taking only orbital effects into account is shown. On the right, the expected size of the orbital magnetoresistance in TaAs is illustrated with an assumed mobility of $5\,\mathrm{T}^{-1}$.

B || a - **TaX**

Table 4.2.6. – The resulting fit-parameters for the LMR in TaP with field along a according to eq. 4.2.8. The expected change in conductivity in field ($\delta\sigma/\sigma$ (theory)) according to chapter 2.5 and the transport mobilities along a, μ^a as discussed in the previous chapter 4.2.3 are shown as well.

n_1	$(5 \pm 1) \cdot 10^{17}\,\mathrm{cm}^{-3}$
n_2	$(1.3 \pm 0.1) \cdot 10^{17}\,\mathrm{cm}^{-3}$
σ_0	$(15 \pm 1) \cdot 10^{6}\,\mathrm{S\,m}^{-1}$
μ_1	$(0.3 \pm 0.1)\,\mathrm{T}^{-1}$
μ_2	$(1.6 \pm 0.3)\,\mathrm{T}^{-1}$
μ^c	0.27-1.43 T^{-1}
$\delta\sigma/\sigma$(exp)	0.28
$\delta\sigma/\sigma$(theory)	0.24

Figure 4.2.9 presents the resistivity determined from all contact pairs on TaP and TaAs with current along a.

For TaP, a fit to the resistivity is shown. The model applied is the same as the one presented above for current along c, the fit parameters can be found in table 4.2.6. Similar to the fits to the c-axis magnetotransport, both $\delta\sigma/\sigma$ and the mobilities agree with those determined by different methods.

The limited current homogeneity in TaAs makes any attempt of a quantitative analysis or fitting procedure dubious. Still, the absolute change in conductivity can be compared against the expected change due to the orbital magnetoresistance. This is illustrated as black dashed line, with an assumed mobility of $5\,\mathrm{T}^{-1}$. Apparently, the increase in resistivity exceeds this appreciably. This suggests another contribution to the magnetoresistance, responsible for the initial increase and consequently also the following decrease. Since all measurements agree in the low field peak in resistivity, this most likely reflects the true magnetoresistivity of TaAs. It was shown in chapter 3.2.2, that in spite of strong current jetting, the actual longitudinal magnetoresistance is still roughly visible in the signal. If the increase beyond what is expected from the orbital contribution is caused by a weak antilocalisation, the following decrease might be a part of it and not a chiral anomaly. Since this could explain all the features, a proof of the existance of the chiral anomaly in TaAs would require the exclusion of a weak antilocalisation.

In both niobium compounds, a negative longitudinal magnetoresistance can be observed below $3\,\mathrm{T}$ (see figures 4.2.4 (NbAs) and 4.2.5 (NbP)). In NbAs, the decreasing resistivity is preceded by an increase, while in both materials the high field resistivity shows a continuous increase.

$B \mid\mid a$ - **NbX, survey of possible effects**

Since the interpretation of the $B||I||a$ transport in both niobium compounds is the least straightforward so far, all possible effects should be surveyed and discussed. The increasing resistivities might be caused by a number of effects:

- As already observed, an orbital longitudinal magnetoresistance might be responsible. The calculations presented in table 2.5.2 suggest only a modest $\delta\sigma/\sigma$ of 7.5 % in NbAs and 9.7 % in NbP, while the increase in the experiment is around 20 %. Therefore, this possibility can be excluded and any contributions will be neglected in the following discussion.

- Effects sourced in the trivial band structure which come into play at higher fields.

  The fields applied are sufficiently large that the quantum limit of some orbits is in reach or has indeed been crossed: The nested inner pockets in NbAs show quantum oscillations frequencies[1] of 9-30 T, with some orbits ranging to below 1 T (see figure 4.1.3 and [15]). In NbP, frequencies of around 25 T were observed in the literature, while lower are predicted by DFT [14]. Magnetisation measurements show a single frequency below 1 T and more at 34 T and beyond under this orientation. Therefore, the large applied magnetic field may have changed the electronic structure already to some extend.

As described in chapter 5.1, beyond the quantum limit effects such as a decreasing Debye screening length and increasing electron wavelength do influence the longitudinal transport. It cannot be excluded that below, but close to, the quantum limit, somewhat similar effects come into play.

Also, not all possible effects may have been included in the calculations of the orbital longitudinal magnetoresistance.

Therefore, the high field increase may have an intrinsic reason in the 'trivial' electronic structure, which was not taken into account so far. Since these effects would change the scattering time but *not add* separate scattering channels, this would come as an additive conductivity contribution. This intrinsic reason for the high field resistivity increase will be assumed in scenario A.

- A slight misalignment of the sample with respect to the field direction. As described in chapter 3, the sample is mounted on a single axis rotation stage, while the orientation around the second axis of rotation was done by eye. Misalignments around 1° cannot be excluded, which would result in two additional contributions to the resistivity:

  First, an admixture of the transverse magnetoresistance ρ_{xx}. Under the influence of a misalignment of the field with respect to the current, the measured signal is a vectorial superposition of the ρ_{xx} and ρ_{zz} components [32]. Since $\rho_{\mathrm{xx}}(14\,\mathrm{T})/\rho_0 \sim 500$, even a small misalignment might be noticeable, since the total change of longitudinal resistivity is only about 20 %. As a vector addition of magnetoresistances, this is additive to the *magnetoresistance* and should vanish for $B \to 0$.

  Second, for current along a, only the mirror symmetry perpendicular to the field direction preserves the shape of the conductivity tensor as discussed in chapter 2.1.2 and appendix A.1, in particular, the fact that σ_{xz}, σ_{yz} are zero. If the field is rotated away from the a-axis, this mirror symmetry is broken and the relation

---

[1] The quantum oscillation frequency is equal to the quantum limit of a specific orbit, i.e. when the electrons have condensed in the last Landau level or, if other pockets are still present, the last Landau level has left the pocket [16].

$\sigma_{\mathrm{zz}} = \rho_{\mathrm{zz}}^{-1}$ is not valid anymore. Performing the full tensor inversion to arrive at ρ_{zz} from $\hat{\sigma}$ leads to additional terms in the denominator, which can be treated in a Taylor expansion as described in appendix A.1. Here, also additive terms in *resistivity* appear. Those should be zero in zero field, but may be finite in an elevated field.

This symmetry breaking might also occur, if the current does not flow in parallel with the a axis, as it might be caused by small current jetting effects or inhomogeneities in the sample. The latter is a reasonable assumption, since a redistribution of the current within the sample in zero field during cooldowns was observed (not shown).

Both effects would be most pronounced at high fields and may also be responsible for the high field increase in resistivity seen in both samples. These effects, additive in resistivity, are the basis of scenario B.

- A weak antilocalisation (WAL) from quadratic (trivial) bands might show as an increasing resistivity if the ratio $\tau_\phi/\tau_{\mathrm{so}}$ is chosen appropriately as shown in figure 2.6.2. This would naturally come along with a decreasing resistivity afterwards.
- A weak antilocalisation caused by Weyl quasiparticles, as presented in figure 2.6.3. This would only be expected in a system with separate Weyl Fermi surface pockets, i.e. NbAs. The effect would result in a purely positive magnetoresistance, if inter-valley scattering and correlations are small, as described in chapter 2.6.1.

A decreasing resistivity might have three reasons:

- A weak antilocalisation from 'trivial' quasiparticles will always present itself in this way in three spatial dimensions (again, see chapter 2.6).
- A chiral anomaly, as discussed in chapter 2.7, which is only possible in NbAs, since NbP does not host individual Weyl pockets.
- As was discussed in chapter 4.2.3, the Weyl semimetals investigated here contain up to 100 ppm of magnetic impurities, which may give rise to a negative longitudinal magnetoresistance at low temperatures due to the Kondo effect [71]. This was observed in gold doped with similar concentrations of iron. In order to show any influence of the magnetic impurities on the resistivity, it is necessary that the temperature is roughly equal or smaller than the Kondo temperature T_{K}. This scales with the bandwidth of the system B and the density of states at the Fermi energy, $N(E_{\mathrm{F}})$, such as $T_{\mathrm{K}} \sim B \exp(-1/(2JN(E_{\mathrm{F}})))$, where J is

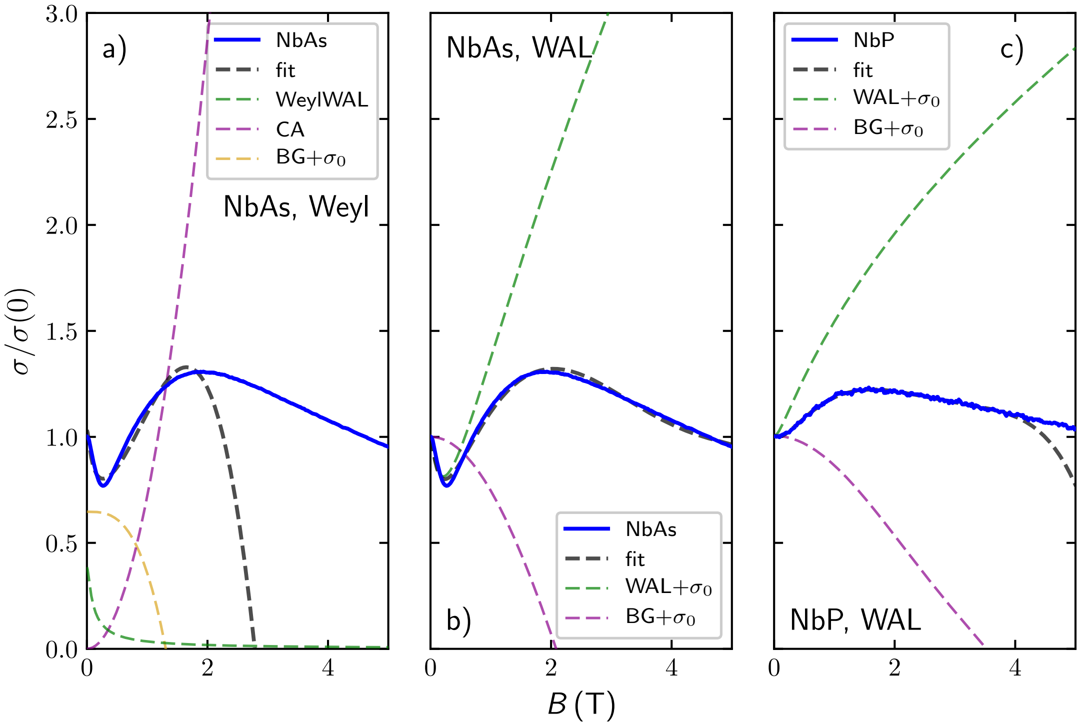

Figure 4.2.10. – Fits to the normalised conductivities for current and field along a in both niobium compounds. a) Fit to NbAs of σ^{Weyl} in a range 0-3 T, with $\sigma_{\mathrm{BG}} = a \cdot B^3$. b) Fit to NbAs of σ^{WAL} in a range of 0-4 T with $\sigma_{\mathrm{BG}} = a_1 \cdot B^2 + a_2 \cdot B^3 + a_3 \cdot B^4$. c) Fit to NbP of σ^{WAL} in a range of 0-4 T with $\sigma_{\mathrm{BG}} = a_1 \cdot B^2 + a_2 \cdot B^4 + a_3 \cdot B^5$. The individual contributions were sometimes offset to σ_0 for clarity.

the coupling between the impurity and the electron spins [72]. Compared to the 'good metal' gold, the semimetals investigated here have bandwidths and densities of states which are about 10 to 100 lower. Given the exponential, this should suppress T_{K} well into the mK range or even below, making any influence of magnetic impurities on the transport very unlikely. Also, the observed contribution to the resistivity in iron doped gold is on a scale of a few ten nΩ cm, smaller than the observed few hundred nΩ cm in our samples.

Experimentally, a slight increase in resistivity at low temperatures, as expected in a Kondo scenario, was observed in some samples of TaAs, as well as a saturating increase in NbAs with current along c (not along a as is the case here, see figure 4.2.1). This does not have to be driven by the Kondo effect, as either localisation physics or the temperature dependence of ionized impurity scattering show in a similar manner [73]. The latter is a well known effect in semiconductors. On the other hand, measurements down to below 50 mK in NbAs and TaAs did not show any increase in zero field resistivity at all.

All things combined, magnetic impurities as a reason for the observed negative longitudinal magnetoresistance are extremely unlikely.

Excluding the orbital longitudinal magnetoresistance and influence of magnetic impurities and attributing the high field increase in resistivity to either intrinsic effects or a misalignment leaves only weak antilocalisations of some sort as source of the low-field increase in resistivity in NbAs. Two scenarios have to be considered:

- The low-field magnetoresistance of NbAs might be entirely governed by Weyl fermions, i.e. the increase is caused by a Weyl weak antilocalisation and the decrease caused by a chiral anomaly. At the same time, in NbP, the decrease is caused by a (trivial) weak antilocalisation.
- Since both the chiral and the non-chiral NbAs and NbP come with a negative longitudinal magnetoresistance in some field range, a common cause unrelated to their chirality is likely. This would only be a trivial weak antilocalisation, where the different ratios of $\tau_\phi/\tau_{\mathrm{so}}$ cause the existance or absence of the low-field increase.

To see which of the scenarios is more credible, the magnetoresistance may now be fitted with the respective models. Those should contain terms accounting for the low field magnetoresistance, i.e. a WAL, Weyl WAL or a chiral anomaly, and the high field background. If misalignments are excluded, all effects contribute as influences to the conductivities and not as additional scattering channels. This is assumed in the following scenario A, where the background is added as a sum of conductivities.

Scenario A

The model taking Weyl fermions into account, σ^{Weyl}, and the one governed by a weak antilocalisation, σ^{WAL}, have the form

$$\sigma^{\mathrm{Weyl}} = \sigma_0 + A \cdot \sigma_{\mathrm{WeylWAL}} + C \cdot B^2 + \sigma_{\mathrm{BG}}, \tag{4.2.9}$$

$$\sigma^{\mathrm{WAL}} = \sigma_0 + A \cdot \sigma_{\mathrm{3DWAL}} + \sigma_{\mathrm{BG}}. \tag{4.2.10}$$

Here, σ_0 constitutes a field independent offset, $\sigma_{\mathrm{WeylWAL}}$ is a Weyl weak antilocalisation as presented in equation 2.6.8, σ_{3DWAL} is a weak antilocalisation as found in equation 2.6.7 and σ_{BG} is a background suitable to model the high field magnetoconductivity which is some polynomial in B. This was found by trial and error, such that an as good as possible fit was possible with as few as possible parameters.

Table 4.2.7. – Fit parameters of the conductivity models σ^{Weyl} (Eq. 4.2.9) and σ^{WAL} (Eq. 4.2.10) for the fits presented in figure 4.2.10. The following polynomials were used for the background: NbAs Weyl: $\sigma_{\text{BG}} = a \cdot B^3$, NbAs WAL: $\sigma_{\text{BG}} = a_1 \cdot B^2 + a_2 \cdot B^3 + a_3 \cdot B^4$, NbP WAL: $\sigma_{\text{BG}} = a_1 \cdot B^2 + a_2 \cdot B^4 + a_3 \cdot B^5$

NbAs Weyl		NbAs WAL		NbP WAL	
σ_0	0.65	σ_0	1.04	σ_0	1.005
A	1.26	A	0.016	A	0.004
l	103 nm	B_ϕ	9.4 mT	B_ϕ	26 mT
$l_\phi - l$	1 nm	B_{so}	62 mT	B_{so}	34 mT
C	$0.72\,\text{T}^{-2}$	a_1	$-0.69\,\text{T}^{-2}$	a_1	$-0.15\,\text{T}^{-2}$
a_1	$-0.282\,\text{T}^{-3}$	a_2	$0.15\,\text{T}^{-3}$	a_2	$0.01\,\text{T}^{-4}$
		a_3	$-0.01\,\text{T}^{-4}$	a_3	$-0.0016\,\text{T}^{-5}$

All fits were performed in the range 0-4 T with a seven fold increased weight between 0-0.8 T to account for the strong variation of the conductivity in this range.

The results of the fit and the field dependence of the individual terms can be seen in figure 4.2.10. The σ^{Weyl} model shown in a) does not yield a good agreement. One reason for this are difficulties finding an appropriate background to model the high field increase. The one shown, is actually turning negative at low fields, which is unphysical. Also, the negative curvature of the increase in resistivity does not match the positive one of the supposed B^2 contribution of the chiral anomaly. The parameters of the fit are not very physical as well: For weak localisation physics to exist in the first place, a separation of the dephasing length scale l_ϕ and the mean free path l is necessary. As shown in the table of fit parameters 4.2.7, l_ϕ and l are effectively equal, which should rule out the existence of the effect all together.

The agreement of the weak-antilocalisation models in b) and c) is much better. Still, the background conductivity in b) is turning negative at fields below 2 T, which is unphysical, but a result of the strong increase of the conductivity contribution of the antilocalisation. Eventually, at higher fields, the same would be true in NbP, i.e. subfigure c).

Scenario B

If the high field background is assumed to be caused by a misalignments in field, it would give rise to additive contributions to the *resistivity*. Here, the relation $\sigma_{\text{zz}} = \rho_{\text{zz}}^{-1}$ is not exact anymore. As a consequence, a model including a sum of resistivities would

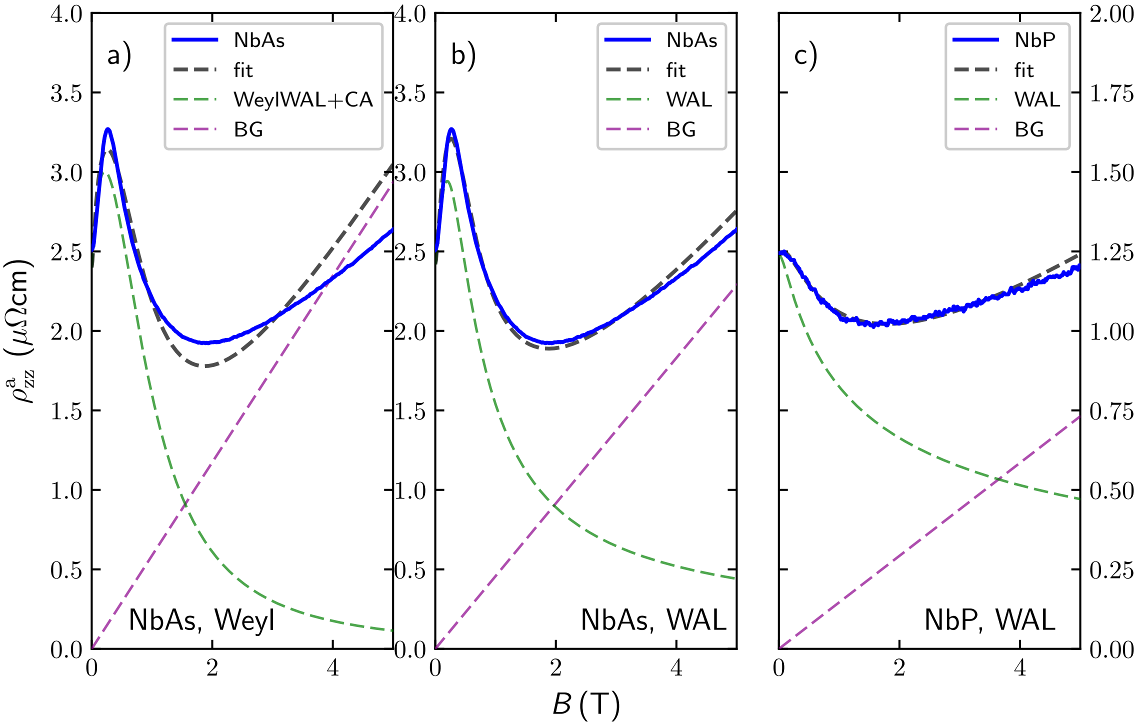

Figure 4.2.11. – Fits to the resistivities for current and field along a in both niobium compounds. The fit range of all fits is 0-4 T. Fit of ρ^{Weyl} (a)) and ρ^{WAL} (b)) to NbAs and of ρ^{WAL} (c)) to NbP. Note the different y-axis scale in subfigure c).

be more appropriate, with the restriction that additive terms vanish for $B \to 0$, such as

$$\rho^{\text{Weyl}} = \frac{1}{\sigma_0 + A \cdot \sigma_{\text{WeylWAL}} + C \cdot B^2} + a_1 \cdot B \tag{4.2.11}$$

$$\rho^{\text{WAL}} = \frac{1}{\sigma_0 + A \cdot \sigma_{\text{3DWAL}}} + a_1 \cdot B. \tag{4.2.12}$$

The linear background can be justified in various ways: First, as first order Taylor approximation. Second, although the lowest field transverse magnetoresistance is quadratic (at a few mT), the high field magnetoresistance, which may be mixing into the longitudinal one due to the assumed misalignment, is almost linear.

Figure 4.2.11 presents fits of both models to the longitudinal resistivity of NbAs and the corresponding fit of ρ^{WAL} to NbP. The general agreement of the model is rather good, with the exception of ρ^{Weyl}, especially if the extremely simple structure of the backgrounds compared to the conductivity fits is considered. An inspection of the fit parameters shown in table 4.2.8 reveals a similar picture to the conductivity fits:

Table 4.2.8. – Fit parameters of the resistivity models ρ^{Weyl} (Eq. 4.2.11) and ρ^{WAL} (Eq. 4.2.12) for the fits presented in figure 4.2.11.

NbAs Weyl		NbAs WAL		NbP WAL	
σ_0	$0.28\,\mathrm{MS\,cm^{-1}}$	σ_0	$2.61\,\mathrm{MS\,cm^{-1}}$	σ_0	$1.26\,\mathrm{MS\,cm^{-1}}$
A	2.33	A	0.035	A	0.0042
l	$112\,\mathrm{nm}$	B_ϕ	$9.7\,\mathrm{mT}$	B_ϕ	$17\,\mathrm{mT}$
$l_\phi - l$	$0.2\,\mathrm{nm}$	B_{so}	$72\,\mathrm{mT}$	B_{so}	$23\,\mathrm{mT}$
C	$0.34\,\mathrm{MS\,cm^{-1}\,T^{-2}}$	a_1	$0.46\,\mathrm{\mu\Omega\,cm\,T^{-1}}$	a_1	$0.15\,\mathrm{\mu\Omega\,cm\,T^{-1}}$
a_1	$0.233\,\mathrm{\mu\Omega\,cm\,T^{-1}}$				

The extremely small difference between the dephasing length l_ϕ and mean free path l of the Weyl weak-antilocalisation renders this model unlikely. At the same time, the dephasing and spin orbit fields B_ϕ and B_{so} are similar to the ones retrieved by the conductivity fits which were presented in table 4.2.7.

The more physical background properties render scenario B, which includes a slight misalignment of the sample in field, more likely.

$B \,||\, a$ - **NbX, discussion**

Basic questions regarding the applicability of the weak antilocalisation model (Eq. 2.6.7) used here may be in order. In most systems where this effect was identified, the changes to the conductivity were at least ten times smaller then in both niobium compounds [74, 75]. How the effect can be this large in our case, is not clear.

The same is true for the Weyl weak antilocalisation [37]. This model appears to be suitable for rather disordered systems, such as the bismuth alloy $\mathrm{Bi}_{1-x}\mathrm{Sb}_x$ on which it was successfully used in references [37, 17]. The mean free paths retrieved by the fits on NbX around 60-100 nm agree with those retrieved by a Dingle analysis[2] and are appreciably larger then the encountered 6 nm in $\mathrm{Bi}_{1-x}\mathrm{Sb}_x$ [17]. This difference may explain the unphysical results and limited fit qualities of the Weyl weak antilocalisation model in both niobium compounds. Reports in the literature which apply this model to members of the TaAs-family rely only on an approximate $\delta\sigma \sim -\sqrt{B}$ model [38, 33, 39]. This is only true for large separations of $l_\phi/l \sim 100$, which may not be fulfilled.

The fits of the 'trivial' weak antilocalisation yields two parameters of physical significance, B_ϕ and B_{so}, from which the corresponding scattering times can be extracted

---

[2] Around 30-300 nm for scattering times of $1 \cdot 10^{-13}$-$1 \cdot 10^{-12}$ s (tables 4.2.2 and 4.2.3) and a Fermi velocity of $3 \cdot 10^5\,\mathrm{m\,s^{-1}}$ [13].

and be checked for the physical credibility. They are related to the scattering times such as $B_\mathrm{i} = \hbar/(4eD\tau_\mathrm{i})$, where $\mathrm{i} = \phi,\mathrm{so}$. Those scattering times can be compared with the total scattering time of the charge carriers, as determined from the transport lifetime τ_tr or from a Dingle analysis τ_D. The latter should be smaller, since in the Dingle analysis, all scattering processes which limit the lifetime of a state enter, while in transport only those which affect the directed movement do. However, the scattering time from the Dingle analysis is more error prone (see chapter 2.8). All parameters would be physically credible if the relation $\tau_\phi \gg \tau_\mathrm{so} \gg (\tau_\mathrm{tr},\tau_\mathrm{D})$ is fulfilled. Since the following discussion is just estimating the credibility of the parameters and is neither capable nor desired to yield precise numbers, the fit parameters as presented in tables 4.2.7 and 4.2.8 are rounded to the ones shown in table 4.2.9.

Starting with the calculation of the scattering times from the fit parameters B_ϕ and B_so, the diffusion constant D of the electrons in NbAs has to be determined first. Having a multiband system at hand, it is not clear whether electrons from a single Fermi surface contribute, or whether inter-valley scattering makes any single band description futile in the first place. Therefore, the diffusion constant could be band specific or an effective diffusion constant from a combination of both. Since it is an impurity driven effect, the band with the lowest mobility and therefore diffusion constant should dominate.

The Einstein relation for the single band diffusion constants of the electron and hole bands, D_e, D_p and the two band diffusion constant D_tb can be calculated such as [1, 76]

$$D_\mathrm{e,p} = \frac{k_\mathrm{B} T \mu_\mathrm{e,p}}{e} \tag{4.2.13}$$

$$D_\mathrm{tb} = \frac{k_\mathrm{B} T_\mathrm{eff}}{e} \frac{n+p}{n/\mu_p + p/\mu_e}. \tag{4.2.14}$$

Here, T, T_eff will be the temperature of the measurement (4 K in NbAs, 2 K in NbP), n, p denote the electron and hole concentrations respectively and $\mu_\mathrm{n,p}$ the respective mobilities. In appendix A.5 the argument is outlined, why $T = T_\mathrm{eff}$ is a reasonable simplification.

For the calculation of the diffusion constant we will rely on the charge carrier densities and mobilities which were already presented in chapter 4.2.3. The single band diffusion constants in NbAs are $D_\mathrm{e} = 9\,\mathrm{cm}^2\,\mathrm{s}^{-1}$ and $D_\mathrm{p} = 90\,\mathrm{cm}^2\,\mathrm{s}^{-1}$, with the two-band average $D_\mathrm{tb} = 18\,\mathrm{cm}^2\,\mathrm{s}^{-1}$. The scattering times together with the transport and Dingle scattering time can be found in table 4.2.9. Apparently, the condition $\tau_\phi \gg \tau_\mathrm{so} \gg \tau_x$, with τ_x as total scattering time, i.e. τ_D or τ_tr, can be fulfilled in some cases. The higher values of τ_ϕ and τ_so are retrieved using the smaller diffusion constant

Table 4.2.9. – Resulting fit parameters of the weak antilocalisation models to the longitudinal magnetoresistance in NbAs and NbP. Parameters were rounded in the light of the results of the conductivity and resistivity fits. The corresponding diffusion constants and scattering times are shown as well.

NbAs				
B_ϕ	$10\,\mathrm{mT}$		$\tau_\mathrm{D}^\mathrm{electron}$	$5 \cdot 10^{-13}\,\mathrm{s}$
B_so	$70\,\mathrm{mT}$		$\tau_\mathrm{tr}^\mathrm{electron}$	$8 \cdot 10^{-13}\,\mathrm{s}$
D	9-90 $\mathrm{cm}^2\,\mathrm{s}^{-1}$		$\tau_\mathrm{D}^\mathrm{hole}$	$6 \cdot 10^{-12}\,\mathrm{s}$
τ_ϕ	$2 \cdot 10^{-12}$-$2 \cdot 10^{-11}\,\mathrm{s}$		$\tau_\mathrm{tr}^\mathrm{hole}$	$1.5 \cdot 10^{-11}\,\mathrm{s}$
τ_so	$3 \cdot 10^{-13}$-$3 \cdot 10^{-12}\,\mathrm{s}$			
NbP				
B_ϕ	$20\,\mathrm{mT}$		τ_D	$0.8 \cdot 10^{-12}$-$1.2 \cdot 10^{-12}\,\mathrm{s}$
B_so	$30\,\mathrm{T}$		τ_tr	$0.7 \cdot 10^{-11}$-$1.2 \cdot 10^{-11}\,\mathrm{s}$
D	29-50 $\mathrm{cm}^2\,\mathrm{s}^{-1}$			
τ_ϕ	$2 \cdot 10^{-12}$-$3 \cdot 10^{-12}\,\mathrm{s}$			
τ_so	$1 \cdot 10^{-12}$-$2 \cdot 10^{-12}\,\mathrm{s}$			

of the electron band, which has smaller total scattering times below $1 \cdot 10^{-12}\,\mathrm{s}$ which readily fulfils the inequality. On the other hand, the parameters of the hole band suggest dephasing times shorter than the transport scattering times which rules out the effect altogether.

In NbP, the relation between the scattering times does not favour a weak antilocalisation model. While the dephasing times are on the same scale as in NbAs, the extremely long Dingle and transport scattering times around $1 \cdot 10^{-12}$-$1 \cdot 10^{-11}\,\mathrm{s}$ make the applicability of the model dubious, at least for the parameters observed here. It may be possible that some band with a lower mobility is carrying the antilocalisation, which is 'silent' in quantum oscillations. As an example, band 18 is supposed to contribute about 18 % to the a-axis transport, at least according to its shape, but is not observed in quantum oscillations, therefore no Dingle scattering time is known.

4.3. Discussion and outlook

The Weyl semimetals in general, and the TaAs family of Weyl semimetals in particular, promise the opportunity to study effects related to three-dimensional Weyl fermions. One of the effects caused by these chiral fermions is the so called chiral anomaly, presenting itself as a negative longitudinal magnetoresistance. So far, their possible influence was obscured by an artefact caused by the large conductivity anisotropy in these compounds, the so called current jetting, which has a similar signature.

The work presented here constitutes the first reliable investigation of the longitudinal magnetoresistance in TaAs-type Weyl semimetals in search for evidence of a chiral anomaly known to us. By developing a soldering procedure to attach the current contacts, the current was injected in a rather homogeneous way. This was monitored by a number of voltage probes allowing for a spatially resolved measurement of the potential distribution. In most cases, the achieved current homogeneities were sufficient to draw quantitative conclusions. Of all materials, TaAs is the most interesting, but also the most elusive in the investigation: Single crystals of appreciable size were almost impossible to come by and it proved extremely challenging to make homogeneous current contacts since it was almost impossible to wet with any liquid metal.

Trying to understand the influence of inhomogeneous current contacts better, simulations of the potential distribution in a sample with imperfect current contacts were performed. This was done using self-developed code utilising experimental data for the components of the conductivity tensor. If current contacts did not cover the whole width of a sample, the main potential gradient was found to be not along the length of a sample rather then along its width. This made any misalignment of contacts a source of a possible sign inversion of the voltage in an increasing magnetic field, i.e. giving rise to negative resistances. Still, qualitatively, the 'true' longitudinal magnetoresistance of the material remained visible in the experimental results.

To further aid the interpretation of the acquired data, the expected size of the orbital magnetoresistance was calculated from the known bandstructure. The results were found to be in agreement with experimental data, showing the c axis transport to be almost exclusively dominated by orbital effects. Along the a-axis, both tantalum compounds are expected to have an appreciable contribution from orbital effects, while they are almost absent in both niobium compounds.

For $B||I||a$, both NbP and NbAs show a negative longitudinal magnetoresistance. This is surprising to some extend, since NbP should not host any individual Weyl-pockets, therefore a chiral anomaly should be at least strongly suppressed. The most likely interpretation is the existence of a weak antilocalisation which is able to qualitatively explain the full low-field longitudinal magnetoresistance in both compounds.

Despite this qualitative agreement, some questions remain, especially regarding the large size of the effect. However, there is no other possible explanation known to us, which is able to explain the positive longitudinal magnetoresistance in NbAs and the negative one in both materials.

In TaAs, the low-field longitudinal magnetoresistance along a is probably qualitatively similar to the one observed in NbAs. There appears to be an excess of positive magnetoresistance over the expected size of the orbital contribution which is followed by a negative longitudinal magnetoresistance. This also suggests the presence of weak antilocalisation physics, although the data is more ambiguous.

In conclusion, the observation of a chiral anomaly in these compounds is rather questionable and other effects such as weak localisation physics are more likely to be responsible. As a general conclusion, it can also be stated that searching for some experimental signature, of e.g. a chiral anomaly, in electronic transport is ambiguous, due to the number of possible effects which are difficult to distinguish.

A more thorough investigation of the longitudinal magnetoresistance in both niobium compounds and TaAs would be a project that could easily fill a possible future thesis. Experimentally, two things would be required: Firstly, it would be advisable to use microstructuring, since this yielded the best qualitative results in the investigation. To avoid misinterpretation due to the possible influence of the degraded surface layer, cross checks against bulk samples are advisable. Also, the investigation should take place in a vector magnet to allow for precise alignment of the current with respect to the magnetic field along both axes of rotation. Additionally, the influence of different samples with different mean free paths, and the temperature dependence of the effects seen would yield important information on the processes involved.

5 | Other projects

5.1. $CoSb_3$ - quantum oscillations and quantum limit investigation

5.1.1. Introduction

The cubic skutterudite $CoSb_3$ is a narrow-gap semiconductor. Its electronic structure features a single valence band with its maximum at the Γ point accompanied by three conduction bands which form a direct gap. The structure and band structure of $CoSb_3$ are depicted in figure 5.1.1. Earlier studies on crystals grown by vapour transport and flux methods revealed the material to grow naturally p-doped with charge carrier densities around $1 \cdot 10^{16}$-$1 \cdot 10^{19}\,\mathrm{cm}^{-3}$ [77, 78].

Our interest was sparked by two publications which predict the closing and the following inversion of the gap under application of tetragonal strain, i.e. the compression of the cubic lattice along [100] [79, 80]. This should result in linear bands at least along some crystallographic directions and would enable the study of a continuous transition from a normal semiconductor into a topologically non-trivial material.

To investigate this transition by means of a resistivity measurement, it is necessary to have crystals of reasonable quality with a Fermi energy sufficiently close to the gap. A study and confirmation of the electronic structure, which is so far only known from ab-initio calculations, was also required.

Two sets of samples were investigated by means of quantum oscillations in this project: One grown by a self-flux and a second one using a novel, inclined rotary Bridgman (IRB) method. The latter yielded crystals with a reproducible low charge carrier density. Those presented a suitable model system for an isotropic electron gas with its quantum limit in an experimentally accessible field range. Consequently, measurements in pulsed-magnetic fields at the Dresden High Magnetic Field Laboratory at the Helmholtz Zentrum Dresden Rossendorf were carried out to investigate the quantum limit properties of this system. The quantum limit transport properties were found to be governed by impurity effects in the vicinity of a magnetic field driven charge localisation.

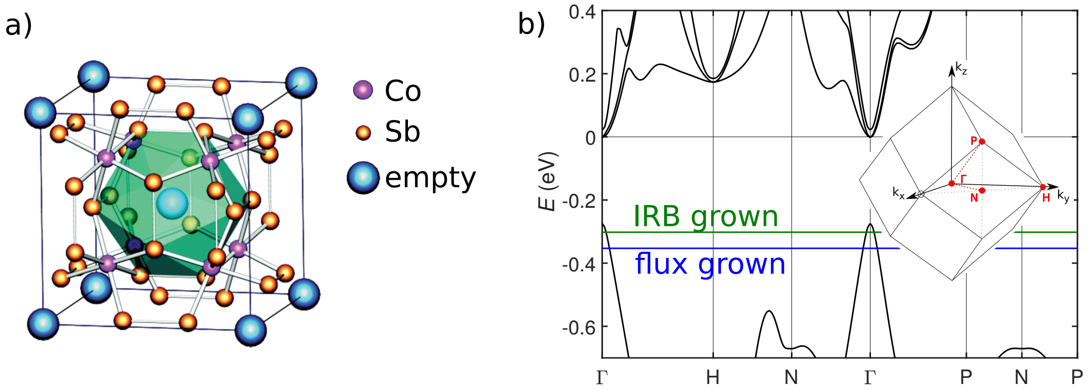

Figure 5.1.1. – a) Structure of $CoSb_3$. In case of this unfilled skutterudite, there are empty sites in the lattice. b) The DFT bandstructure of a GGA calculation including spin-orbit coupling. The Fermi energy of the IRB and flux grown samples as determined by the quantum oscillation frequencies and the known band structure is presented as well.

5.1.2. Sample characterisation

Flux grown samples

Sample growth from an antimony rich self-flux was done by Andreas Leithe-Jasper and Flipo Sever at MPI CPfS. The crystals had a size of up to 1 cm and showed facets along certain high symmetry planes of the cubic lattice, while the bulk of the material hosted some voids of millimetre size. Hall measurements confirmed hole type charge carriers and showed a variation in their charge carrier density in the range of $7 \cdot 10^{18}$-$4 \cdot 10^{19}\,\mathrm{cm}^{-3}$.

The variability in charge carrier concentrations was accompanied by an inconsistency of the results of the quantum oscillations with density-function theory (DFT) calculations, which were done by Helge Rosner. The spectrum of the de Haas-van Alphen oscillations mostly showed a number of peaks, or peaks which appeared to split (see figure 5.1.3). The lower frequencies were between 50-80 T, with higher ones ranging up to 120 T. In contrast, the DFT calculations predict only a single conductance band, which should be rather isotropic. This gives rise to a single, spherical Fermi surface which would yield one quantum oscillation frequency. The corresponding effective masses also disagreed with the ones expected from the DFT calculations (see figure 5.1.2).

Given the existence of voids in the material, charge inhomogeneities are not unexpected, which could explain at least the splitting of the dHvA frequencies: The systematic dependence of the effective mass on the quantum oscillation frequency sug-

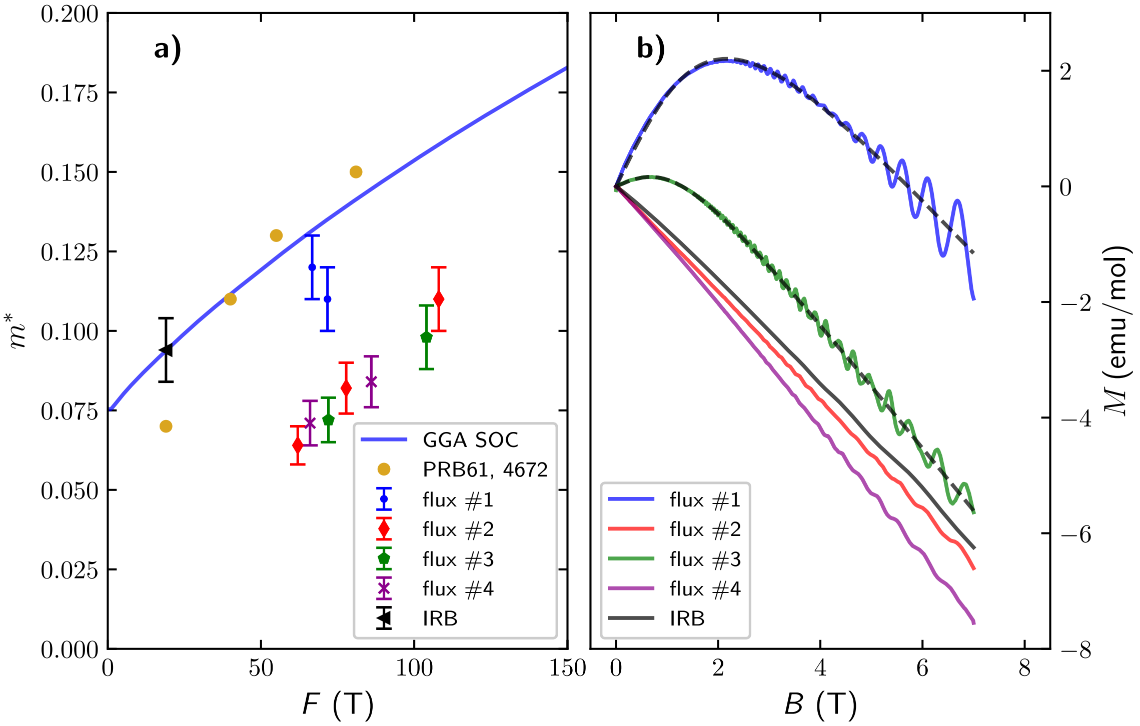

Figure 5.1.2. – a) Relation between the observed quantum oscillation frequency F and the effective mass $m^* = m/m_0$. The DFT GGA calculation including spin-orbit coupling was done by Helge Rosner. The experimental values from the flux and IRB grown samples and results reported in [81] are presented as well. b) Magnetisation versus field for various samples from flux and IRB growth. Flux grown samples which clearly show the presence of magnetic impurities show the largest quantum oscillations. The broken lines denote fits to a Brillouin function which describes the magnetisation of paramagnetic impurities (Eq. 4.2.1).

gests all frequencies to originate from the same band, which implies the formation of well separated domains of different charge carrier density within one crystal.

Also, the unexpected observation was made, that samples which clearly showed the presence of magnetic impurities in magnetisation measurements, had quantum oscillations of a higher amplitude than those where magnetic impurities were apparently absent. Since magnetic impurities are more effective as scatterers [82], the Dingle temperature should be increased, dampening the oscillations. However, samples with magnetic impurity concentrations of $5 \cdot 10^{-5}$-$4 \cdot 10^{-4}\,\mathrm{mol}^{-1}$ showed mean free paths in excess of 200 nm, while those with a factor of ten lower impurity concentrations had mean free paths a factor 2-4 lower.

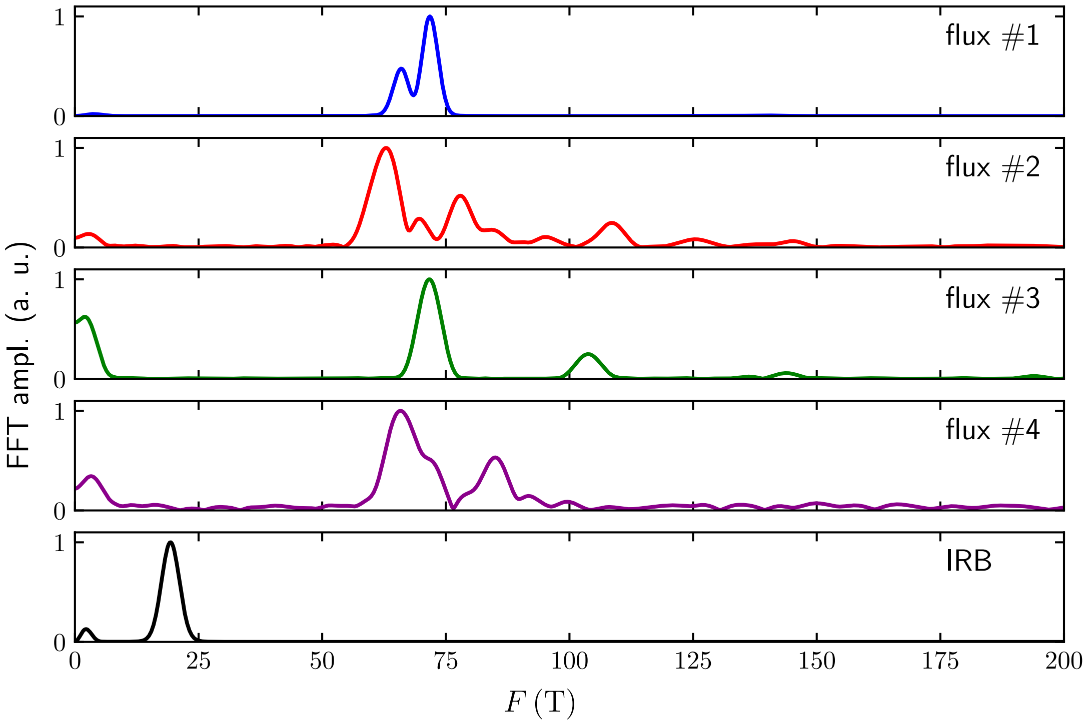

Figure 5.1.3. – Fourier transformed of the de-Haas van-Alphen oscillations observed in four batches of the self-flux grown samples. The Shubnikov de-Haas spectrum of the IRB grown sample is shown as well. The splitting of frequencies is well observable in all flux batches, while the IRB sample shows only a single frequency.

Samples grown by the inclined rotary Bridgman method

At Ludwig-Maximillians-University Munich, samples were grown by an inclined rotary Bridgman (IRB) method by Prof. Peter Gille and Mirtha Pillaca Quispe [83]. In this method, an ampule containing cobalt and an excess of antimony relative to the stoichiometric ratio is placed in an oven, with the assembly inclined by about 15° with respect to the horizon. The ampule is rotated at 100 rpm while it is retracted from the oven at a rate of $2.4\,\mathrm{mm\,d^{-1}}$. The crystals grew as extremely homogeneous material of a few centimetres in size.

Hall measurements revealed them to be hole doped as well, with charge carrier densities of $5 \cdot 10^{17}\,\mathrm{cm^{-3}}$, in full accordance with a single quantum oscillation frequency of 19 T. Also, the effective mass m^* of 0.1 agrees with the prediction of the DFT calculation for this doping level (see figure 5.1.2 a), black marker). The mean free path of 30 nm found in these samples is lower than for flux grown samples.

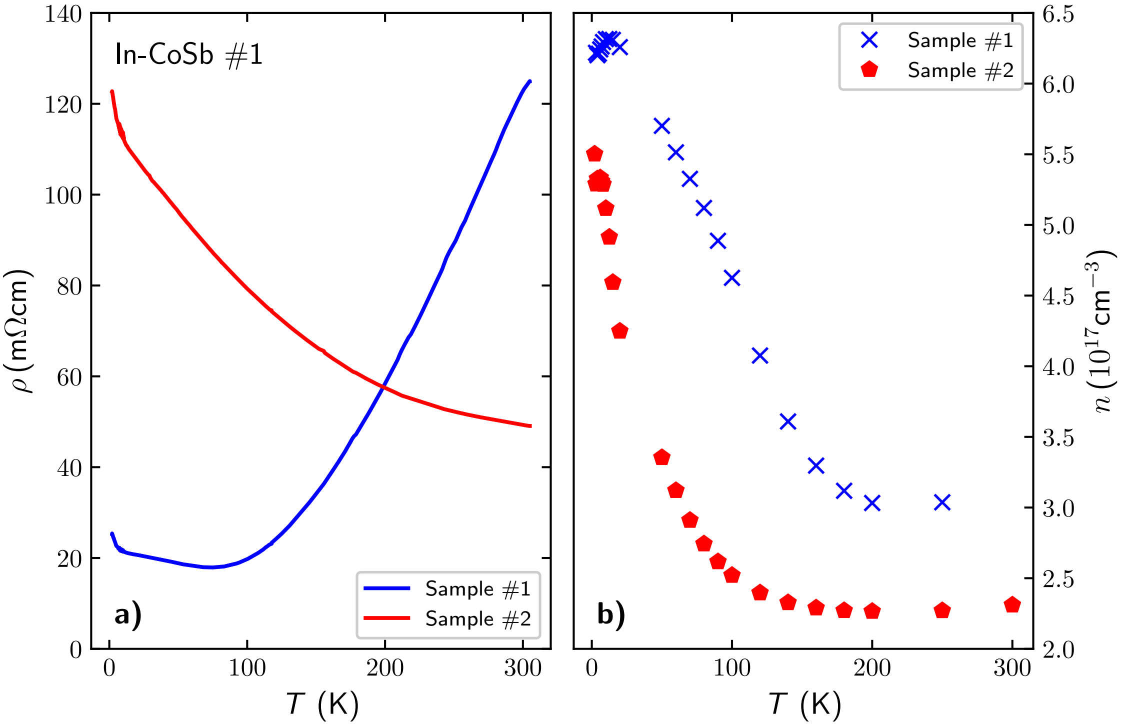

Figure 5.1.4. – Transport properties of batch In-CoSb #1. a) Temperature dependent resistivities. b) Charge carrier density of the same samples over the same temperature range.

Since the Fermi energy was still in the hole band, it was attempted to move it closer to the gap by electron doping with Indium. For this, two batches of the nominal composition In$_{0.05}$Co$_4$Sb$_{12}$ (batch In-CoSb #1) and In$_{0.1}$Co$_4$Sb$_{12}$ (batch In-CoSb #2) were prepared.

The lower-doped batch In-CoSb #1 showed an increasing resistivity upon cooling, in some samples from room temperature on, in others only at lowest temperatures as shown in figure 5.1.4 a). The charge carrier density from the Hall resistivity ρ_{xy}, as determined by a one-band model fit, indicates an increase towards lower temperatures by a factor of 2 (see figure 5.1.4 b). At the same time, the transverse low-temperature magnetoresistance $\Delta\rho_{xx}$ is negative, indicating the presence of an impurity band [84]. A strong influence of impurities in the materials is also indicated by an increasing rather then decreasing mobility with increasing temperature.

Increasing the dopand concentration in batch In-CoSb #2 raises the Fermi energy well into the conduction band. Here, charge carrier concentrations around $1 \cdot 10^{18}$-$1 \cdot 10^{19}$ cm^{-3} electrons were observed, which decrease by about a factor of four upon raising the temperature from 2 K to 300 K, similar to what is observed in batch In-

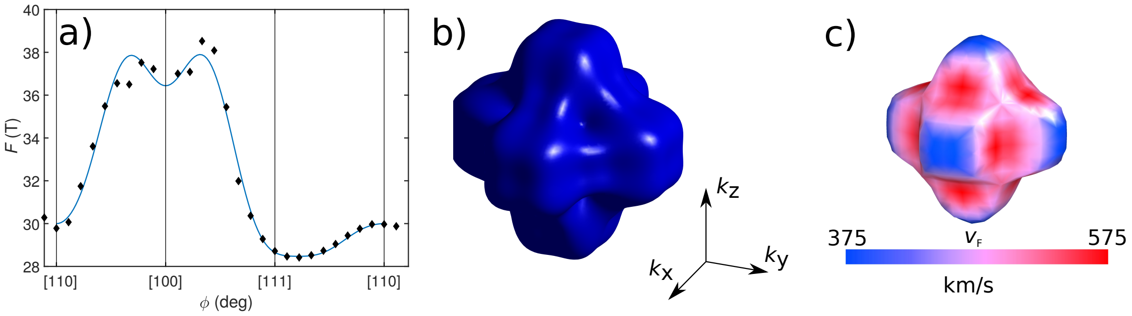

Figure 5.1.5. – Results of the quantum oscillation study on the Indium doped $CoSb_3$, batch In-CoSb #2. a) The angular dependence of the quantum oscillation frequency. b) The reconstructed Fermi surface via a cubic harmonic expansion, fitted to the angular dependence of the SdH frequencies. c) The Fermi surface of the second of the three electron bands (counted from the gap towards higher energies) for a Fermi energy of 0.16 eV. The colour code illustrates the magnitude of the Fermi velocity on the surface.

CoSb #1. From DFT calculations three conductance bands are known. Two of these are degenerate at the Γ point forming the direct gap, while the third is gaped (slightly visible in figure 5.1.1). Since thermal excitations between the bands, and from a possible impurity band, into the higher conductance bands are possible, the change in mobilities and charge carrier density is attributed to multiband effects.

If all indium is assumed to be incorporated homogeneously into the lattice, electronically activated and in the 3+ oxidation state, this is equivalent of an electron concentration of $6 \cdot 10^{20}\,\mathrm{cm}^{-3}$. Clearly, the observed charge carrier densities are smaller and vary between crystals. This indicates a slightly inhomogeneous distribution or activation of dopands. In summary, only one per mille to one percent of the Indium is electronically incorporated into the lattice.

In some samples of batch In-CoSb #2, Shubnikov-de Haas oscillations with frequencies around 25-50 T could be observed. Only two to three maxima of the oscillations could by observed at highest fields, rendering a Fourier transformation not ideal for their analysis. Therefore, the more cumbersome approach of fitting the resistivity with the Lifshitz-Kosevich equation 2.8.3 had to be used. The angle dependent frequency of the quantum oscillations is depicted in figure 5.1.5 a). This angle dependence was used to fit a cubic harmonic expansion[1] of the Fermi surface to it, the result is shown in panel b) of the same figure. While no angle dependence of the quantum oscillation frequency from DFT calculations was available, a picture of the expected shape of the Fermi surface of the lower two of the three conduction bands was. The inner one agreed well with the result of the harmonic expansion (see figure 5.1.5 c)). This is reas-

---

[1] The Matlab code to do this was kindly provided by Frank Arnold.

onable, since the inner band should possess a higher curvature, therefore lower mass and higher mobility, making it more likely to manifest itself in Shubnikov-de Haas oscillations.

5.1.3. High magnetic field measurements

Samples grown by the IRB method provided a model system for the study of an isotropic electron gas confined to its lowest Landau level, which is the case at fields higher than 19 T in these samples. In the quantum limit, the electronic system becomes effectively one dimensional. This can allow electronic correlations to drive the system into various electronic instabilities such as charge- or spin-density waves [85].

Systems which allow for the study of this state such as bismuth or graphite, where new phases have been found [86, 87], suffer from additional complications such as multiple Fermi surfaces and anisotropies. Besides these pure elements, doped semiconductors such as $Hg_{1-x}Cd_xTe$ [88], n-InSb [89] or $SrTiO_3$ [90] offer the possibility to study the quantum limit of an electron gas at a few Tesla, but show disorder driven charge localisations, mostly referred to as magnetic freeze-out, at elevated fields. Given the slightly higher quantum limit field in $CoSb_3$, there was the hope to circumvent the magnetic freeze-out in favour of e.g. an instability, such as a charge-density wave [85].

To investigate this, two samples of IRB grown $CoSb_3$ were prepared for the investigation of ρ_{xx}, ρ_{xy} and ρ_{zz} in pulsed magnetic fields up to 70 T at the Dresden High Magnetic Field Laboratory at the Helmholtz Zentrum Dresden Rossendorf. This experiment was kindly supported by Tobias Förster. Experimentally, the pulse field environment called for special care regarding the preparation of contacts and wiring of the sample, since the large $\mathrm{d}B/\mathrm{d}t$ around $3000\,\mathrm{T\,s^{-1}}$ will cause substantial induced voltages in every open-wire loop.

To cope with the short time scales involved in the measurement, the ac-current used is at a few kHz and the signal at the voltage contacts is digitised without demodulation, with the lock-in demodulation implemented in software. To have full control over the analysis, self-written code was used for the demodulation of the signal.

The results, presented in figure 5.1.6, show an appreciable increase both in ρ_{xx} and ρ_{zz} beyond the quantum limit field of 19 T. At the same time, at lowest temperatures the negative Hall signal bends upwards, indicating an increase in charge carrier density.

Inverting the resistivity tensor to yield conductivities shows the transverse conductivity σ_{xx} to rise after reaching the quantum limit, as can be seen in figure 5.1.7. Therefore, despite the rising resistivity, the conductivity is actually enhanced at high fields and low temperatures.

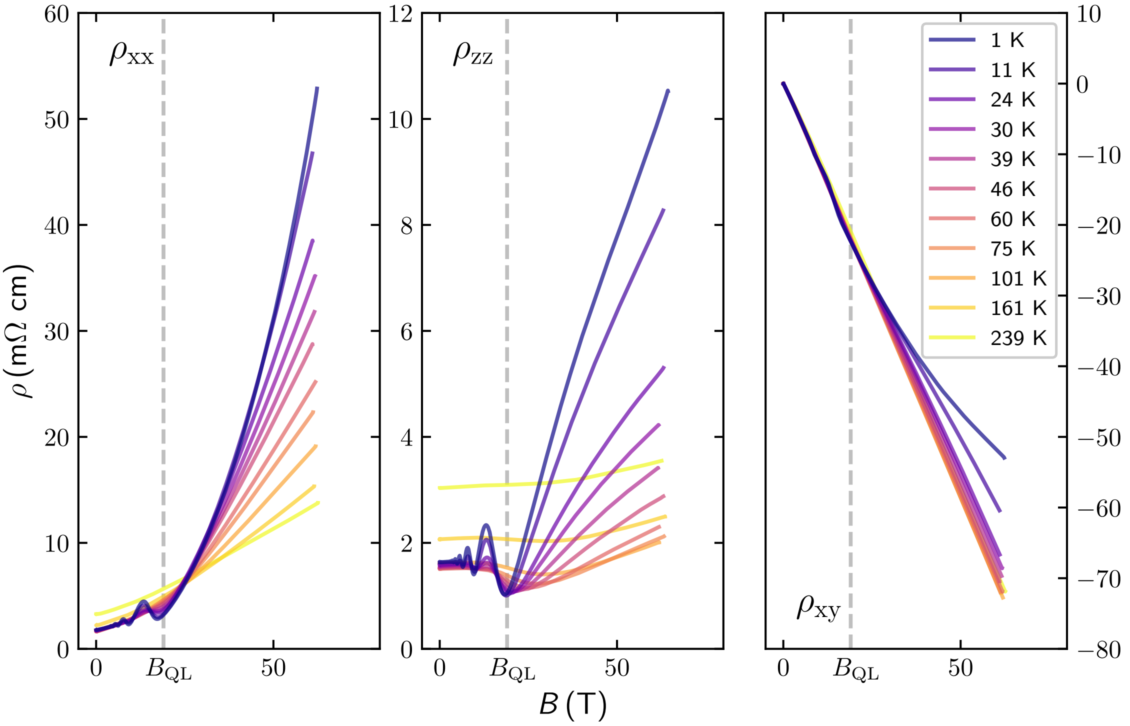

Figure 5.1.6. – Components of the resistivity tensor in high magnetic fields beyond the quantum limit (grey dashed line).

In general, three different field regions can be distinguished: Below the quantum limit, where quantum oscillations are visible, above the quantum limit (the 'intermediate field range') where the transverse conductivity increases in field and at highest fields the onset of the magnetic freeze-out when σ_{xx} is decreasing again.

The intermediate field region can be qualitatively understood in terms of a theory by Murzin *et al.*, which was made to explain the quantum limit transport properties of InSb [89]. In a sufficiently high magnetic field, electrons are confined to the magnetic length $l_m = \sqrt{\hbar/(eB)}$ in the direction perpendicular to the field, inhibiting the transport in this direction. Along the field direction, normal electronic transport can still take place. Here, only scattering on impurities can result in a displacement perpendicular to the field direction, constituting the only charge transport mechanism in the perpendicular direction. Obviously, the more scattering events, the higher the longitudinal resistivity but the better the transverse transport. This is reflected in the $\sigma_{xx} \sim \sigma_{zz}^{-1/3}$ proportionality suggested in [89].

The model outlined above also attempts to explain the field dependence of the longitudinal conductivity σ_{zz}. This is the result of the varying interplay of length scales: The increasing field is lowering the Fermi energy with respect to the band

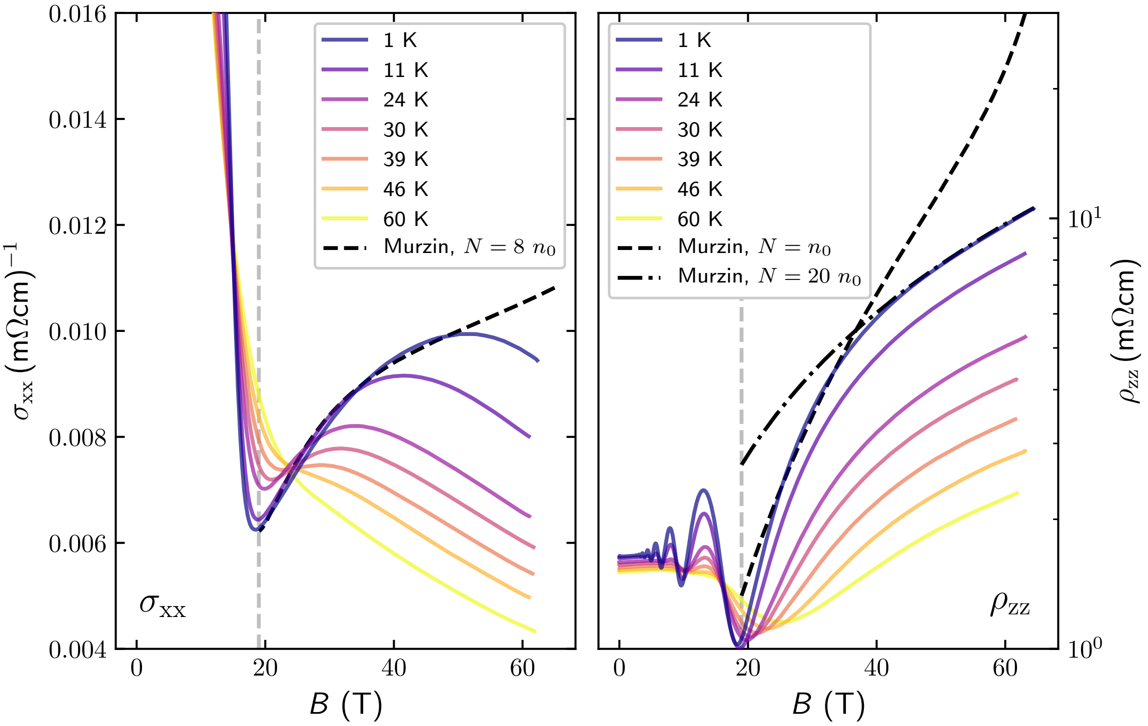

Figure 5.1.7. – The transverse conductivity σ_{xx} and the longitudinal resistivity ρ_{zz} on a log scale. The model by Murzin *et al.* is shown as dashed or dashed-dotted black line in both for the best fitting impurity concentrations N denoted in multiples of the charge carrier density n_0. The quantum limit field is again denoted as grey dashed line.

edge, and with it k_F, resulting in an increased electron wavelength. On the other hand, lowering E_F while keeping the number of charge carriers constant results in an increasing density of states. This increases the dielectric constant and reduces the Debye radius of impurities. In summary, an increasing electron wavelength is meeting impurities which become more and more delta-like, facilitating large angle scattering and increasing the resistivity. Eventually though, the electron wavelength becomes larger than the size of the impurities, which should result in a non-monotonic field dependence of the resistivity. This has not been experimentally observed so far, since the magnetic freeze-out is typically happening at lower fields [89].

The model of Murzin *et al.*, describing the intermediate field range, has two parameters: One is the impurity concentration, assumed to be equal to the charge carrier concentration. This assumption might not be true for a number of reasons: For once, different kinds of impurities might compensate themselves, making them electronically neutral. Other impurities might not be electronically activated as in the case of the indium of the doped batch In-CoSb #2. Finally, lattice defects such as antisites may act as scatterers but are electronically neutral as well. Therefore, the impurity concentration cannot be fixed to the charge carrier concentration. The second parameter is the size of the effect. This was adjusted such, that both model and experimental data would coincide at 40 T. Since the calculation came with some numerical effort, both parameters were not optimised by a fit algorithm but by hand.

Figure 5.1.7 presents the result of the model for σ_{xx} and σ_{zz}, the latter shown as its inverse ρ_{zz}. The best agreement with the data was achieved by setting the impurity concentration to be eight times the charge carrier density. On the right hand side, the longitudinal resistivity is shown, together the model from Murzin *et al.*, once such that it fits at low fields and once such that a good fit at high fields is achieved. This also illustrates the influence of the impurity concentration on the predicted resistivity. Still, the model does not explain the field dependence of ρ_{zz} satisfyingly. In general, both models tend to underestimate the curvature of σ_{xx} and ρ_{zz}.

As a result, the high field measurements on $\mathrm{CoSb_3}$ allowed for the study of an isotropic electron gas, where quasi particles are confined to the lowest Landau level but the metal insulator transition has not yet taken place. The transverse transport was found to be in agreement with an existing theory by Murzin *et al.*, describing a dependence of σ_{xx} on the longitudinal conductivity σ_{zz}. The modelling of the longitudinal transport can account for the increase in resistivity, but has shortcomings describing the curvature of $\rho_{\mathrm{zz}}(B)$.

Further progress on this field, could be made in two directions: To study the metal insulator transition, lower temperatures well into the mK range would be necessary [91]. Also, samples with a range of, probably lower, charge carrier concentrations would allow for a more in-depth investigation of the intermediate field region.

Another, probably experimentally more challenging route would be a system with highest possible mean free path, allowing for the study of an unperturbed, isotropic 3D electron gas at highest fields.

5.1.4. Conclusion

In this project it was shown that samples of $\mathrm{CoSb_3}$, grown by a flux method, are hole-doped with charge carrier densities around $1 \cdot 10^{18}\,\mathrm{cm}^{-3}$ and mean free paths around 100 nm, in few samples up to 250 nm. The most severe limitation of this method is the inhomogeneity of the crystals and lacking reproducibility. The inclined rotary Bridgman method on the other hand reproducibly yielded crystals of great homogeneity and lower charge carrier density, but with a lower mean free path around 30 nm. One possible explanation for these rather modest mean free paths is that antimony can have positive as well as negative valencies, making it able to occupy the cobalt site in the lattice thus creating a defect. This inhibits the growth of highest quality single crystals.

The study of the high magnetic field properties qualitatively recovered the quantum limit transport properties of InSb or $Hg_{1-x}Cd_xTe$ before the onset of the magnetic freeze-out. Quantitatively, differences especially in the longitudinal transport were found, which illustrates the complexities of the description of the transport properties in this regime.

5.2. UBe_{13} - sample characterisation and high field resistivity

5.2.1. Background

The cubic compound UBe_{13} was first reported as a heavy fermion superconductor in 1983 [92]. Interest was growing quickly for a number of reasons. The Sommerfeld coefficient just above T_c of around $1\,\mathrm{J\,mol^{-1}\,K^{-2}}$ is one of the largest ever reported. Further, the upper critical field around 13 T is way higher than could be expected from the low critical temperature of around 0.9 K in a typical BCS picture. Together with the 5f-character from the Uranium orbitals this renders the occurrence of an unusual pairing symmetry rather likely.

The investigation of single crystalline sample quickly showed a variation in their low-temperature properties [93]: In some samples, the Sommerfeld coefficient $\gamma = C_{\mathrm{el}}/T$, C_{el} being the electronic specific heat, is rising upon lowering the temperature towards the superconducting transition. Here, the critical temperature T_c of around 0.7 K is lower than in other samples. This type of crystals was denoted as *low-type* or short l-type crystals. The other variety showed a higher T_c around 0.9 K, slightly lower but temperature independent specific heat and a lower jump at T_c. Those were called *high-type* samples. The reason why some samples were of the one or the other kind was unknown for many years. Since the difference only occurred in single crystals, the aluminium flux method was speculated to be responsible for it.

The growth of single crystals in UBe_{13} faces the problem, that the melting point of the material of about 2000 °C is higher than the temperatures typical ovens and crucibles can achieve and withstand [94]. Therefore, the polycrystalline material is dissolved in aluminium, which serves as a flux and lowers the melting point. Upon slowly cooling the mixture, UBe_{13} crystals start to precipitate in the flux. Afterwards, the rest of the aluminium is etched away and only the desired crystals are left over. Naturally, this process gives the aluminium the chance to act as an impurity in the lattice, if the solubility is high enough. Structurally, it is extremely difficult to resolve this, since typical methods rely on x-ray diffraction or absorption and these are dominated by much heavier uranium signals.

Though other fluxes were tried, none yielded convincing results.

This is the starting point of the investigation on the aluminium incorporation and the sample quality of UBe_{13} depending on various growth and annealing parameters. The project was a combined effort between the Department of Chemical Metal Science at the MPI CPfS and the authors group, with the project being led by Alfred Amon. Samples were grown and analysed by various structural methods such

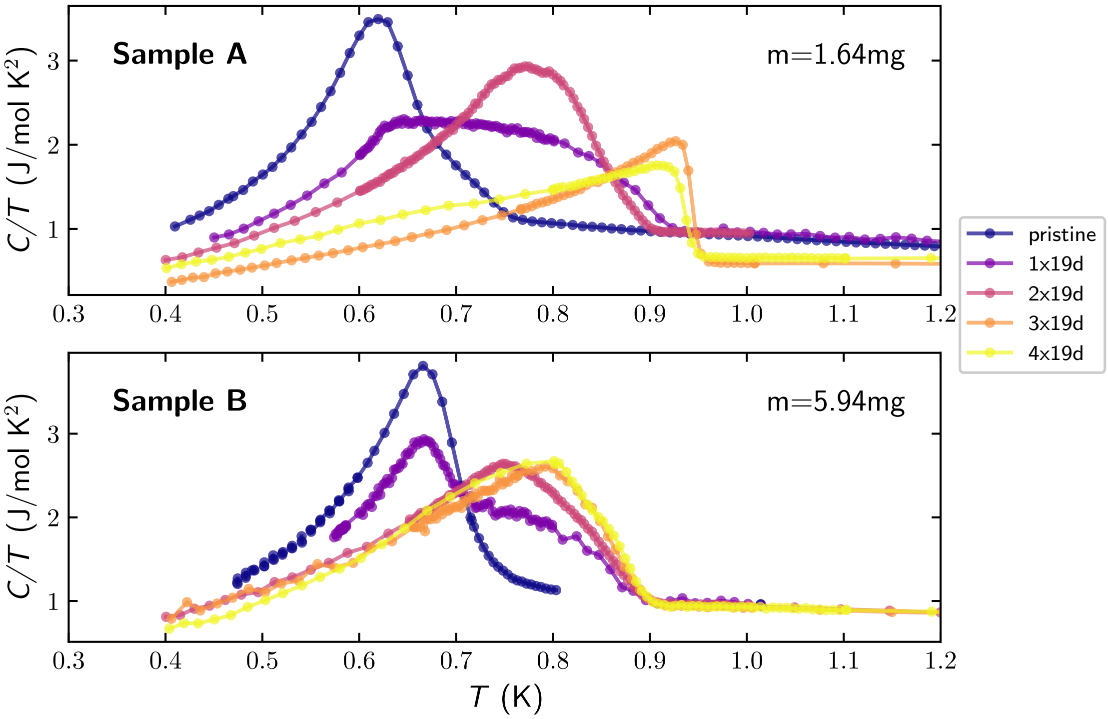

Figure 5.2.1. – Specific heat of two samples of UBe$_{13}$, as it evolves during the stepwise annealing procedure.

as powder and single crystal x-ray diffraction, transition electron microscopy (TEM) or NMR. Some samples were repeatedly annealed for various time spans and their structure reanalysed. At the same time the low temperature properties, first and foremost the specific heat was measured. These low-temperature measurements were contributed by the author. The results were published in [95].

5.2.2. Low-temperature specific heat measurements

After the synthesis, a crystal of UBe$_{13}$ showed mirror like facets but also cracks and voids. A number of smaller samples were then cut from this larger crystal, with their long axis along the crystallographic a direction. Two of them, a small sample 'A' and a larger one 'B', were chosen for further investigation and their specific heat was measured. This showed the samples to be of the low-type variety, with an increasing Sommerfeld coefficient upon cooling and a large jump upon crossing T_c around 0.7 K (see figure 5.2.1).

Both samples were annealed at 900 °C in an argon atmosphere for 19 days, their specific heat re-measured and annealed again. The single transition visible in the

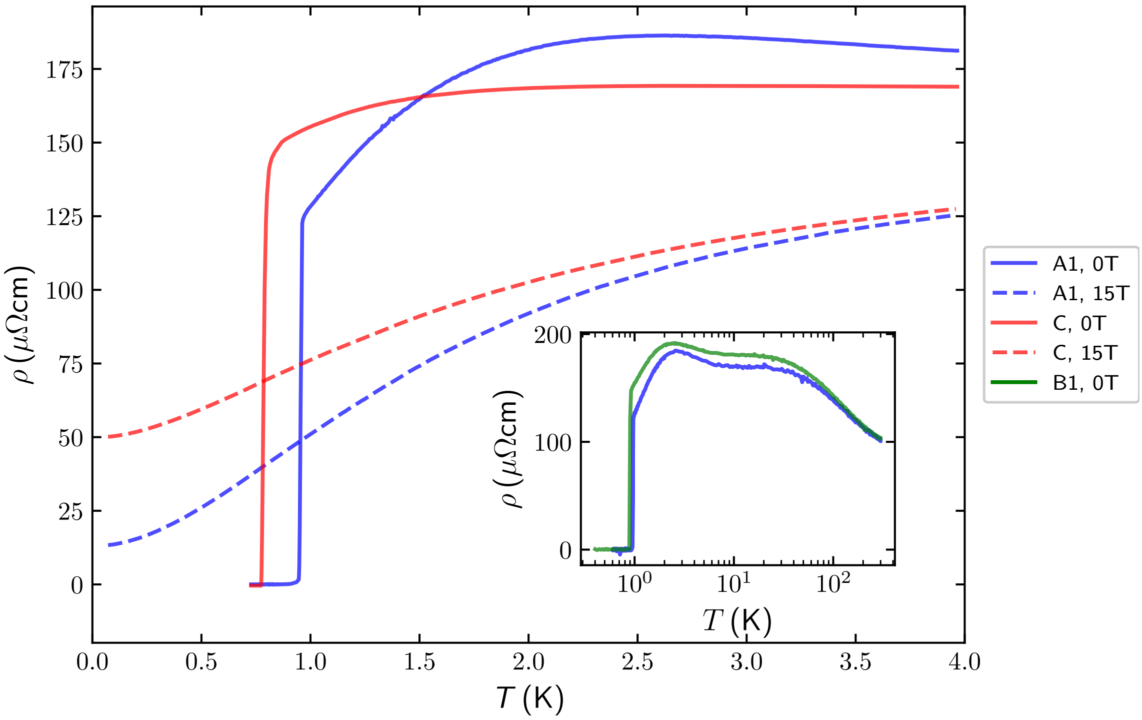

Figure 5.2.2. – Low temperature resistivity of a pristine and an annealed sample of UBe_{13}. In the insert, the resistivity from room temperature down to the superconducting transition of the fully annealed sample (blue) and a partially annealed sample (green) is shown.

pristine sample appears to smear out and move towards higher temperature, with more 'weight' accumulating, in a sharper transition with increasing annealing time. This process is observed in both samples, but appears to be slower in the larger one. While C/T in the normal state was unchanged after the first annealing steps in sample A, it drops to a lower, temperature independent value after the third annealing phase. Apparently, the annealing transforms a low-type crystal to a high-type crystal.

In the last annealing step, the height of the jump in specific heat of sample A is reduced and the weight shifted to lower temperatures, which is understood as a degradation of the sample. This is supported by TEM investigations which observe a destroyed crystal structure in samples annealed for a longer time.

5.2.3. Resistivity measurements

Three samples were also chosen for resistivity measurements.

- A1: A piece of sample A after the annealing procedure, of which the specific heat results were presented above.

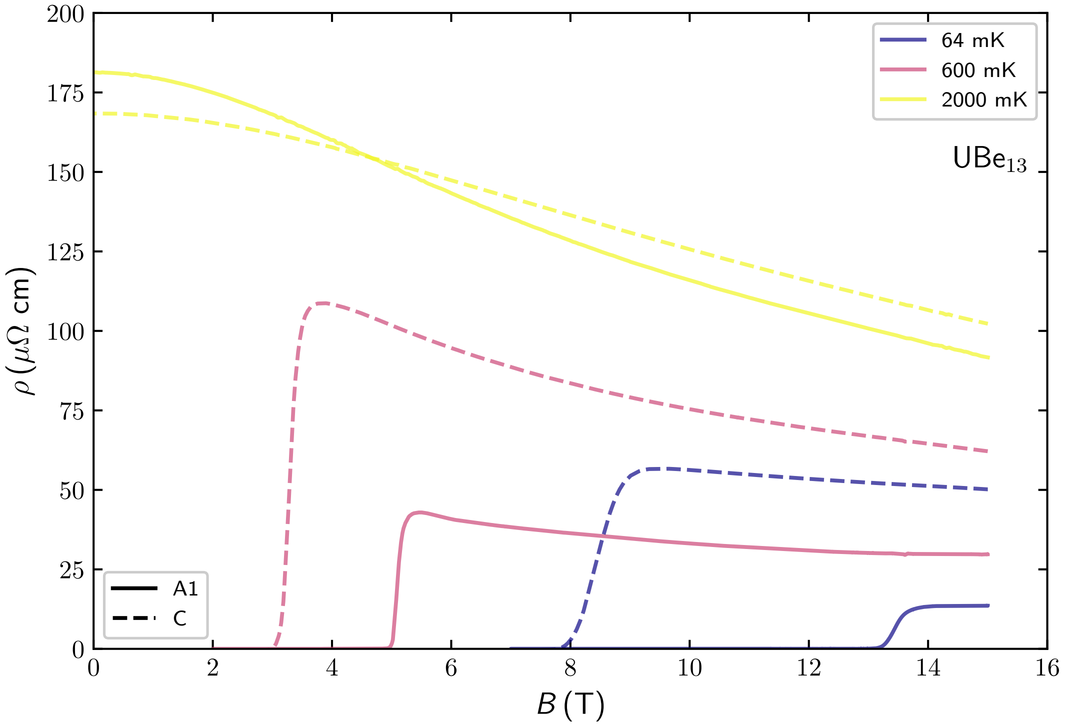

Figure 5.2.3. – Low temperature field dependent resistivity of a pristine and an annealed sample of UBe$_{13}$. The overall lower resistivities in the annealed sample A1 are well visible.

- B1: This piece was cut from sample B and annealed an additional 20 days. The specific heat measured on this sample identifies it as still being of low-type.
- C: A pristine sample, which had not undergone any annealing procedure.

The resistivity from room temperature down to the superconducting transition is shown in the insert of figure 5.2.2. The temperature dependence is in full agreement with the literature reports: Upon cooling from room temperature, the resistivity rises due to the Kondo effect. At the same time, the charge carrier density drops to values equivalent to about 5 % of the room temperature value [96]. Around 40 K the resistivity reaches a plateau, or first hump, before the maximum is reached at around 2.5 K. The last hump is usually interpreted as Kondo-coherence peak. From here, the resistivity decreases until T_c is reached below 1 K. Qualitatively, both the 'fully' annealed sample A1 and the 'partially' annealed sample B1 agree, while sample A1 shows an overall lower resistivity. Note that both resistivities were normalised to a literature room temperature value of 103 µΩ cm to exclude uncertainties in the geometry.

In figure 5.2.2, the resistivity at low temperatures is presented for sample A1 as well as for the pristine sample C. In zero field, the coherence peak of the annealed sample is appreciably more pronounced. Upon application of a magnetic field, the normal state resistivity is reduced due to the polarisation of magnetic moments and an almost normal metallic temperature dependence is recovered. Since the annealing process should reduce the disorder in a sample, the reduced residual resistivity at 15 T of sample A1 compared to sample C is not surprising. This can serve as a measure of sample quality and shows this sample to be of similar quality as the best literature reports (13 µΩ cm compared to ∼10 µΩ cm reported in [97]).

Figure 5.2.3 illustrates the field dependence of the resistivity at three temperatures for sample A1 and C. The negative magnetoresistance is caused by the Kondo effect [72]. In general, the resistivity in field in the annealed sample A1 at lowest temperatures is reduced due to the lower disorder. Also, the sample A1 shows an appreciably elevated B_{c2} over sample C.

Both from the field and temperature dependence of the resistivity, the superconducting phase diagram can be extracted, which is presented in figure 5.2.4. Apparently the $B_{c2}(T)$ dependence of sample A1 coincides with the one reported earlier by Brison *et al.* [97]. Both the results for sample A1 and the pristine sample C agree with earlier reports on the phase diagram of high and low-type crystals respectively [98, 93]. The not-yet fully annealed sample B1 lies somewhere in between.

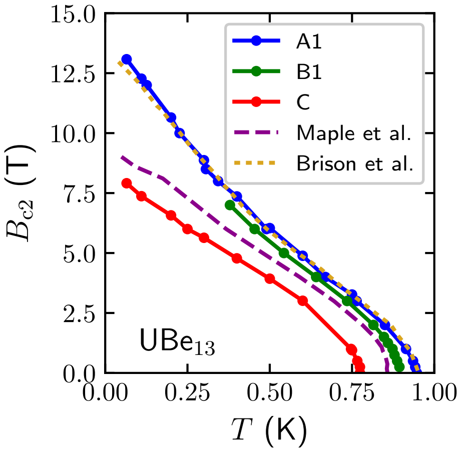

Figure 5.2.4. – Phase diagram as determined by resistivity measurements on samples A1, B1 and C compared to the ones published by Brison *et al.* [97] and Maple *et al.* [98].

Therefore, the study of the phase diagram further supports the impression, that annealing causes the samples to transform from the low-type variety to the high type variety.

5.2.4. Conclusion

The results presented above focus on the low-temperature properties of the metallic and superconducting phase, since the structural investigation was was done by collegues from the chemistry department. It was shown, that aluminium incorporation into the lattice expands the lattice parameter until the solubility limit between 1-2 %

is reached. The lattice parameters found here, agree with the decreasing lattice parameters of the single crystals in the course of the annealing procedure. This suggests a decreasing aluminium concentration with annealing which involves the diffusion of aluminium out of the samples. Naturally, this process is accompanied with inhomogeneities in the bulk since the diffusion is driven by a concentration gradient. This can explain the gradual transition from low to high-type in the specific heat measurements. Since the vapour pressure of Beryllium is rather high, elevated temperatures cause a reduction of Beryllium in the samples, visible as vacancies in the TEM pictures. Also, vacancies appear to arise on lattice sites which were formerly occupied by aluminium. Together, this ultimately leads to the structural disintegration at long annealing times [95].

As a summary, this is the first study which proofs the existence of aluminium in the lattice of UBe$_{13}$ single crystals after synthesis. It also solves the question of the structural difference between the high and low-type varieties, which apparently differ in their aluminium content.

6 Conclusion

The work presented in this thesis consists mainly of transport measurements on the TaAs family of Weyl semimetals, which were employed to learn about novel chiral contributions to the magnetotransport properties. Since the chiral anomaly can be expected in some members of the TaAs family while it should be absent in others, the study is expected to allow for the disentanglement of chiral and non-chiral effects. It was found, that none of the compounds presents any transport properties which can unambiguously be attributed to the chiral anomaly.

Aiming for a clear separation of 'trivial' (i.e. non-chiral) effects such as the artefact of current jetting or the orbital longitudinal magnetoresistance, the influence of both effects was calculated. With the detailed knowledge about the band structure and Fermi surfaces at hand, it was possible to calculate the expected size of the orbital longitudinal magnetoresistance, as presented among the theoretical background in chapter 2. In all materials the *c*-axis magnetotransport is expected to show a pronounced orbital longitudinal magnetoresistance, which was found to be in agreement with the experimental results presented in chapter 4. Indeed, along this direction this is the dominating effect.

Learning more about the influence of contact geometries on the measurement, simulations of the potential distribution, as presented among the other experimental methods in chapter 3, were performed. The main potential drop was found to be perpendicular to the magnetic field and intended current direction, causing apparent negative resistances if the voltage contacts were slightly misaligned. At the same time it was observed, that despite the presence of current jetting, qualitative conclusions regarding the sign of the magnetoresistance can still be drawn, although with some caution.

The bulk of the results as presented in chapter 4 indicate, that the TaAs compounds are first and foremost compensated semimetals, well comparable to materials such as bismuth. This is especially true for TaP, while both niobium compounds seem to host not fully explainable weak-antilocalisation physics when current and field are aligned with the a axis. Due to smaller sample sizes, the longitudinal magnetoresistance in TaAs remains elusive, but a sum of orbital and weak-antilocalisation contributions is most likely.

Two more projects on $CoSb_3$ and UBe_{13} were briefly presented as well. In $CoSb_3$, a first investigation tried to find out about the influence of the growth process on the electronic properties and Fermi energy in this naturally p-doped narrow gap semiconductor. Self flux grown crystals show a higher charge carrier density and effective masses which do not fit to the expectations from DFT calculations. On the other hand, those grown by a novel inclined rotary Bridgman (IRB) method are extremely homogeneous and have an appreciably lower charge carrier concentration. These crystals present an ideal model system for a three dimensional isotropic electron gas with a sufficiently low carrier density to investigate quantum limit physics.

At highest magnetic fields, crystals of IRB grown $\mathrm{CoSb_3}$ show a disorder mediated transverse conductivity σ_{xx} between the quantum limit and the onset of a high-field charge localisation. This is in accordance with an existing theory, which relates the longitudinal conductivity σ_{zz} to the transverse σ_{xx}.

In $\mathrm{UBe_{13}}$, the incorporation of the aluminium flux used during sample growth into the lattice and its influence on the superconducting properties was investigated in a collaborative effort with the chemistry department. In this material, single crystals show low temperature properties, foremost the specific heat, which can either be classified into the 'low-type' or 'high-type'. In a series of annealing steps, each followed by a specific heat measurement, it was shown that the low-type variety evolves into the high-type upon annealing. Structural investigations by the chemistry department found the growth to leave 1-2 % aluminium in the lattice, giving rise to superconducting properties formerly classified to be of 'low-type'. Upon annealing, the aluminium diffuses out, leaving vacancies behind and causing the second variety, 'high-type'. The reduction of disorder and impurities upon annealing is also in agreement with field and temperature dependent transport measurements.

In summary, it was shown that the transport from trivial parts of the band structure in the Weyl semimetals dominate over the chiral ones, rendering the transport properties of these materials similar to those of compensated semimetals, at least to first order. Also, the knowledge of the electronic structure both in the Weyl semimetals and in $\mathrm{CoSb_3}$ was successfully used to differentiate those transport properties well explainable by existing theories and those effects where this is currently not possible. This allows to clearly identify pressing questions in condensed matter physics beyond the boundary of today's understanding.

A | Appendix

A.1. Magnetoconductivity tensor of the TaAs family

As described in chapter 2.1.2, the resistivity tensor as determined in an experiment is the inverse of the conductivity tensor. The number of finite and independent elements of the conductivity tensor is determined by the symmetry of the system. These symmetry operations are given by the respective point group of the crystal. It will be shown, that the symmetries present in the TaAs-family with field along a and c still yield a conductivity tensor as presented in chapter 2.1.2 and the simplified matrix inversion applies. Also, the influence of slight misalignments will be discussed, which is relevant in the analysis of the longitudinal conductivities presented in chapter 4.2.4.

Since the TaAs family belongs to the space group I4$_1$md [63], the point group is $\mathrm{C_{4v}}$, which is invariant under the symmetry operations C_i shown in table A.1.1 as can be found on the Bilbao crystallographic server [99]. Not all these symmetry operations still apply in an applied magnetic field along the c or a direction.

In order to find the finite and independent elements of the conductivity tensor, the tensor has to be invariant under the applicable symmetry transformations:

$$C_i^{\mathrm{T}} \hat{\sigma} C_i^{\mathrm{T}} = \hat{\sigma}. \tag{A.1.1}$$

If a symmetry transformation C_i transforms, e.g. σ_{zy} into $-\sigma_{\mathrm{zy}}$, the condition above can only be satisfied if this component is equal zero.

The transformation of the conductivity tensor for field along c under the twofold rotation around c, 2_{001} in the Seitz notation, should be discussed as an example. Applying the corresponding matrix transformation yields

$$C_{2-(001)}^{\mathrm{T}} \hat{\sigma} C_{2-(001)} = \begin{pmatrix} \sigma_{\mathrm{xx}} & \sigma_{\mathrm{xy}} & -\sigma_{\mathrm{xz}} \\ \sigma_{\mathrm{yx}} & \sigma_{\mathrm{yy}} & -\sigma_{\mathrm{yz}} \\ -\sigma_{\mathrm{xz}} & -\sigma_{\mathrm{yz}} & \sigma_{\mathrm{zz}} \end{pmatrix} = \hat{\sigma}. \tag{A.1.2}$$

This implies, that all off-diagonal terms which include z are zero. The $4^{\pm}_{001}$ transformation further yields $\sigma_{\mathrm{xy}} = -\sigma_{\mathrm{yx}}$. Therefore, the conductivity tensor has the same form as the one presented in chapter 2.1.2 and equations 2.1.5, 2.1.6 and 2.1.7 apply.

With field along the a direction, only the mirror operation in the (010) plane, which is perpendicular to the field direction, is still valid. Since the basis of the conductivity tensor, where z is along the field direction, does not coincide with the basis used for the crystal symmetry operations, the latter has to be transformed by a rotation of 90° around a. Applying this transformation arrives at the same results as the transformation along c, therefore equations 2.1.5, 2.1.6 and 2.1.7 are still valid. However, σ_{xy} and σ_{yx} are independent.

These symmetries might be broken when the current is rotated slightly out of the field, or if the current flow within the sample is not perfectly aligned with the crystal axis. The latter might be caused by inhomogeneities within the sample or current jetting effects.

With the full tensor inversion, ρ_{zz} is influenced by more conductivity tensor components than σ_{zz}:

$$\rho_{\mathrm{zz}} = \frac{\sigma_{\mathrm{xx}}\sigma_{\mathrm{yy}} + \sigma_{\mathrm{xy}}^2}{\sigma_{\mathrm{zz}}(\sigma_{\mathrm{xx}}\sigma_{\mathrm{yy}} + \sigma_{\mathrm{xy}}^2) - \sigma_{\mathrm{xz}}\sigma_{\mathrm{yy}}\sigma_{\mathrm{zx}} - \sigma_{\mathrm{xx}}\sigma_{\mathrm{yz}}\sigma_{\mathrm{zy}} - \sigma_{\mathrm{xx}}\sigma_{\mathrm{yz}}\sigma_{\mathrm{xz}} + \sigma_{\mathrm{zx}}\sigma_{\mathrm{yx}}\sigma_{\mathrm{zy}}}, \tag{A.1.3}$$

$$\rho_{\mathrm{zz}} = \frac{\sigma_{\mathrm{xx}}\sigma_{\mathrm{yy}} + \sigma_{\mathrm{xy}}^2}{\sigma_{\mathrm{zz}}(\sigma_{\mathrm{xx}}\sigma_{\mathrm{yy}} + \sigma_{\mathrm{xy}}^2) + \xi} \sim \frac{1}{\sigma_{\mathrm{zz}}} + \frac{\partial}{\partial \xi}\rho_{\mathrm{zz}} \cdot \xi. \tag{A.1.4}$$

In the second line, all σ_{iz}, with $i \neq z$, containing terms were contracted into ξ, which may be assumed to be very small. Therefore, a Taylor expansion in ξ can be performed which will cause ρ_{zz} to be a sum of $1/\sigma_{\mathrm{zz}}$ with some additive contribution. Since the off-diagonal terms should vanish in zero field, $\frac{\partial}{\partial \xi}\rho_{\mathrm{zz}} \cdot \xi$ should not be a constant offset, rather then a B dependent function vanishing for $B = 0$.

Table A.1.1. – Possible symmetry operations C_i of the space group of the TaAs family, I4$_1$md. Also shown, is which still apply in a magnetic field along the crystallographic a and c direction.

(x,y,z) form	matrix form	Seitz	$B\|\|a$	$B\|\|c$
x,y,z	$\begin{pmatrix} +1 & 0 & 0 \\ 0 & +1 & 0 \\ 0 & 0 & +1 \end{pmatrix}$	1	✓	✓
-x,-y,z	$\begin{pmatrix} -1 & 0 & 0 \\ 0 & -1 & 0 \\ 0 & 0 & +1 \end{pmatrix}$	2_{001}	-	✓
-y,x,z	$\begin{pmatrix} 0 & -1 & 0 \\ +1 & 0 & 0 \\ 0 & 0 & +1 \end{pmatrix}$	4^+_{001}	-	✓
y,-x,z	$\begin{pmatrix} 0 & +1 & 0 \\ -1 & 0 & 0 \\ 0 & 0 & +1 \end{pmatrix}$	4^-_{001}	-	✓
x,-y,z	$\begin{pmatrix} +1 & 0 & 0 \\ 0 & -1 & 0 \\ 0 & 0 & +1 \end{pmatrix}$	m_{010}	✓	-
-x,y,z	$\begin{pmatrix} -1 & 0 & 0 \\ 0 & +1 & 0 \\ 0 & 0 & +1 \end{pmatrix}$	m_{100}	-	-
-y,-x,z	$\begin{pmatrix} 0 & -1 & 0 \\ -1 & 0 & 0 \\ 0 & 0 & +1 \end{pmatrix}$	m_{110}	-	-
y,x,z	$\begin{pmatrix} 0 & +1 & 0 \\ +1 & 0 & 0 \\ 0 & 0 & +1 \end{pmatrix}$	m_{1-10}	-	-

A.2. Calculation of the orbital longitudinal magnetoresistance

The change in resistivity in an applied magnetic field, $\Delta\sigma/\sigma$, as discussed in chapter 2.1 was calculated based on reference [10]. The following equations were used:

$$\sigma_{\mathrm{zz}}(0) \sim S = \int_{\mathrm{FS}} \mathrm{d}^2 k v_{\mathrm{z}}^2 \tag{A.2.1}$$

$$\delta\sigma_{\mathrm{zz}} \sim \delta S = \int_{\mathrm{FS}} \mathrm{d}^2 k \left(v_{\mathrm{z}} \langle v_{\mathrm{z}} \rangle - v_{\mathrm{z}}^2 \right) \tag{A.2.2}$$

Here, the Fermi surface and Fermi velocity have to be known. The starting point of the calculation was the band structure of the individual material. This existed as matrix $E(\mathbf{k})$ as result of DFT calculations made by Binghai Yan, Yan Sun and Shu-Chun Wu using WIEN2K. Typically, the calculation yields a 300x300x90 sized matrix containing the dispersion of an individual band in the whole Brillouin zone. Since the Fermi surfaces are typically rather small compared to the size of the Brillouin zone, the relevant part containing an individual Fermi surface is sliced out of the matrix and interpolated on a 4 to eight times higher point density. The size of the interpolated matrix depends on the size and shape of the Fermi surface, but it consists mostly of about 120x120x200 points. Together with the known Fermi energy, this was fed into MATLABs `isosurface` function to extract the Fermi surface from the matrix.

The `isosurface` function returns so called *faces* and *vertices*. Vertices are points in (here) k space which are on the Fermi surface. The faces contain the information, which three vertices do form one tile on the Fermi surface, therefore it is a vector of indices of vertices. Bigger Fermi surfaces are expressed in about 4000 to 8000 vertices and twice as many faces. The faces and vertices as relevant information about the Fermi surface are saved together with the $E(\mathbf{k})$ matrix and the k grid in a *.mat* file.

In order to calculate the integrals in equations A.2.1 and A.2.2, it is necessary to compute both the Fermi velocity component v_{z} as well as the average of the Fermi velocity component $\langle v_{\mathrm{z}} \rangle$ over a cyclotron orbit.

In order to be able to compute the average of the Fermi velocity over a cyclotron orbit, the Fermi surface is sliced in the direction perpendicular to the field. The width of each slice is chosen equal to the average size of the faces along k_{z}, Δk_{z}. This is computed and all vertices within a slice of Δk_{z} are sought. For every vertex, v_{z} is calculated together with the distance to the adjacent vertices in order to allow for a proper average of the Fermi velocity along the orbit. This is necessary, since the point density on the surface and along the orbit is not constant.

To compute v_z at a certain vertex, the k coordinates of the vertex are sought for in the energy matrix. Since the Fermi velocity is the derivative of the energy with respect to the momentum, this derivative is computed as the average between the forward and backward derivative.

Once both v_z and $(v_\mathrm{z}\langle v_\mathrm{z}\rangle - v_\mathrm{z}^2)$ are known for every vertex, the face average of these is calculated together with the area of the individual face and summed up to yield the integrals in equations A.2.1 and A.2.2.

A.3. Simulation of the electric potential distribution in samples with strong conductivity anisotropies

This section describes the numeric approach in Matlab [100] for the simulation of the potential field within a sample with different contact geometries as discussed in chapter 3.2.2. Mathematically, it is based on the Laplace equation as detailed in Yoshidas publication [11]:

$$\mathrm{div}\mathbf{J} = \hat{\sigma}\Delta U = 0 \tag{A.3.1}$$

$$0 = \sigma^*(\frac{\mathrm{d}^2 U}{\mathrm{d}\zeta^2} + \frac{\mathrm{d}^2 U}{\mathrm{d}\eta^2} + \frac{\mathrm{d}^2 U}{\mathrm{d}\xi^2}). \tag{A.3.2}$$

The first line is the spatial derivative of the microscopic version of Ohms law (see also chapter 2.1). Since there is no current generated within the sample, the divergence of the current has to vanish. In the second line, a coordinate transformation $((x,y,z) \rightarrow (\zeta,\eta,\xi))$ was done, which takes the conductivity anisotropy into account. The new coordinates, ζ,η,ξ, can be obtained such as

$$\begin{aligned}\zeta &= \sqrt{\frac{\sigma_{\mathrm{zz}}}{\sigma_{\mathrm{xx}}}}x,\\ \eta &= \sqrt{\frac{\sigma_{\mathrm{zz}}}{\sigma_{\mathrm{yy}}}}y,\\ \xi &= z,\\ \sigma^* &= \sigma_{\mathrm{zz}}.\end{aligned}$$

This transformation can be thought of as a rescaling of distances. If e.g. σ_{xx} is considerably smaller than σ_{zz}, as it is the case in a compensated semimetal in high magnetic fields, this is equivalent to the sample 'growing' in the x direction, therefore inhibiting a equilibration of the current in x direction.

Equation A.3.2 will now be solved by numeric means. For this, the sample will be transformed onto a discrete spatial grid, consisting of a number of points N, M and P in the x, y and z direction respectively. In order to do calculations on this discrete grid, equation A.3.2 has to be converted into a discretised form.

A.3.1. Notation and algorithm

The basic mathematics of the algorithms were taken from reference [101] but since it is quite basic there is plenty of other material on this topic on the internet. The algorithm will be outlined on the example of a function f on a discrete 3D grid formed by the variables x, y and z. In the calculations, f will be the potential field U. Individual points on the grid will be denoted x_i with $i \in [0,N]$ and y, z likewise. The grid spacing Δx is homogeneous and is given by $\Delta x = x_{i+1} - x_i$ and Δy and Δz in analogue fashion. The value of the function $f(x_i,y_j,z_k)$ will be contracted to $f_{i,j,k}$.

If a simple central difference in 1D is used, the first derivative $\partial f/\partial x|_i$ of a function f_i can be computed such as

$$\left.\frac{\partial f}{\partial x}\right|_i \approx \frac{f_{i+1} - f_{i-1}}{2\Delta x}.$$

Applying this once more, we arrive at the second derivative

$$\frac{\partial^2 f}{\partial x^2} \approx \frac{f_{i+1} - 2f_i + f_{i-1}}{(\Delta x)^2}.$$

With this, the 3D Laplace equation can be rewritten. For the sake of convenience, the inverse of the grid-spacings are used $\alpha = 1/(\Delta x)$, $\beta = 1/(\Delta y)$ and $\gamma = 1/(\Delta z)$

$$\begin{aligned} 0 &\approx \alpha^2(f_{i+1,j,k} - 2f_{i,j,k} + f_{i-1,j,k}) + \beta^2(f_{i,j+1,k} - 2f_{i,j,k} + f_{i,j-1,k}) + \\ &\quad \gamma^2(f_{i,j,k+1} - 2f_{i,j,k} + f_{i,j,k-1}) \\ f_{i,j,k} &\approx \frac{1}{2}(\alpha^2 + \beta^2 + \gamma^2) \left[\alpha^2(f_{i+1,j,k} + f_{i-1,j,k}) + \beta^2(f_{i,j+1,k} + f_{i,j-1,k}) + \right. \\ &\quad \left. \gamma^2(f_{i,j,k+1} + f_{i,j,k-1})\right]. \end{aligned}$$

Obviously, this is a system of linear equations for the grid values. Solving this directly for about 300 000 equations might come with numerical difficulties, which is why an iterative method, the Jacobi algorithm, can be used. This is relaxing $f_{i,j,k}$ to an approximate solution. The grid is initialised to some start values $f^0_{i,j,k}$. Then it is updated iteratively to the next step $f^1_{i,j,k}$ such as

$$\begin{aligned} f^1_{i,j,k} &\approx \frac{1}{2}(\alpha^2 + \beta^2 + \gamma^2) \left[\alpha^2(f^0_{i+1,j,k} + f^0_{i-1,j,k}) + \beta^2(f^0_{i,j+1,k} + f^0_{i,j-1,k}) + \right. \\ &\quad \left. \gamma^2(f^0_{i,j,k+1} + f^0_{i,j,k-1})\right] \end{aligned}$$

and likewise going from iteration step l to $l+1$. The procedure is stopped once e.g. the relative change of the grid value $|f^{l+1}_{i,j,k} - f^l_{i,j,k}|/f^l_{i,j,k}$ is small enough.

A slight alteration of this, the *successive over relaxation* (SOR), increases the speed and was used for the calculations in this thesis and implemented in Matlab [100]. Here, a factor ω is introduced which increases the step size if it is chosen greater 1. The equation above is altered such as

$$f^{l+1}_{i,j,k} \approx (1-\omega) f^{l}_{i,j,k} + \omega \frac{1}{2}(\alpha^2+\beta^2+\gamma^2) \left[\alpha^2 (f^{l}_{i+1,j,k} + f^{l}_{i-1,j,k}) + \beta^2 (f^{l}_{i,j+1,k} + f^{l}_{i,j-1,k}) + \gamma^2 (f^{l}_{i,j,k+1} + f^{l}_{i,j,k-1}) \right] . \tag{A.3.3}$$

By trial and error it was found that $\omega = 1.5$ yields the best speed up.

What equation A.3.3 effectively states is that each point is relaxed to some (modified by ω) average between its neighbours. If the relaxation is started on a grid composed of equal values apart from some difference e.g. along the boundary, the perturbation has to propagate into the interior and then relax to some steady state value. On large grids, this is rather inefficient. To put it into a different language, the algorithm will relax quickly for short wavelengths relative to its grid size but fails at long wavelengths. To counter this and speed up the calculation further, it is typically started on a rather coarse grid. Once this has relaxed, it is interpolated and the previous result used as a starting grid for the next relaxation. In the next step, the 'long' wavelengths relative to the grid size have already converged, which speeds up the process.

A.3.2. Solving Yoshidas equation

Solving the partial differential equation A.3.2 can only be done by setting the correct boundary conditions. Since the current through the sample is kept constant in an experiment, the boundary condition for the voltage field U is a defined constant gradient at the surfaces of the sample. This gradient is finite where there is a current contact and zero everywhere else, since there is no current running through other surfaces of the sample. This type of boundary condition is also referred to as *von-Neumann* boundary condition.

To implement it, the outermost layer of points of the sample is reset before each relaxation step is performed. Every point, where there is no current contact is set to the value of the next point towards the interior. Where there is a current contact (e.g. on a surface perpendicular to the z axis) the value of the boundary $U_{i,j,0}$ can be obtain

$$U_{i,j,0} = \frac{I \Delta z}{\sigma_{\mathrm{zz}} \cdot (\Delta\tilde{x} \Delta\tilde{y})} \pm U_{i,j,1}$$

where $\Delta\tilde{x}$ and $\Delta\tilde{y}$ denote the size of the rectangular contact in the x and y direction. The sign is set depending on the contact being I+ or I-. The total current is kept constant in the calculation.

The code was structured such, that all parameters for the calculation of the voltage distribution for a fixed magnetic field are fed into a parameter file. The MATLAB `.mat` files were used. An individual file was created for each magnetic field value at which a potential distribution is supposed to be calculated. These files include parameters such as sample size, contact size and position and the diagonal components of the conductivity tensor which is the only field dependent quantity.

Upon loading one parameter file, a minimally sized grid is created and relaxed under the given boundary conditions. This is then interpolated twofold along every direction and relaxed again until a certain maximum number of grid points is exceeded. The last relaxed grid typically contains more than 300 000 points and is saved for a later analysis.

For the analysis, the individual relaxed grid, representing the potential distribution at an individual magnetic field, would be loaded for graphic display or to extract the potential difference from e.g. a certain voltage contact geometry on the surface of the sample.

Using individual, and independent, parameter files for each magnetic field allows for an easy way for parallelisation: Since there was access to Matlabs *Parallel toolbox*, changing the `for`-loop running over all parameter files into a `parfor` resulted in the parallel execution of, in this case, four parameter files. A calculation consisting of about 100 individual relaxations (i.e. for magnetic fields from 0-10 T in 0.1 T steps) will take about one to a few hours.

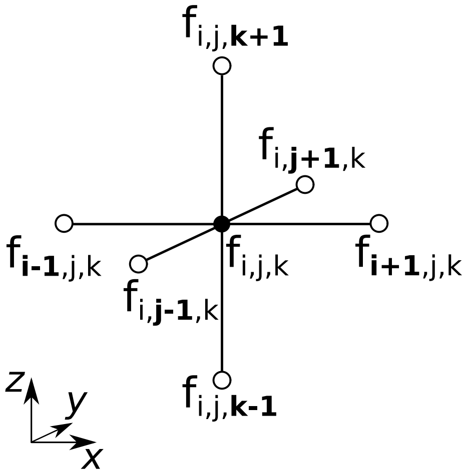

Figure A.3.1. – Schematic illustration of the stencil which is used to update a point $f_{i,j,k}$.

A.3.3. Possible improvements

One of the biggest shortcomings of the created code is the fixed parallel orientation between the rectangular samples main axis and the magnetic field. It would have been rather interesting to observe the angular dependence around the parallel orientation.

A.4. Estimate of the Debye length in Weyl systems

The anisotropy of the chiral anomaly depends on the size of the impurity potential, as discussed in chapter 2.7. This can be estimated using the Deby length, which can be computed such as

$$l_\mathrm{D} = \sqrt{\frac{\epsilon_0 \epsilon_r}{e_0^2 D(E_\mathrm{F})}}. \tag{A.4.1}$$

Here, $\epsilon_0\epsilon_r$ describe the dielectric constant of the lattice, and $D(E_\mathrm{F})$ the density of states at the Fermi energy. In reference [102], ϵ_r was found to be 800. Including uncertainties, we will use a range of 100-1000.

The density of states will be estimated in a free electron gas model [69]. It can be retrieved such as

$$D(E_\mathrm{F}) = \frac{\partial N}{\partial E} = \frac{1}{4\pi^2}\left(\frac{2m}{\hbar^2}\right)^{3/2}\sqrt{E_\mathrm{F}}. \tag{A.4.2}$$

Assuming an effective mass of 0.05-0.1 and a Fermi energy of 10-30 meV (see chapter 4.2.3 and [13, 12, 14, 36, 15]) we arrive at a range of $D(E_\mathrm{F}) = 3.8 \cdot 10^{18}\text{–}1.9 \cdot 10^{19}\,\mathrm{eV}^{-1}\,\mathrm{cm}^{-3}$. This then yields a range of Debye lengths, $l_\mathrm{D} = 1.7 \cdot 10^{-8} - 1.2 \cdot 10^{-7}\,\mathrm{m}$.

A.5. Validity of $T = T_{\mathrm{eff}}$

In the computation of the diffusion constant from the two-band mobilities and charge carrier densities in chapter 4.2.4, the temperature T_{eff} was set equal the measurement temperature T. This can be justified, since the derivation of the diffusion constant found in [76] was done for semiconductors. In these materials, higher internal electric fields due to e.g. higher resistivities of the material are possible.

Taking this into account, the diffusion constant D can be computed as

$$D = \frac{k_{\mathrm{B}}T_{\mathrm{eff}}}{e}\frac{n+p}{n/\mu_p + p/\mu_e}, \tag{A.5.1}$$

$$k_{\mathrm{B}}T_{\mathrm{eff}} = k_{\mathrm{B}}T + \epsilon\,\underbrace{\frac{np}{n+p}\left[\frac{(1/\mu_e + 1/\mu_p)E}{n/\mu_p + p/\mu_n}\right]^2}_{\alpha}. \tag{A.5.2}$$

Here, n denotes the electron concentration, p the hole concentration, $\mu_{n/p}$ the respective mobilities, ϵ the dielectric function of the material and E the electric field.

To our knowledge, the dielectric constant of NbAs is unknown. However, we can estimate the size of α relative to $k_{\mathrm{B}}T$ to get an idea of a upper boundary of ϵ_r, where the correction of the second term becomes important.

The magnitude of the electric field can be determined by the geometry of the FIB structure and the potential difference, $1\,\mu\mathrm{V}/17\,\mu\mathrm{m} = 0.06\,\mathrm{V\,m^{-1}}$. With the mobilities and charge carrier densities from chapter 4.2.3 and the electric field, $\alpha/(k_{\mathrm{B}}T)$ is found to be $\sim 1.5 \cdot 10^{-5}$. If we want to neglect the influence up to a contribution of about 10 %, an upper boundary of ϵ would be $\sim 1 \cdot 10^4$. This can be compared with calculations of the dielectric constant in TaAs [102], which suggests $\epsilon_{\mathrm{r}} \sim 800$ for an electric field aligned in parallel with a. The correction is therefore on the order of 1 % and is neglected.

Bibliography

[1] N. W. Ashcroft and N. D. Mermin, *Solid State Physics* (Harcourt, 1976).

[2] A. B. Pippard, *Magnetoresistance in Metals*, Cambridge Studies in Low Temperature Physics Vol. 2 (Cambridge University Press, Cambridge, 1989).

[3] W. Shockley, Physical Review **79**, 191 (1950).

[4] R. G. Chambers, Proceedings of the Physical Society. Section A **65**, 458 (1952).

[5] R. G. Chambers, Proc. R. Soc. Lond. A **238**, 344 (1957).

[6] C. Bergemann, A. P. Mackenzie, S. R. Julian, D. Forsythe, and E. Ohmichi, Advances in physics **52**, 639 (2003).

[7] N. E. Hussey, M. Abdel-Jawad, A. Carrington, A. P. Mackenzie, and L. Balicas, Nature **425**, 814 (2003).

[8] M. C. Jones and E. H. Sondheimer, Physical Review **155**, 567 (1967).

[9] A. B. Pippard, Proc. R. Soc. Lond. A **282**, 464 (1964).

[10] H. K. Pal and D. L. Maslov, Physical Review B **81**, 214438 (2010).

[11] K. Yoshida, Journal of Applied Physics **51**, 4226 (1980).

[12] F. Arnold, C. Shekhar, S.-C. Wu, Y. Sun, R. D. d. Reis, N. Kumar, M. Naumann, M. O. Ajeesh, M. Schmidt, A. G. Grushin, J. H. Bardarson, M. Baenitz, D. Sokolov, H. Borrmann, M. Nicklas, C. Felser, E. Hassinger, and B. Yan, Nature Communications **7**, 11615 (2016).

[13] F. Arnold, M. Naumann, S.-C. Wu, Y. Sun, M. Schmidt, H. Borrmann, C. Felser, B. Yan, and E. Hassinger, Physical Review Letters **117**, 146401 (2016).

[14] J. Klotz, S.-C. Wu, C. Shekhar, Y. Sun, M. Schmidt, M. Nicklas, M. Baenitz, M. Uhlarz, J. Wosnitza, C. Felser, and B. Yan, Physical Review B **93**, 121105 (2016).

[15] F. Arnold, M. Naumann, and E. Hassinger, to be published .

[16] B. J. Ramshaw, K. A. Modic, A. Shekhter, Y. Zhang, E.-A. Kim, P. J. W. Moll, M. D. Bachmann, M. K. Chan, J. B. Betts, F. F. Balakirev, A. Migliori, N. J. Ghimire, E. D. Bauer, F. Ronning, and R. D. McDonald, Nature Communications **9**, 2217 (2018).

[17] H.-Z. Lu and S.-Q. Shen, Physical Review B **92**, 035203 (2015).

[18] G. Bergmann, Physics Reports **107**, 1 (1984).

[19] B. L. Altshuler and A. G. Aronov, CHAPTER 1 - Electron–Electron Interaction In Disordered Conductors, in *Modern Problems in Condensed Matter Sciences*, edited by A. L. Efros and M. Pollak, , Electron–Electron Interactions in Disordered Systems Vol. 10, pp. 1–153, Elsevier, 1985.

[20] H. Fukuyama, CHAPTER 2 - Interaction Effects in the Weakly Localized Regime of Two- and Three-Dimensional Disordered Systems, in *Modern Problems in Condensed Matter Sciences*, edited by A. L. Efros and M. Pollak, , Electron–Electron Interactions in Disordered Systems Vol. 10, pp. 155–230, Elsevier, 1985.

[21] S. Hikami, A. I. Larkin, and Y. Nagaoka, Progress of Theoretical Physics **63**, 707 (1980).

[22] B. L. Altshuler, D. Khmel'nitzkii, A. I. Larkin, and P. A. Lee, Physical Review B **22**, 5142 (1980).

[23] E. König-Tarasevich, Private conversation with Dr. Elio König-Tarasevich.

[24] P. Seiler, Private conversation with Dr. Patrick Seiler.

[25] C. Shekhar, A. K. Nayak, Y. Sun, M. Schmidt, M. Nicklas, I. Leermakers, U. Zeitler, Y. Skourski, J. Wosnitza, Z. Liu, Y. Chen, W. Schnelle, H. Borrmann, Y. Grin, C. Felser, and B. Yan, Nature Physics **11**, 645 (2015).

[26] H. Suzuura and T. Ando, Physical Review Letters **89**, 266603 (2002).

[27] N. Armitage, E. Mele, and A. Vishwanath, Reviews of Modern Physics **90**, 015001 (2018).

[28] D. T. Son and B. Z. Spivak, Physical Review B **88**, 104412 (2013).

[29] H. B. Nielsen and M. Ninomiya, Physics Letters B **130**, 389 (1983).

[30] S. L. Adler, Physical Review **177**, 2426 (1969).

[31] J. S. Bell and R. Jackiw, Il Nuovo Cimento A (1965-1970) **60**, 47 (1969).

[32] A. Johansson, J. Henk, and I. Mertig, Physical Review B **99**, 075114 (2019).

[33] C.-L. Zhang, S.-Y. Xu, I. Belopolski, Z. Yuan, Z. Lin, B. Tong, G. Bian, N. Alidoust, C.-C. Lee, S.-M. Huang, T.-R. Chang, G. Chang, C.-H. Hsu, H.-T. Jeng, M. Neupane, D. S. Sanchez, H. Zheng, J. Wang, H. Lin, C. Zhang, H.-Z. Lu, S.-Q. Shen, T. Neupert, M. Z. Hasan, and S. Jia, Nature Communications **7**, 10735 (2016).

[34] A. Johansson, Private conversation with Annika Johansson., 2019.

[35] J. Behrends and J. H. Bardarson, Physical Review B **96**, 060201 (2017).

[36] Y. Sun, S.-C. Wu, and B. Yan, Physical Review B **92**, 115428 (2015).

[37] H.-J. Kim, K.-S. Kim, J.-F. Wang, M. Sasaki, N. Satoh, A. Ohnishi, M. Kitaura, M. Yang, and L. Li, Physical Review Letters **111**, 246603 (2013).

[38] X. Huang, Physical Review X **5** (2015).

[39] Y. Li, Z. Wang, P. Li, X. Yang, Z. Shen, F. Sheng, X. Li, Y. Lu, Y. Zheng, and Z.-A. Xu, Frontiers of Physics **12**, 127205 (2017).

[40] J.-F. Mercure, *The de Haas van Alphen effect near a quantum critical end point in Sr3Ru2O7*, Doktorarbeit, University of St Andrews, 2008.

[41] C. Bergemann, *Magnetic Effects in Unconventional Superconductors*, Doktorarbeit, Trinity College, Cambridge, 1999.

[42] D. Shoenberg, *Magnetic Oscillations in Metals by D. Shoenberg* (Cambridge University Press, 1984).

[43] L. Landau, Zeitschrift für Physik **64**, 629 (1930).

[44] L. Shubnikov and W. J. de Haas, Leiden Comm. **207a** (1930).

[45] W. J. de Haas and P. M. van Alphen, Leiden Comm. **208a** (1930).

[46] L. Onsager, The London, Edinburgh, and Dublin Philosophical Magazine and Journal of Science **43**, 1006 (1952).

[47] I. M. Lifshitz and A. M. Kosevich, JETP **2**, 636 (1956).

[48] A. McCollam, S. R. Julian, P. M. C. Rourke, D. Aoki, and J. Flouquet, Physical Review Letters **94**, 186401 (2005).

[49] P. Moll, (2019).

[50] C. Wang, H.-Z. Lu, and S.-Q. Shen, Physical Review Letters **117**, 077201 (2016).

[51] H. Ulrich and H. Weber, *Laplace-, Fourier- und z-Transformation: Grundlagen und Anwendungen*, 10 ed. (Springer Vieweg, 2017).

[52] F. J. Harris, Proceedings of the IEEE **66**, 51 (1978).

[53] M. C. Steele, Physical Review **97**, 1720 (1955).

[54] K. Yoshida, Journal of the Physical Society of Japan **39**, 1473 (1975).

[55] K. Yoshida, Journal of the Physical Society of Japan **40**, 1027 (1976).

[56] K. Yoshida, Journal of the Physical Society of Japan **41**, 574 (1976).

[57] R. D. d. Reis, M. O. Ajeesh, N. Kumar, F. Arnold, C. Shekhar, M. Naumann, M. Schmidt, M. Nicklas, and E. Hassinger, New Journal of Physics **18**, 085006 (2016).

[58] M. D. Bachmann, N. Nair, F. Flicker, R. Ilan, T. Meng, N. J. Ghimire, E. D. Bauer, F. Ronning, J. G. Analytis, and P. J. W. Moll, Science Advances **3**, e1602983 (2017).

[59] Q. D. Inc., Quantum Design SVSM Manual.

[60] J. Clarke and A. Braginski, *The SQUID handbook - Vol. 1* (Wiley-VCH Verlag GmbH, Weinheim, 2004).

[61] H. Weyl, Zeitschrift fur Physik **56**, 330 (1929).

[62] B. Yan and C. Felser, Annual Review of Condensed Matter Physics **8**, 337 (2017).

[63] H. Weng, C. Fang, Z. Fang, B. A. Bernevig, and X. Dai, Physical Review X **5**, 011029 (2015).

[64] N. J. Ghimire, Y. Luo, M. Neupane, D. J. Williams, E. D. Bauer, and F. Ronning, Journal of Physics: Condensed Matter **27**, 152201 (2015).

[65] S.-M. Huang, S.-Y. Xu, I. Belopolski, C.-C. Lee, G. Chang, B. Wang, N. Alidoust, G. Bian, M. Neupane, C. Zhang, S. Jia, A. Bansil, H. Lin, and M. Z. Hasan, Nature Communications **6**, 7373 (2015).

[66] T. Besara, D. A. Rhodes, K.-W. Chen, S. Das, Q. R. Zhang, J. Sun, B. Zeng, Y. Xin, L. Balicas, R. E. Baumbach, E. Manousakis, D. J. Singh, and T. Siegrist, Physical Review B **93**, 245152 (2016).

[67] Y. Luo, N. J. Ghimire, E. D. Bauer, J. D. Thompson, and F. Ronning, Journal of Physics: Condensed Matter **28**, 055502 (2016).

[68] Z. Wang, Y. Zheng, Z. Shen, Y. Lu, H. Fang, F. Sheng, Y. Zhou, X. Yang, Y. Li, C. Feng, and Z.-A. Xu, Physical Review B **93**, 121112 (2016).

[69] C. Kittel, *Introduction to Solid State Physics*, 8th ed. (Wiley John + Sons, Hoboken, NJ, 2004).

[70] M. Besser, Masterarbeit, 2017.

[71] J. Kondo, Progress of Theoretical Physics **32**, 37 (1964).

[72] A. C. Hewson, *The Kondo Problem to Heavy Fermions*Cambridge studies in magnetism (Cambridge University Press, 1993).

[73] D. Long and J. Myers, Physical Review **115**, 1107 (1959).

[74] A. Kawabata, Journal of the Physical Society of Japan **49**, 628 (1980).

[75] D. V. Baxter, R. Richter, M. L. Trudeau, R. W. Cochrane, and J. O. Strom-Olsen, Journal de Physique **50**, 1673 (1989).

[76] P. Kleinert and V. V. Bryksin, Applied Physics Letters **86**, 062102 (2005).

[77] H. Rakoto, E. Arushanov, M. Respaud, J. M. Broto, J. Leotin, C. Kloc, E. Bucher, and S. Askenazy, Physica B: Condensed Matter **246–247**, 528 (1998).

[78] T. Caillat, A. Borshchevsky, and J. Fleurial, Journal of Applied Physics **80**, 4442 (1996).

[79] J. C. Smith, S. Banerjee, V. Pardo, and W. E. Pickett, Physical Review Letters **106**, 056401 (2011).

[80] V. Pardo, J. C. Smith, and W. E. Pickett, Physical Review B **85**, 214531 (2012).

[81] E. Arushanov, M. Respaud, H. Rakoto, J. M. Broto, and T. Caillat, Physical Review B **61**, 4672 (2000).

[82] F. Pobell, *Matter and Methods at Low Temperatures*, 3 ed. (Springer-Verlag, Berlin Heidelberg, 2007).

[83] M. Pillaca, O. Harder, W. Miller, and P. Gille, Journal of Crystal Growth **475**, 346 (2017).

[84] J. F. Woods and C. Y. Chen, Physical Review **135**, A1462 (1964).

[85] B. I. Halperin, Japanese Journal of Applied Physics **26**, 1913 (1987).

[86] F. Arnold, A. Isidori, E. Kampert, B. Yager, M. Eschrig, and J. Saunders, Physical Review Letters **119**, 136601 (2017).

[87] Z. Zhu, P. Nie, B. Fauqué, B. Vignolle, C. Proust, R. D. McDonald, N. Harrison, and K. Behnia, Physical Review X **9**, 011058 (2019).

[88] R. G. Mani, J. R. Anderson, J. B. Choi, and D. A. Nelson, Physical Review B **36**, 9146 (1987).

[89] S. S. Murzin, A. G. M. Jansen, and E. G. Haanappel, Physical Review B **62**, 16645 (2000).

[90] A. Bhattacharya, B. Skinner, G. Khalsa, and A. V. Suslov, Nature Communications **7**, 12974 (2016).

[91] B. Fauqué, Private conversation with Dr. Benoît Fauqué., 2018.

[92] H. R. Ott, H. Rudigier, Z. Fisk, and J. L. Smith, Physical Review Letters **50**, 1595 (1983).

[93] C. Langhammer, R. Helfrich, A. Bach, F. Kromer, M. Lang, T. Michels, M. Deppe, F. Steglich, and G. R. Stewart, Journal of Magnetism and Magnetic Materials **177-181**, 443 (1998).

[94] H. U. Borgstedt, H. Wedemeyer, and Gmelin, *Handbook inorganic chemistry. U - Uranium*, U. Uran. Uranium (System-Nr. 55) Vol. B2, 8 ed. (Springer-Verlag, Berlin Heidelberg, 1989).

[95] A. Amon, I. Zelenina, P. Simon, M. Bobnar, M. Naumann, E. Svanidze, F. Arnold, H. Borrmann, U. Burkhardt, W. Schnelle, E. Hassinger, A. Leithe-Jasper, and Y. Grin, Scientific Reports **8**, 10654 (2018).

[96] T. Penney, J. Stankiewicz, S. von Molnar, Z. Fisk, J. L. Smith, and H. R. Ott, Journal of Magnetism and Magnetic Materials **54-57**, 370 (1986).

[97] J. P. Brison, J. Flouquet, and G. Deutscher, Journal of Low Temperature Physics **76**, 453 (1989).

[98] M. B. Maple, J. W. Chen, S. E. Lambert, Z. Fisk, J. L. Smith, H. R. Ott, J. S. Brooks, and M. J. Naughton, Physical Review Letters **54**, 477 (1985).

[99] Bilbao Crystallographic Server, http://www.cryst.ehu.es/cgi-bin/cryst/programs/nph-point_genpos?num=13.

[100] MATLAB R2017a, The MathWorks, Inc., Natick, Massachusetts.

[101] S. Dalziel, Numeric mathematic lecture, 1998.

[102] J. Buckeridge, D. Jevdokimovs, C. R. A. Catlow, and A. A. Sokol, Physical Review B **93**, 125205 (2016).

Acknowledgment

At the end of a thesis, the time has come to thank those who allowed me to write it in the first place and who made the time worthwhile.

The first to mention here is *Prof. Elena Hassinger*. I would like to thank her for the opportunity to work in her young group, observe it its people grow, the continuous motivation to proper scientific work in contrast to our field of research and reading the drafts of this thesis at lengths.

Also, I want to mention *Prof. Clemens Laubschat*, for supervising the project officially in the first years, being a member of the examination committee and long conversations about topics away from physics but not less interesting.

Prof. Andrew Mackenzie I would like to thank for the opportunity to work alongside his department at the MPI CPfS.

Experimental condensed matter physics would not be possible without high quality samples from skilled sample growers. Therefore I would like to thank *Marcus Schmidt* and *Vicky Süß* for providing the samples of the TaAs family. Further, I would like to thank *Andreas Leithe-Jasper*, *Flipo Sever*, *Prof. Peter Gille* and *Mirtha Pillaca-Quispe* for growing and providing CoSb$_3$ as well as (again) *Andreas* and *Alfred Amon* for the UBe$_{13}$ samples. It was a pleasure to work with all of them, for their easy accessibility and patient explanation of the chemical background.

Learning new techniques and skills of all kinds is an essential part of a PhD thesis. One of the persons who taught me most during my physical education, who guided all projects presented here in their early stages and whose company in the office I appreciated a lot was *Frank Arnold.*

I would also like to thank my former collegue and local contact during the high magnetic field measurements, *Tobias Förster* for his support and all the conversations in recent years.

The projects described above were always done in collaborations of various kinds. People who contributed by discussions, explanations of theories or information about other or even unpublished research are *Johannes Klotz*, *Michael Baenitz*, *Tobias Meng*, *Elio König-Tarasevich*, *Benoît Fauqué*, *Helge Rosner*, *Burkhard Schmidt* and *Thilo Kopp*. For the preparation of the NbAs microstructures, I would like to acknowledge *Maja Bachmann*. I am particularly grateful to *Patrick Seiler* for taking the patience and time to respond to numerous emails during the last days of writing this thesis.

Colleagues who make the workplace enjoyable cannot be underestimated. I would therefore like to thank *Zuzana Medvecka*, *Onishi Hakase*, *Daniel Hafner*, *Javier Landaeta*, *Fabian Jerzembek*, *Parisa Mokhtari* and *Stefan Lucas* for their companionship, also outside the working hours. Special thanks goes to *Sebastian Seifert*, for many work related and not work related technical conversations and his attempts to gold plate TaAs. *Michael Nicklas* should be mentioned for the frequent conversations educating me about many aspects of research besides physics. I would also like to thank *Thomas Lühmann*, *Robert Borth*, *Manuel Brando*, *Markus König*, *Oliver Stockert*, *Ulrike Stockert*, *Burkhard Schmidt*, *Ralf Weise*, *Walter Schnelle*, *Renate Hempel-Weber*, *Robert Küchler*, *Alexander Steppke* and *Jörg Sichelschmidt* for their company and more often then not entertaining conversations in the coffee corner and over lunch.

No research facility or university could run without support from the technical and organisational staff of all kinds. I want to thank all of them, both at CPfS and TU Munich, for their easy accessibility and friendly ears in all matters.

Auch alte Kollegen sollen hier nicht vergessen sein. Insbesondere *Richard Skrotzki* möchte ich hier erwähnen.

Ohne Unterstützung aus dem privaten Freundeskreis wäre all dies nicht möglich gewesen. Die richtigen Leute wissen, dass sie gemeint sind =).

Traditionell an letzter Stelle in dieser Liste möchte ich jene erwähnen, die eigentlich an die Erste gehören: Ohne die Unterstützung meiner Eltern würde ich diese Zeilen wohl kaum schreiben.